417141

Analysis Package for the Culebra Flow and Transport Calculations (Task 3) of the Performance Assessment Analyses Supporting the Compliance Certification Application Analysis Plan 019 Version 00

(WPO# 40516)

James Ramsey 12/10/96

James Ramsey / Org. 6849
Author / Principal Investigator — Date

Michael D. Wallace 12/11/96

Mike Wallace / Org. 6849
Principal Investigator — Date

12/11/96

Hong-Nian Jow / Org. 6848
Department Manager — Date

Information Only

Analysis Package for the Culebra Flow and Transport Calculations (Task 3) of the Performance Assessment Analyses Supporting the Compliance Certification Application Analysis Plan 019 Version 00

(WPO# 40516)

Effective Date: _____

WBS Number: 1.2.07.4.1
Author: James L. Ramsey, SNL, Organization 6849
Manager: D.R. Anderson, SNL, Organization 6849

Analyst	James Ramsey, SNL Mike Wallace, RE/SPEC
Technical Reviewers	Alex Treadway, SNL George Barr, SNL Ron Dykhuizen, SNL Andrew Peterson, SNL
Quality Assurance Reviewers	Victor Harper-Slaboszewicz, SNL Sid Ailes, CTAC
Managers	D. Richard Anderson, SNL Hong-Nian Jow, SNL

Information Only

Table of Contents

1.0 Introduction 4
2.0 Analysis Overview 8
2.1 Deviations from the Analysis Plan (AP-019) 11
2.2 Software Requirements 13
2.3 Assumptions 16
2.4 Data Sources 18
2.5 Initial and Boundary Conditions 20
2.5.1 Groundwater flow 20
2.5.1 Groundwater Transport 26
2.6 Potash Mining 27
3.0 Personnel Assignments and Training Requirements 30
4.0 QA Requirements 30
5.0 Technical Approach 30
6.0 Conclusions 35
7.0 Results 35
7.1 Culebra Flow Results 35
7.2 Culebra Transport Results 52
7.3 Solution Convergence 67
7.3.1 Spatial Discretization 67
7.3.2 Temporal Discretization 78
8.0 References 86

Appendices
A. Physical Transport in the Culebra Dolomite, Meigs and McCord (1996)
B. Supporting documentation
C. TRACKER source listing and code verification
D. Input Data
E. Input Files
F. Background Information
G. Glossary

Information Only

1.0 Introduction

As part of the Compliance Certification Application (CCA) for the Waste Isolation Pilot Project (WIPP), a performance assessment (PA) was conducted to compute the complementary cumulative distribution function (CCDF) of the normalized cumulative radionuclide release to the accessible environment. Groundwater flow and radionuclide transport were simulated in the Culebra Dolomite member of the Rustler Formation as part of this performance assessment. These simulations are identified as Task 3 in Fewell (1996).

This document contains a detailed description of the Culebra flow and transport simulations performed under Analysis Plan #019 (AP-019, Ramsey, 1996). Background information describing how the various Task introduced by Fewell (1996) are combined to compute releases from the WIPP can be found in Appendix F. Definitions of commonly used phases, accronyms, and use specific words, are included in Appendix G.

The WIPP repository is located 26 miles (42 kilometers) east of Carlsbad, New Mexico, in Eddy County, Figure 1.1. The disposal horizon of the WIPP is approximately 2,150 feet (650 meters) below the ground surface in the Salado Formation of the Delaware Basin, Figure 1.2. The Salado is regionally extensive, consisting predominately of halite, a low permeable evaporate.

The Rustler Formation is located above the Salado and is of particular importance to the CCA because it contains the most transmissive units above the repository. In the vicinity of the WIPP, the Rustler consist of evaporite units interbedded with carbonates and siliciclastic units. Vine (1963) extensively described the Rustler and proposed the four formal names and one informal name that are still used today as the stratigraphic subdivisions of the Rustler, Figure 1.3. More detailed subdivisions were reported by Holt and Powers (1988) after examining the WIPP shafts as well as core and well data from around 600 boreholes in southeastern New Mexico.

The Culebra was identified in the early stages of site characterization as the most transmissive unit in the Rustler and consequently the most likely pathway for subsurface transport. The Culebra is a fractured dolomite with nonuniform properties both horizontally and vertically. There are multiple scales of porosity and permeability within the Culebra, ranging from microfractures to potentially large vuggy zones. Flow occurs through fractures, vugs, and to some extent though intergranular pores. Large permeability contrast between the different scales of inter-connected porosity are distinguished as those occurring within the advective porosity ϕ_a (also referred to as fracture porosity), and those occurring within the diffusional porosity ϕ_d (also referred to as matrix porosity). The advective porosity consist of the void space contained in the highly transmissive portions of the rock (i.e. large open fractures and/or connected vugs), and the diffusional porosity represents the inter- and intragranular porosity but may also include other features such as microfractures and/or vugs.

Information Only

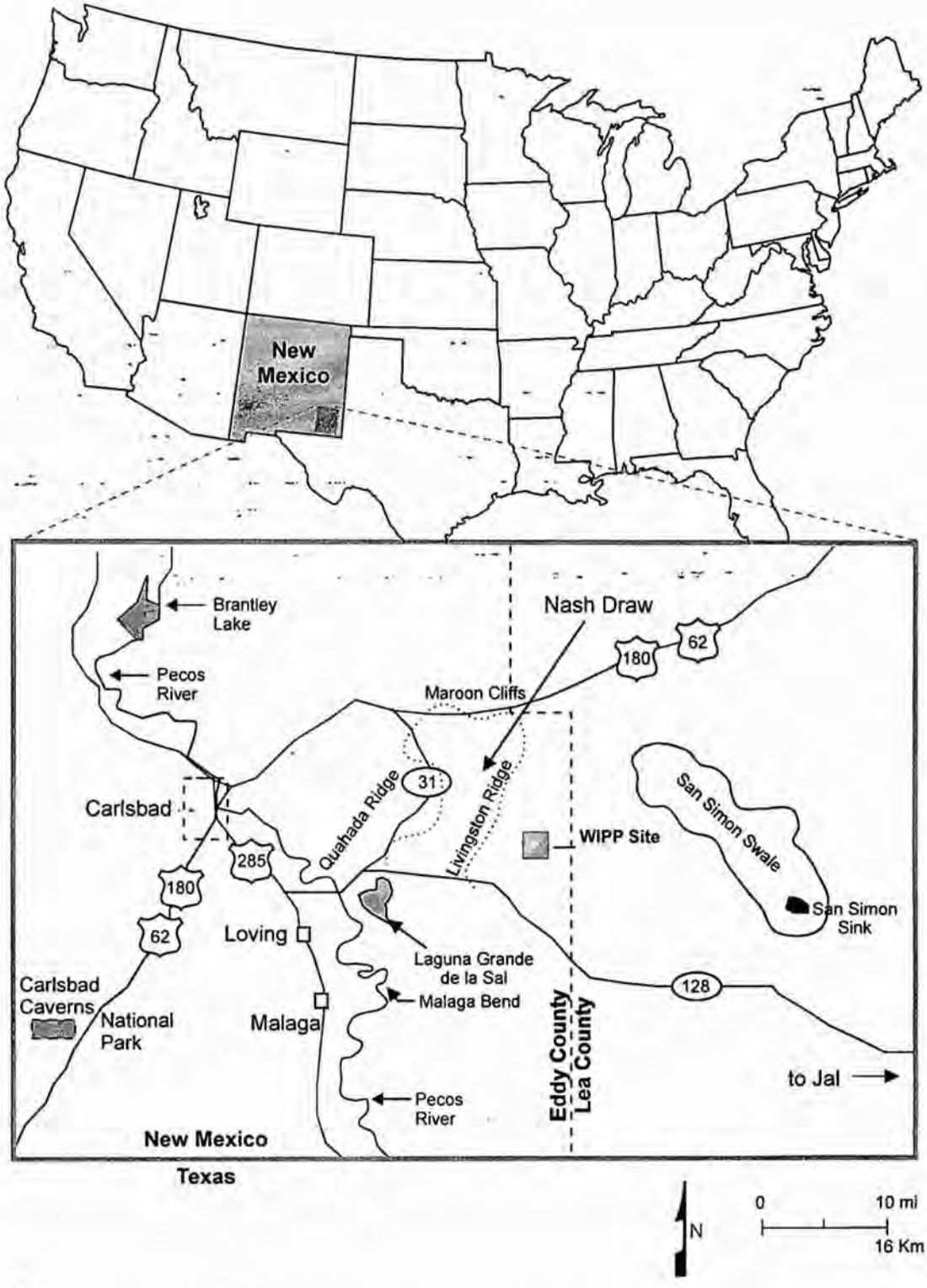

Figure 1.1. WIPP Site Location in Southeastern New Mexico

Information Only

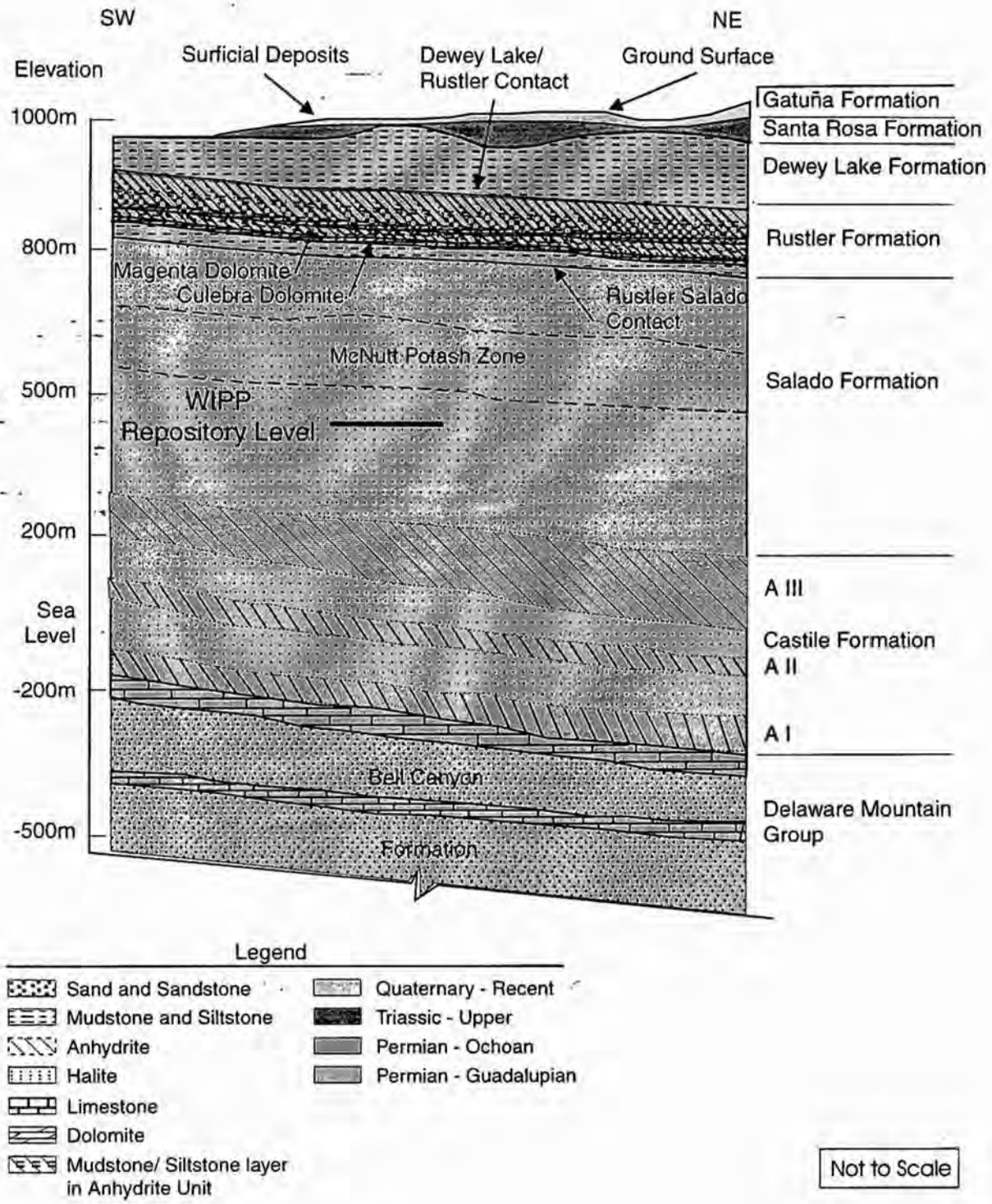

Figure 1.2. Generalized Stratigraphic Cross Section above Bell Canyon Formation at WIPP Site

Information Only

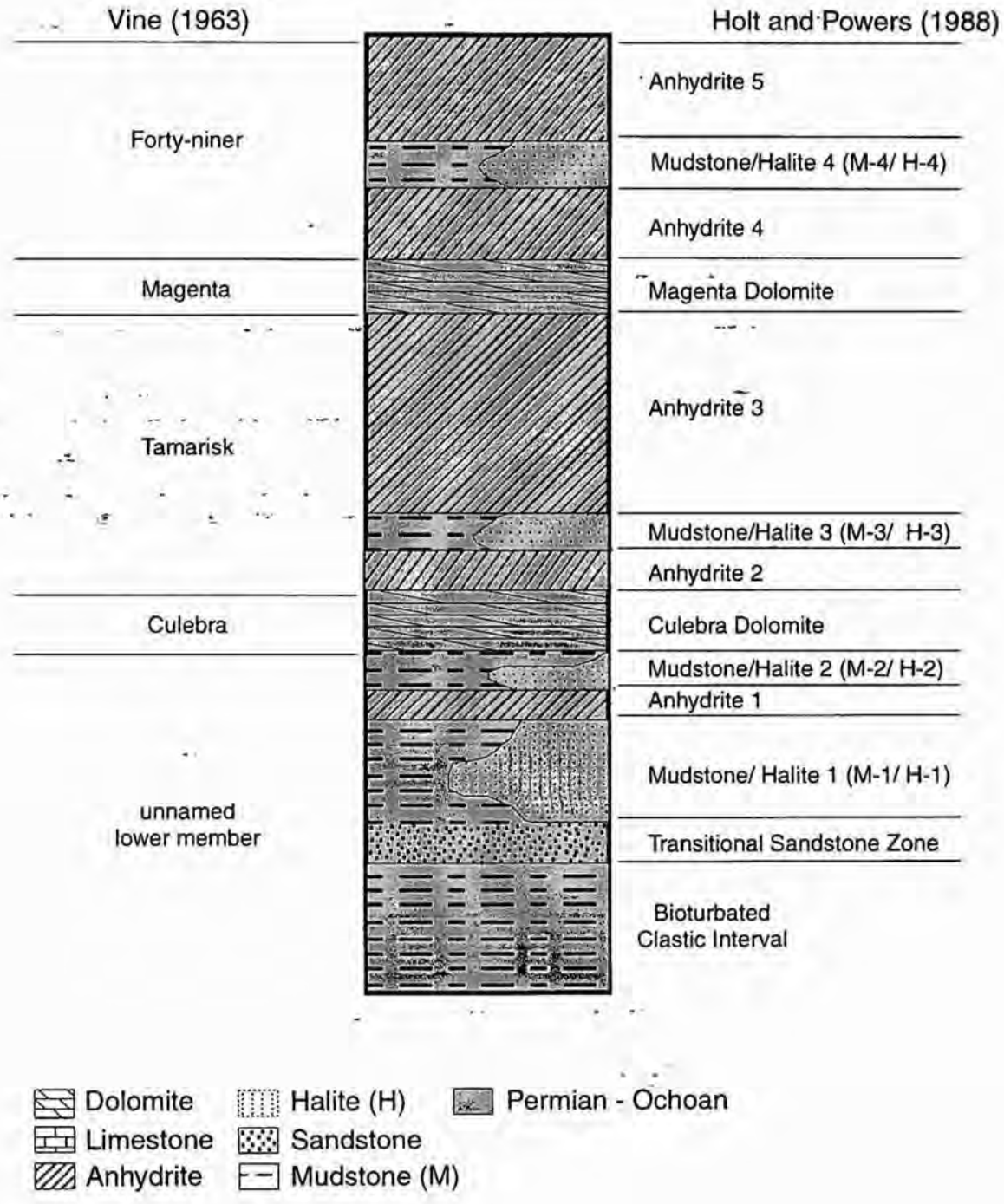

Figure 1.3. Rustler Stratigraphy

Information Only

The physical transport processes that influence actinide transport in the Culebra are advection, matrix diffusion, and dispersive spreading due to heterogeneities. Over most of the site, advective transport occurs primarily through large-aperture fractures and inter connected vugs. Tracer test conducted at the WIPP demonstrate both advective transport and matrix diffusion. Based on these test and numerous other field data, a dual-porosity conceptual model has been adopted to predict radioisotope transport within the Culebra. A detailed discussion of the Culebra conceptual model and physical transport parameters used in this analysis can be found in Meigs and McCord (1996), provided in Appendix A.

2.0 Analysis Overview

The cumulative release of radionuclides through the Culebra to the accessible environment is computed using two-dimensional groundwater flow and transport numerical models. Corbet (1996) examined the assumption of two-dimensional transport in the Culebra, and found the errors introduced by modeling the Culebra in two rather than three dimensions to be adequately small given the objective of the calculations. Flow is simulated assuming single porosity steady state flow, and radionuclide transport was modeled assuming dual-porosity transport behavior with linear equilibrium sorption isotherms. The Culebra Flow and Transport Task consist of three major processes or sub tasks, namely; generation of the transmissivity fields, groundwater flow calculations, and radionuclide transport calculations. Given the assumptions provided in Section 2.3, these sub task were completed without input data from either the Salado Flow (Task 1), or Salado Transport (Task 2) calculations. The Culebra Flow and Transport results are combined with the results of all other task in the construction of the CCDF, Smith et. al (1996).

This analysis includes dominant transport mechanisms and potential future events such as oil and gas exploration, potash mining, and climate change. Uncertainty regarding the impact of potential future events as well as imprecisely known input variables is addressed by employing a Monte Carlo analysis scheme. The WIPP performance assessment uses Monte Carlo techniques for both uncertainty and sensitivity analyses. Sensitivity analyses determine the contribution of individual input variables to the uncertainty in model predictions.

The first step in the analysis was to generate the Culebra transmissivity field (T-field) and quantify its uncertainty based on current knowledge of the site. Uncertainty in the T-field was quantified by generating a large number of plausible T-fields through geostatistical analysis. Each transmissivity field is a statistical representation of the natural variation in transmissivity which honors measured field data according to predetermined criteria. For simplicity, one T-field was generated for each set of sampled parameters used in the analysis. A sample size of 100 was chosen based on the number of uncertain parameters. Therefore, 100 different, but equally likely, representations of the Culebra transmissivity field were produced, Lavenue (1996).

The effects of potash mining are incorporated into the analysis according to the guidelines and recommendations given in 40 CFR Part 194. Mining impacts were considered by uniformly

Information Only

scaling the transmissivity in regions considered to contain economically-extractable resources by a factor of 1 to 1000. Mining effects were treated differently depending on the location of the resources with respect to the land withdrawal boundary. Outside the land withdrawal boundary, it was assumed mining will occur prior to sealing the disposal facility. Inside the land withdrawal boundary, mining will occur with a probability of 1 in 100 each century. The probabilistic aspects of mining associated with the time of occurrence within the land withdrawal boundary are accounted for in the construction of the CCDF, and discussed by Smith et. al (1996).

This analysis is essentially based on two sets of transmissivity fields; one with mining outside the land withdrawal boundary (partial mining scenario), and one with all regions mined (full mining scenario). These transmissivity fields were used to produce two sets (partial and full mining) of steady state groundwater flow fields, followed by two sets of transport simulations. The results of the transport simulations predict the movement of radioisotopes for cases in which either the full or partial mining scenario is in place for the full 10,000 year period.

The impact of potential climate variations on groundwater flow in the Culebra was addressed by uniformly scaling the x and y components of the Darcy flow velocity by a single value ranging from 1.0 to 2.25, known as the climate index. Rationale and justification for the implementation of climate change and the climate index can be found in Corbet and Swift (1996).

In the transport simulations, only dissolved species are included in the analysis. Colloid facilitated actinide transport was not included for the reasons discussed in Section 2.1. A total of four isotopes were transported; ^{241}Am, ^{239}Pu, ^{234}U, and ^{230}Th. The single decay chain of $^{234}U \rightarrow {}^{230}Th$ was also simulated in the analysis. A source consisting of a fifty year constant rate step function was injected into the Culebra beginning at time zero. The mass flux rate was specified such that one kg of each isotope was injected over the fifty year period. The source is intended to represent the discharge from an intrusion borehole penetrating the repository. For Culebra transport purposes, the intrusion is assumed to take place directly above the center of the waste-disposal region. The specific location of the intrusion borehole, in UTM coordinates is N 3,581,385.2, E 613,597.5.

The integrated release of each isotope at the land withdrawal boundary is stored as a function of time and used in the CCDF construction. These time dependent values are the primary deliverable for this task. In the CCDF construction, the linearity of the governing transport equations is exploited. Due to the linearity of this system of partial differential equations, it is possible to evaluate transport in the Culebra from a unit release, then use these results to construct transport results for any arbitrary time-dependent source, Helton and Johnson (1996, Appendix A). Consequently, to calculate the release resulting from multiple intrusions at various times, only one simulation is required per transport species for each flow field.

The equations solved to predict the movement of radioisotopes in the Culebra are linear (see Section 2.2) and can be conceptualized as a system of partial differential equations of the form,

Information Only

$$\mathbf{Lu} = \mathbf{h}, \tag{2.1}$$

where **L** is a linear differential operator, **u** is the radionuclide concentration, and **h** is a source/sink function. If $\mathbf{u}_1$ and $\mathbf{u}_2$ are solutions to

$$\mathbf{Lu}_1 = \mathbf{h}_1 \text{ and } \mathbf{Lu}_2 = \mathbf{h}_2, \tag{2.2}$$

c_1 and c_2 are constants, and $\mathbf{u} = c_1\mathbf{u}_1 + c_2\mathbf{u}_2$ then,

$$\mathbf{Lu} = \mathbf{L}(c_1\mathbf{u}_1 + c_2\mathbf{u}_2) = c_1\mathbf{Lu}_1 + c_2\mathbf{Lu}_2 = c_1\mathbf{h}_1 + c_2\mathbf{h}_2. \tag{2.3}$$

Thus, **u** is a solution to

$$\mathbf{Lu} = c_1\mathbf{h}_1 + c_2\mathbf{h}_2. \tag{2.4}$$

Therefore, if the solutions to Eq. 2.2 are known, numerous solutions to Eq. 2.4 can be obtained in highly efficient manner.

It is important to point out that in order to exploit the linearity of the governing transport equations, the source function used to construct the CCDF (Salado transport results) must be linearly dependent on the source function used in the transport simulations. To meet this requirement, the results of the Salado transport calculations are discretized into fifty year intervals during the CCDF construction. Each fifty year interval is assigned a uniform injection rate based on the cumulative mass flowing to the Culebra. The time interval of fifty years was chosen based on results from the Salado flow calculations. These results show the rate of flow up an intrusion borehole to be relatively constant over any fifty year period at the Salado / Rustler contact (Vaughn 1996, Figure 7.2.2-10).

The coupled Culebra transport solution (Salado and Culebra transport) to each fifty year window is computed by linearly scaling the results of a single transport simulation in which 1 kg of each isotope is injected at a continuous rate over a fifty year period. Using the principle of superposition, the scaled transport results of each fifty year interval are then combined to produce a unique transport solution to the coupled system. To facilitate this process, the transport results must be shifted in time. Hence, the integrated discharge of each isotope is stored as a function of time to accomodate this operation. A more rigorous discussion of the use of the Culebra transport results in the constuction of the CCDF as well as the linearity of the governing transport equations can be found in Helton and Johnson (1996).

The calculations described above were repeated three times to achieve confidence in the results. In each **Replicate**, the LHS sampling routine was re-run with a different seed to produce an entirely different set of parameter combinations. The transmissivity fields were also sampled on in each replicate so a given run number in replicate 1 has no relation to the same run number in replicates 2 or 3. To complete all three replicates, a total of 100 T-fields were generated,

Information Only

followed by 600 groundwater flow simulations, and 600 transport simulations with five independent species (for linear scaling and superposition purposes, ^{230}Th the daughter product of ^{234}U was distinguished and simulated independent of the ^{230}Th introduced in the source term).

2.1 Deviations from the Analysis Plan (AP-019)

Deviations from the analysis plan (AP-019) can categorized as mistakes and oversights or project decisions. For errors discovered in the analysis, an attempt is made to evaluate the impact of the error on the results of the analysis. Deviations from the analysis plan due to project decisions are stated and documentation supporting the decision is provided.

The first deviation from AP-019, concerns the boundary condition used in the northeastern corner of the regional groundwater modeling domain. This boundary was specified as a no flow boundary condition in the analysis, which is the same boundary condition that was imposed in the 1992 PA (WIPP 1992, pg. 6.9), and more recently in SPM2. However, the analysis plan stipulated the "boundary conditions for the regional scale simulations will be determined when the transmissivity fields are generated". During the T-field generation process, specified head boundary conditions were imposed at all boundary locations other than Nash Draw. Consequently, the stated boundary condition in the analysis plan was not used in the performance assessment.

The use of a no-flow versus a specified head boundary condition at this location was an oversight, carried on from previous performance assessments. The mistake is believed to have no impact on the results of the analysis. Support for this opinion is presented in Appendix B, Figures B1 to B8, where the effect of the boundary condition imposed on the northeastern corner is shown for two randomly selected runs; R1_V100_FM and R1_V030_PM. Notice only a slight change in the regional solutions, Figures B1, B2, B5, and B6, and no detectable change in the local solutions, Figures B3, B4, B7, and B8. Because the local groundwater flow solutions do not appear to be influenced by the choice of boundary condition at this particular location, the results of the transport simulations will not be affected either.

The second deviation from AP-019 involves a coding error in PRESECOTP2D which led to an error in the source term of ^{230}Th. The error had the effect of reducing the cumulative mass of ^{230}Th injected by a factor 256. Consequently, only 1/256 kg of ^{230}Th was injected over a 50 year period. The error had no ramifications on the remaining isotopes or on the daughter product ^{230}Th solution. Also, because the integrated discharge of injected ^{230}Th was exceptionally low in all simulations, the error in the integrated discharge is not detectable in the single precision format which is used by the code to output results (Blaine 1996). Therefore, the error is considered to have no impact on the primary deliverable "isotope integrated discharge". The reader is referred to Blaine (1996), included in Appendix B for more details regarding this subject.

One additional error has been identified involving the parameter ranges for the matrix distribution coefficients, or k_d's. The k_d parameter ranges used in the CCA were those provided

Information Only

by Brush (1996) who latter found an error in the data used to establish the parameter ranges. The revised parameter ranges are given by Brush and Storz (1996), included in Appendix B. For comparison, both parameter ranges are presented in Table 1.1.

Table 1.1 Comparison of Matrix Distribution Coefficients

Isotope (Oxidation State)	CCA k_d Range (m^3/kg) (Brush, 1996)	Revised k_d Range (m^3/kg) (Brush and Storz, 1996)
$^{234}U(IV)$	0.9 to 20	0.7 to 10
$^{234}U(VI)$	0.00003 to 0.03	0.00003 to 0.02
$^{239}Pu(III)$	0.02 to 0.5	0.02 to 0.4
$^{239}Pu(IV)$	0.9 to 20	0.7 to 10
$^{241}Am(III)$	0.02 to 0.5	0.02 to 0.4
$^{230}Th(IV)$	0.9 to 20	0.7 to 10

Notice the revised parameter ranges are somewhat lower than the those used in the CCA, and that the minimum value was reduced for U, Pu, and Th in the (IV) oxidation state. The minimum value was reduced from 0.9 to 0.7 (m^3/kg), and the maximum was reduced from 20 to 10 for these species. However, the revised parameter range is still rather large, so the overall transport behavior of the species will not be considerably different. This position is supported by the fact no $^{239}Pu(III)$, which has much lower k_d's, managed to reach the land withdrawl boundary in the CCA calculations.

In Section 7.2, it is shown that significant releases were computed only when the sampled k_d approached the minimum value of the U(VI) distribution. Because the minimum values (except as noted above) were unchanged, it is highly probable the revised ranges for the matrix distribution coefficient will have no impact on the results of this analysis.

The remaining deviations from AP-019 consist of project decisions made in the light of new analysis and experimental data. The first decision was to reduce the number of isotopes considered in the transport simulations from ten to four. The rationale for this decision is documented in Garner (1996), also included in Appendix B.

The second decision was to not include colloid-facilitated actinide transport in the performance assessment. Rationale for this decision is based on the experimental results reported by Papenguth (1996), which show that colloid-facilitated actinide transport is not a significant transport mechanism at the WIPP. Specifically, the experiments demonstrate that mineral fragments and microbes are attenuated so effectively in the Culebra that it was deemed unnecessary to include them in the performance assessment calculations, Perkins (1996). Additionally, under the neutral to slightly basic geochemical conditions expected in the Culebra, complexation of actinides by humic substances was found to be insignificant, The only actinide-intrinsic colloid of potential concern at the WIPP is the Pu(IV) polymer. However, based on

Information Only

estimates of the Pu(IV) polymer inventory it was determined the quantity of the colloid is so small it could be safely ignored, Stockman (1996).

It is possible that indigenous colloids in the Culebra will react with dissolved actinides to create new colloidal actinides. However, newly formed, actinide-bearing microbial and mineral fragment colloids will be attenuated in the same manner as colloids introduced from a drilling intrusion. Disregarding the impact of indigenous microbes and mineral fragments is a conservative approach due to the high degree of filtration observed with these colloid types. Indigenous humic substances are also not of concern for the reasons given above; actinides do not complex with humics under the pH conditions expected in the Culebra (nominally 7.5). Finally, conditions in the Culebra are not conducive to the formation of Pu(IV) polymer.

2.2 Software Requirements

The analysis plan for the Culebra Flow and Transport Task contains three major processes or Sub Tasks (see Ramsey, 1996, for a description of all Sub Task). The principal numerical models used to complete each of the three major Sub Tasks are listed in Table 2.1.

Table 2.1 - Culebra Flow and Transport Models

Sub task	Description	Code Name	Version Number
3	Transmissivity Fields	GRASPINV	2.01
5	Groundwater Flow	SECOFL2D	3.03
7	Radionuclide Transport	SECOTP2D	1.30

Sub Task 3 consisted of the probabilistic generation of the Culebra transmissivity field. The numerical model GRASPINV was used to perform this task and is discussed by Lavenue (1996).

The groundwater flow simulations, Sub Task 5, were completed using SECOFL2D. SECOFL2D is a two dimensional groundwater flow model capable of simulating transient or steady state flow in saturated and unsaturated porous media. The governing equation solved by SECOFL2D for confined aquifers is (Roache et al., 1996),

$$S\left(\frac{\partial h}{\partial t}\right) = \nabla(bK\nabla h) - Q \qquad (2.5)$$

where, S is the medium storativity (dimensionless), h is the hydraulic head (m), t is the time (s), b is the aquifer thickness (m), K is the hydraulic conductivity (m s^{-1}), and Q is a source/sink term expressed as the volumetric flux per unit area (m s^{-1}).

Groundwater transport simulations, Sub Task 7, were completed using SECOTP2D. SECOTP2D is a two dimensional dual porosity transport model developed to simulate radionuclide transport through fractured porous media. The code assumes parallel plate type fracturing where fluid flow (advection) is restricted to the advective continuum (fractures), and mass is transferred between the advective and diffusive continuum (matrix) via molecular

Information Only

diffusion. Retardation is permitted in the both the advective and diffusive continuum assuming linear equilibrium sorption isotherms. Radioactive decay is accounted for in the model through the use of multiple straight decay chains.

The governing equation solved by SECOTP2D for the advective continuum is (Salari and Blaine 1996),

$$\nabla\left[\phi\mathbf{D}\nabla C_k - \mathbf{V}C_k\right] = \phi R_k\left(\frac{\partial C_k}{\partial t}\right) + \phi R_k\lambda_k C_k - \phi R_{k-1}\lambda_{k-1}C_{k-1} - Q_k - \Gamma_k \qquad (2.6)$$

where, the concentration of the kth radionuclide, C_k, is the dependent variable (kg m^{-3}). Eq. 2.6 is linear and solved simultaneously for each species of a given decay chain, where k = 1,...,N (N being the total number of species in the decay chain). Terms involving C_{k-1} are omitted for the parent of a decay chain, k = 1. The parameters in Eq. 2.6 consist of; **D**, the hydrodynamic dispersion tensor (m^2 s^{-1}), **V**, the specific discharge (m s^{-1}), ϕ, the effective porosity defined as the ratio of the inter-connected advective pore volume to the total or bulk volume (dimensionless), R_k, the advective retardation coefficient (dimensionless), λ_k, the radioactive decay constant (s^{-1}), and Q_k, the specific injection rate defined as the rate of mass injected per unit bulk volume (kg s^{-1} m^{-3}).

The product $\phi\mathbf{D}$ in Eq. 2.6 is defined as,

$$\phi\mathbf{D} = \frac{1}{|\mathbf{V}|}\begin{bmatrix} u & -v \\ v & u \end{bmatrix}\begin{bmatrix} \alpha_L & 0 \\ 0 & \alpha_T \end{bmatrix}\begin{bmatrix} u & v \\ -v & u \end{bmatrix} + \phi\tau D_k^* \qquad (2.7)$$

where, α_L and α_T are the longitudinal and transverse dispersivities (m), u and v are the x and y components the specific discharge (m s^{-1}), D_k^*, the free water molecular diffusion coefficient (m^2 s^{-1}), and τ is the advective tortuosity defined as L/L_e (dimensionless) where, L denotes the length of the porous medium (m), and L_e denotes the flow path length of a fluid particle (m).

The partial differential equation describing transport through the advective continuum is coupled implicitly and solved simultaneously with a one-dimensional diffusion equation describing transport in the diffusive (matrix) continuum,

$$\frac{\partial}{\partial\chi}\left(\phi' D' \frac{\partial C_k'}{\partial\chi}\right) = \phi' R_k'\left(\frac{\partial C_k'}{\partial t}\right) + \phi' R_k'\lambda_k C_k' - \phi' R_{k-1}'\lambda_{k-1}C_{k-1}' \qquad (2.8)$$

where, χ is the spatial coordinate system shown Figure 2.1, and D′ is the matrix diffusion coefficient (m^2 s^{-1}) defined as, $D' = D_k^* \tau'$, where τ' is the matrix tortuosity. The remaining symbols have the same meaning as those in Eq. 2.6 except that the prime denotes diffusive continuum properties.

The initial and boundary conditions employed to solve Eq. 2.8 are,

Information Only

$$C_k'(\chi,0) = 0 \tag{2.9}$$

$$\frac{\partial C_k'}{\partial \chi}(0,t) = 0 \tag{2.10}$$

$$C_k'(B,t) = C_k(x,y,t) \tag{2.11}$$

where, B is the matrix block half length (m).

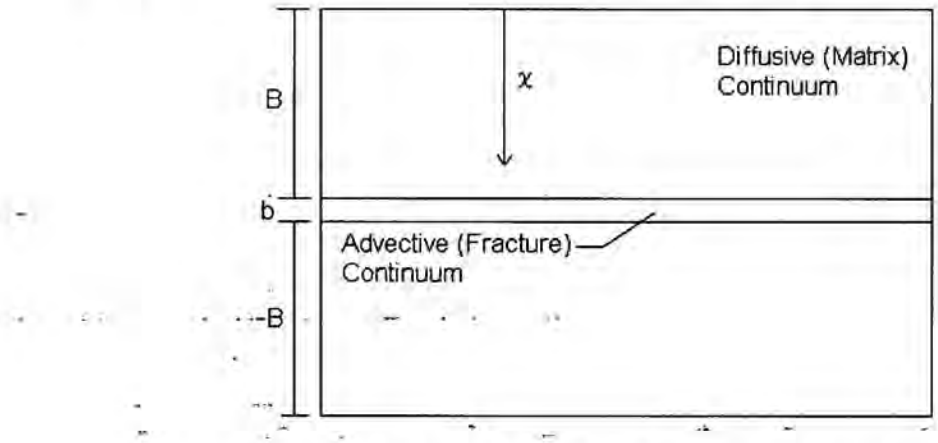

Figure 2.1. Parallel plate dual porosity conceptualization

The equations for the advective and diffusive continua are coupled through the mass transfer term, Γ_k, and the application of Fick's law at the interface between the two continua. The equation describing this transfer of mass is given by,

$$\Gamma_k = -\frac{2\phi}{b}\left(\phi' D' \frac{\partial C_k'}{\partial \chi}\bigg|_{\chi=B}\right) \tag{2.12}$$

where, b is the fracture aperture in the parallel plate formulation (m), defined as,

$$b = \frac{\phi B}{1-\phi} \tag{2.13}$$

The term $2\phi/b$ in Eq. 2.12, represents the specific surface area (ratio of surface area to bulk volume) of the coupled system.

In the analysis, no credit is taken for retardation in the advective continuum (i.e. sorption on clay linings on fracture surfaces). Hence, R_k was set to one for all isotopes. Retardation is however, accounted for in the diffusive continuum and derived from the matrix distribution coefficient by,

Information Only

$$R_k' = \frac{\rho_s(1-\phi')(k_d)_k}{\phi'} + 1 \qquad (2.14)$$

where, ρ_s is the grain density of Culebra Dolomite (kg m^{-3}), and $(k_d)_k$ is the matrix distribution coefficient (m^3 kg^{-1}).

For sub tasks 5 and 7, additional codes are required to preprocess input parameters and post process results. The pre/post processors used are listed in Table 2.2.

Table 2.2 - Pre/Post Processors

Sub Task	Description	Code Name	Version Number
5	Mesh Generation	GENMESH	6.08
	SECOFL2D Preprocessor	PRESECOFL2D	4.05
	SECOFL2D Postprocessor	POSTSECOFL2D	4.04
	Binary to ASCII processor	SUMMARIZE	2.10
7	SECOTP2D Preprocessor	PRESECOTP2D	1.20
	SECOTP2D Postprocessor	POSTSECOTP2D	1.02
5 & 7	Parameter Specification	MATSET	9.00
	LHS preprocessor	PRELHS	2.10
	Latin Hypercube Sampling	LHS	2.41
	LHS postprocessor	POSTLHS	4.07
	Parameter Manipulation	ALGEBRACDB	2.35
	Parameter Transfer	RELATE	1.43
	Plotting Package	BLOTCDB	1.37

The above codes are located in the WIPP Software Configuration Management System (SCMS) and were run on the WIPP Alpha Cluster. All codes used in the analysis were qualified per QAP 19-1.

One additional code was used , which is not included in the WIPP SCMS. The name of the code is TRACKER (Version 5.01Z0). TRACKER is part of the SECO suite of numerical models used to analyze the results of the groundwater flow calculations. TRACKER was used to predict the travel path and travel time of non-reactive non-sorbing particles released into the Culebra in the waste panel area. As required by QAP 9-1, Appendix B, a listing of the source code and code verification are included in Appendix C of this document.

2.3 Assumptions

The intent of this analysis was to incorporate dominant transport mechanisms and potential future events in a computationally feasible manner. To do this a number of assumptions were made about the system being modeled to simplify the computational process. Most assumptions are presumed to have little or no impact on the integrated release of radionuclides, particularly

Information Only

after considering the overwhelming effects of mining and climate variations. Others can be characterized as conservative; meaning they are expected to over predict radionuclide releases.

Assumption 1. *Steady state flow conditions can be used to adequately describe groundwater flow in the Culebra.* This assumption is based on the fact that there are no current or anticipated activities involving pumping from or injection to the Culebra that would impact transport in the area of concern (Bertram, 1996, Wallace, 1996a). This assumption also suggest that the transient effects of climate change and fluid discharges from intrusion boreholes can be neglected.

Potential climatic changes could lead to an increase in hydraulic gradients in the Culebra member. The influence of climate change is incorporated into the analysis by uniformly increasing the calculated steady state velocity fields at the beginning of the simulation (Corbet and Swift, 1996). *Since climate changes, as implemented in this analysis will only accelerate transport, applying the effect of the climate change at the beginning of the simulation is a conservative assumption.*

Flow perturbations resulting from intrusion boreholes are likely to have a local influence on the flow and transport of radionuclides in the Culebra. However, because brine released from an intrusion borehole was shown in the Salado flow calculations to be relatively small ($< 6\ m^3$/yr, Vaughn 1996, Figure 7.2.2-10), the regional flow field should not be affected. Thus, *flow field perturbations due to intrusion boreholes are assumed to have little or no influence on the integrated release of radionuclides and were therefore neglected.*

Assumption 2. *Fluid density and viscosity changes initiated by the release of borehole fluids are assumed to be negligible.* This assumption is based on the relatively small brine inflow results discussed above and the assumption of little or no regional effects.

Assumption 3. *Spatially averaged, constant transport parameters can be used to describe the behavior of a heterogeneous fractured porous medium.* Transport parameters used in the analysis consisted of spatially averaged effective properties which incorporated the effects of heterogeneities. These parameters were varied in the analysis from one run to the next to capture the uncertainty in heterogeneity.

Assumption 4. *An intrusion borehole positioned at the center of the waste disposal region acceptably approximates the potential range of intrusion locations.* This is true even though a weak correlation between borehole position and particle travel time (east positions faster than west) was observed by Wallace (1996b). Particles released near the center of the waste disposal region generally exhibit travel times somewhere between that of particles released at each end of the disposal facility. Therefore, the center of the waste disposal region functions as

Information Only

a mean release point with respect to particle travel time. Furthermore, travel times were found to be far more sensitive to the transmissivity field and mining effects than to the location of the release point Wallace (1996b). Consequently, a more rigorous approach of sampling on the release position would likely have little or no influence the transport results.

2.4 Data Sources

The input data required to generate the Culebra transmissivity fields consisted of point transmissivity values, transient head data, fluid density, pore compressibility, porosity, Culebra elevation and thickness, and steady state fresh water heads. The source of these data is given by Ruskauff (1996), and the data have been qualified through application of QAP 20-3, QAP 9-2, or by SNL WIPP audit. Because SECOFL2D requires hydraulic conductivity K, as a model input parameter rather than transmissivity, GRASPINV reports hydraulic conductivity. A memorandum indicating the GRASPINV output appears to be reasonable and suitable for use by PA is included in Section B-7 of Appendix B.

Flow in the Culebra is thought to be concentrated within zones that are thinner than the total thickness of the Culebra. In general, the upper portion of the Culebra contains few fractures and vugs, and is consequently low in permeability. Where as the lower portion of the Culebra generally contains many more fractures and vuggy zones resulting in significantly higher permeability. The hydraulic conductivity fields produced by GRASPINV were computed based on the total thickness of the Culebra (THICK), 7.75 m, rather than the effective thickness (ETHICK), 4.0 m. In the transport simulations only the effective flow domain is considered however, so it was necessary to modify the hydraulic conductivity fields in a manner to conserve transmissivity. The procedure used to compute hydraulic conductivities representative of the effective Culebra thickness was simply to recompute transmissivity then divide by the effective thickness, K(ETHICK) = K(THICK) * THICK / ETHICK.

The resultant hydraulic conductivity fields, are combined with additional parameters obtained from the controlled PA parameter data base. All parameters, except hydraulic conductivity, are assumed to be spatially constant (see assumption #3). The specific input data including cumulative distribution diagrams and tables of sampled variables are provided in Appendix D.

The Replicate 1, sampled parameter values are plotted on the cumulative distribution diagrams in Appendix D. Because the plotting package used to generate these diagrams computes the cumulative probability of each sample point based on the distribution of the data rather than the known probability distribution, the sampled points do not fall precisely on the diagram. The cumulative probability of each sampled data value is therefore an estimate of that probability rather than the actual probability. These diagrams serve as both an illustration of the parameter distributions as well as a check of the LHS output.

The matrix distribution coefficient, k_d, and free water molecular diffusion coefficient, D^*, are dependent on the oxidation state of the element. Of the radioisotopes modeled, the oxidation

Information Only

states of ^{234}U and ^{239}Pu are considered to be uncertain. The possible oxidation states for ^{234}U are (IV) and (VI), and the possible oxidation states of ^{239}Pu are (III) and (IV). The uncertainty in oxidation state and resulting influence on transport parameters is captured by first sampling on the oxidation state. The parameter distribution for the oxidation state (OXSTAT) is uniform ranging from 0 to 1. When OXSTAT > 0.5 the elements are assumed to be in a "high" oxidation state, U(VI) and Pu(IV). Otherwise, the elements are assumed to be in a "low" oxidation state, U(IV) and Pu(III). Once the oxidation state of the element has been determined, the values of k_d and D^* are obtained from the corresponding parameter distribution.

Model configuration parameters used in the analysis consist of the fracture tortuosity, and skin resistance. Fracture tortuosity, τ (FTORT in Appendix D), was set to a value of one due to insufficient data to support any other value. The rationale for setting $\tau = 1$, is it is the most conservative value this parameter can have and it is a common practice to do so. The skin resistance parameter, ζ (SKIN_RES in Appendix D), is used by SECOTP2D to simulate retardation within clay linings along fracture walls, Salari and Blaine (1996). Because the Project has elected to not take credit for sorption by clay minerals on fracture surfaces, ζ was set to zero which disables this feature of the code..

The longitudinal and transverse dispersivities provided in Appendix D are equal to zero. The rationale and justification for using zero dispersivities is provided in Appendix A. Small dispersivities are usually problematic when attempting to solve the advection-diffusion transport equation (Eq. 2.6) due to oscillatory behavior at the concentation front (Pinder and Gray, 1977, p. 150-169). Most transport simulators address this problem by including the option to invoke an upsteam weighting technique. Upstream weighting reduces numerical oscillations by introducing numerical dispersion and thus smearing the concentration front. SECOTP2D, however, includes the option to use a total variation diminishing (TVD) technique. TVD also introduces numerical dispersion but does so selectively in an attempt to minimize additional dispersion.

One additional parameter, the Culebra bulk compressibility was derived from the Culebra storativity, total thickness, diffusive porosity, and assumed values of the brine specific weight and brine compressibility (see input file ALG_SF2D_CCA_FM.INP in Appendix E). Ultimately, the derived bulk compressibility is used by the groundwater flow model preprocessor, PRESECOFL2D, to recompute storativity. The values used for brine specific weight and brine compressibility are the PRESECOFL2D default values. Hence, the result of this process is the original value of storativity obtained from controlled parameter data base is input to SECOFL2D.

It is important to note that for steady state calculations the storativity computed by the preprocessor is not used by the simulator. Any value of bulk compressibility (within the range limits of the preprocessor) will produce the same steady state flow field. The preprocessor however, requires a value of bulk compressibility be supplied regardless of the nature of the simulation. Since a value must be supplied an effort was made to provide the code with a reasonable value that is consistent with other relevant parameters.

Information Only

2.5 Initial and Boundary Conditions

2.5.1 Groundwater flow

The SECOFL2D dependent variable solved for is freshwater head. Because steady state simulations were performed, it was not necessary to prescribe initial head levels.

Groundwater flow in the Culebra is computed at both a regional and local scale. The purpose of the regional simulation is to incorporate natural flow boundaries into the problem domain that may influence the magnitude and direction of flow in the region of interest. Regional scale simulations were performed over a large problem domain using a relatively coarse computational grid. The results of the regional scale simulations are used to interpolate boundary conditions at the local scale. This modeling approach allows the use of high resolution computational grids in the region of interest, and the incorporation of natural flow boundaries at a much larger scale.

In Figure 2.2, both the regional and local model domains are superimposed on a topographic map of the area surrounding the WIPP. The regional domain is approximately 22 by 30 km and aligned with the axis of Nash Draw along a portion of the western boundary. The computational grid and imposed boundary conditions of the regional domain are shown in Figure 2.3. The grid contains 108 columns and 100 rows resulting in 10,800 grid blocks.

Nash Draw is a topographic low created by the dissolution of halite beneath Rustler Formation. As a consequence of this dissolution, the Rustler has subsided and the contact between the Rustler and Salado Formations consist of an unstructured residuum of gypsum, clay, and sandstone. The residuum is highly conductive and known to discharge to the surface into saline lakes, Hunter (1985). Test wells in the southern portion of Nash Draw produced brine from this interval, and it has become known as the brine aquifer, Figure 2.4.

Robinson and Lang (1938) described the brine aquifer and suggested that the structural conditions which caused the development of Nash Draw may control the occurrence of brine. Thus, the brine aquifer boundary may coincide with the topographic surface elevations of Nash Draw. Drilling associated with the WIPP hydrogeologic studies in the northern half of Nash Draw support this theory.

Groundwater divides are boundaries across which it is assumed that no groundwater flow occurs. Topography and surface-water drainage patterns often provide clues to the location of groundwater divides. Ridges between creeks and valleys may serve as recharge-type divides, and rivers, lakes, or topographic depressions may serve as discharge-type divides.

The axis of Nash Draw is assumed to behave hydraulically as a discharge-type groundwater divide. The basis for this assumption is the known topographic and geologic discharge features of Nash Draw. Consequently, that portion of the western boundary oriented along the axis of Nash Draw is modeled using a no flow boundary condition.

Information Only

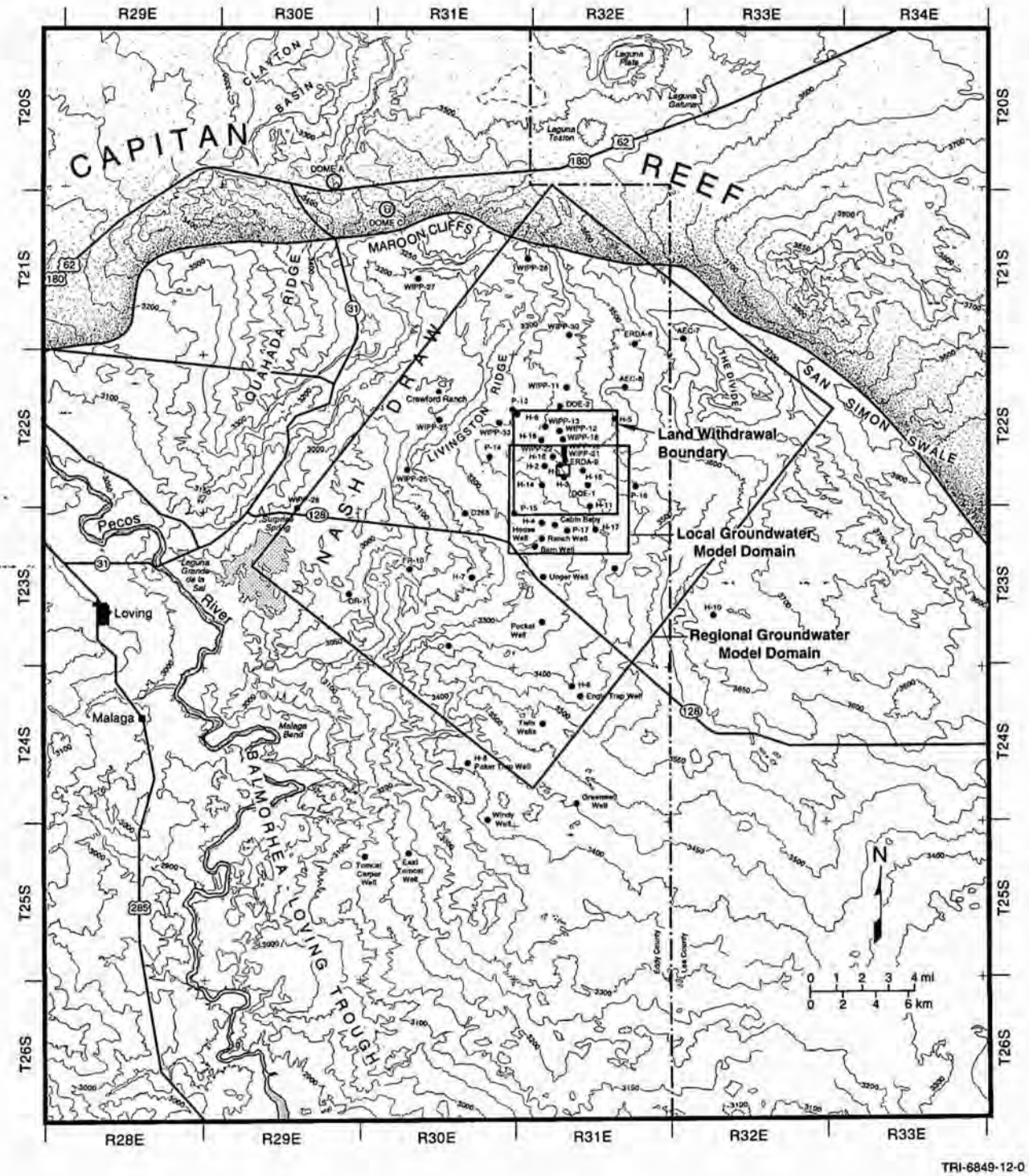

Figure 2.2. The Regional and Local Domains Used in the Horizontal Groundwater Model of the Culebra

Information Only

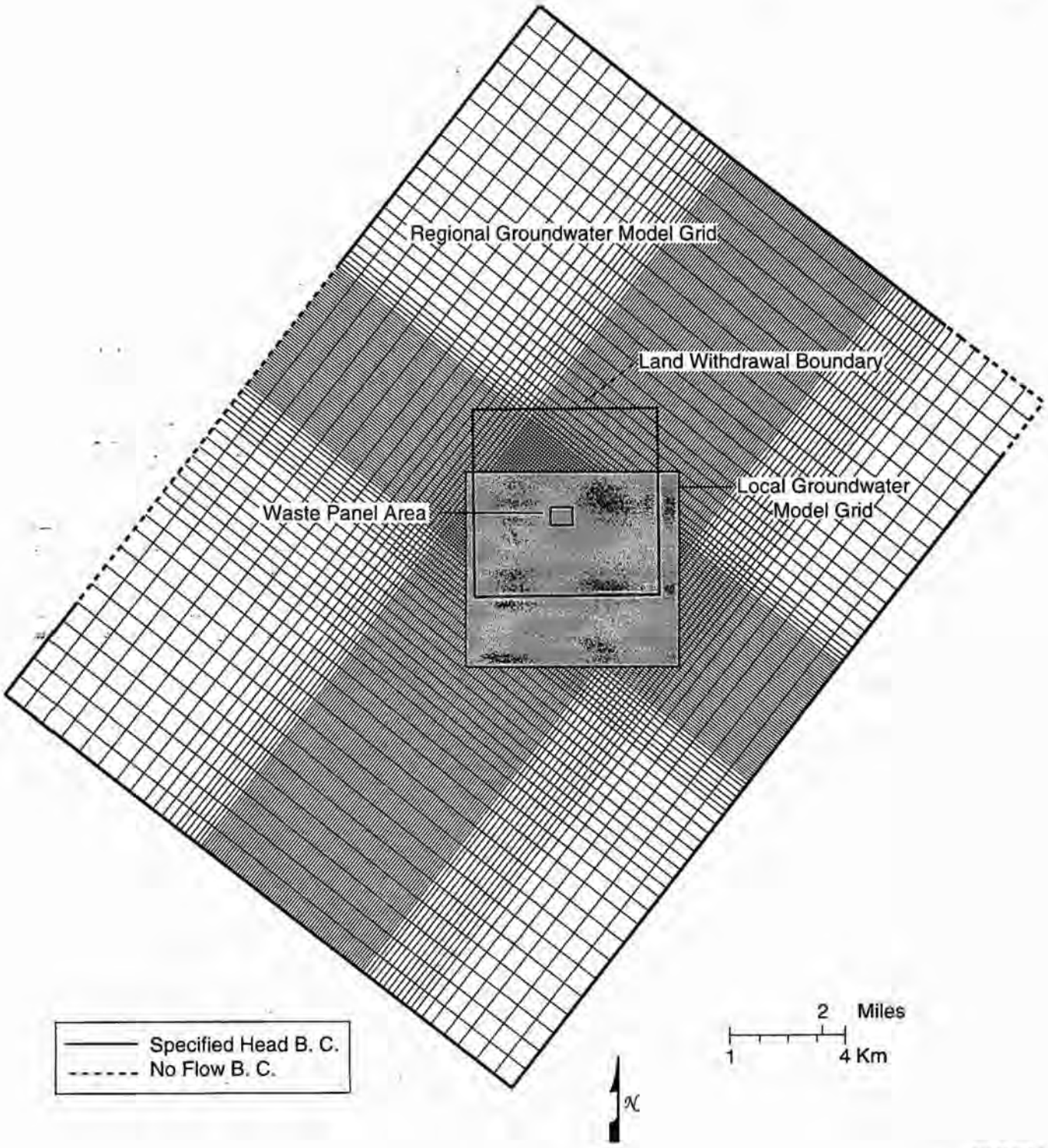

Figure 2.3. Regional Model Domain Spatial Discretization and Boundary Conditions

Information Only

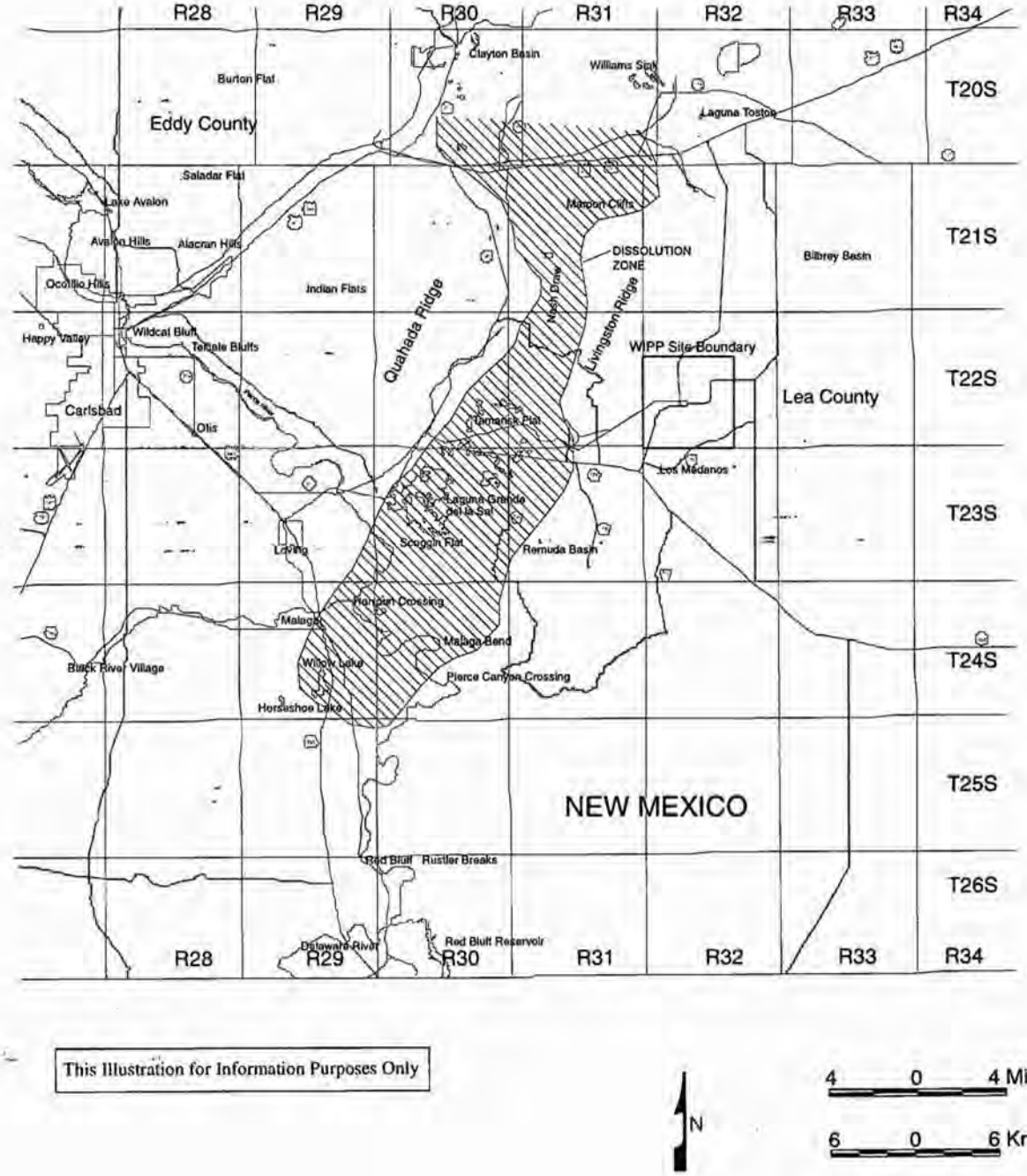

Figure 2.4. Brine Aquifer in the Nash Draw

Information Only

The remaining regional boundary conditions are not as well defined. When possible, they were positioned to align with topographic highs or other geologic features such as San Simon Swale on the northeastern boundary. Due to their uncertainty, the boundaries are positioned a large distance from the local problem domain. This is done to reduce the influence of these boundary conditions on the solution in the region of interest. Due to the relative abundance of head data near the site, Dirichlet (constant head) boundary conditions were intended to be imposed at all boundary locations other than Nash Draw. This approach was followed except in the northeastern corner of the problem domain where a no-flow boundary condition was used instead of a specified head boundary condition.

In all past performance assessments of the WIPP, the northeastern corner of the regional domain has been modeled using no-flow boundary conditions. No-flow boundary conditions were used in the past because the observed transmissivities tend to be low in this region and the northeastern corner lies roughly within the San Simon Swale. It was our intention to change this boundary condition to a more consistent specified head boundary condition, however, the change was unfortunately not made. The oversight is not thought to influence the flow field at the local scale, however. A short discussion, including simulations with both types of boundary conditions is included in Section 2.1.

The WIPP land withdrawal boundary, local grid domain, and the waste panel area, are superimposed on the regional grid in Figure 2.3. The local domain boundaries were selected to capture important flow paths and facilitate the computation of integrated discharges across the land withdrawal boundary. The results of previous performance assessments in conjunction with preliminary test simulations revealed the dominant groundwater flow pattern is from the north to the southeast or southwest. To maximize problem resolution and minimize computational requirements a portion of the land withdrawal boundary in the northern section was excluded from the local model domain. Therefore, the local domain encompasses most of the land withdrawal boundary and extends slightly beyond the eastern, and western borders. The position of the southern boundary was chosen to minimize fluid velocity contrast at the boundary. Large velocity contrast on the model domain boundary have been found to be create numerical problems for the transport simulator.

The computational grid of the local domain is shown in Figure 2.5. The local domain is approximately 7 by 7 km. The grid contains 75 columns and 65 rows resulting in 4875 grid blocks. Boundary conditions imposed on the local domain were chosen to be Dirichlet and derived from the regional head solution using a bi-linear interpolation scheme. The hydraulic properties in the local domain were also determined through interpolation of the regional domain. The same bi-linear interpolation scheme was used to assign hydraulic conductivities in the local domain.

This technique of coupling the local flow simulation to the hydraulic properties and solution of the regional model has been used quite successfully in past performance assessments. However, the hydraulic conductivity fields used here possess a higher degree of variation (generally, several orders of magnitude variation) between neighboring elements than the hydraulic

Information Only

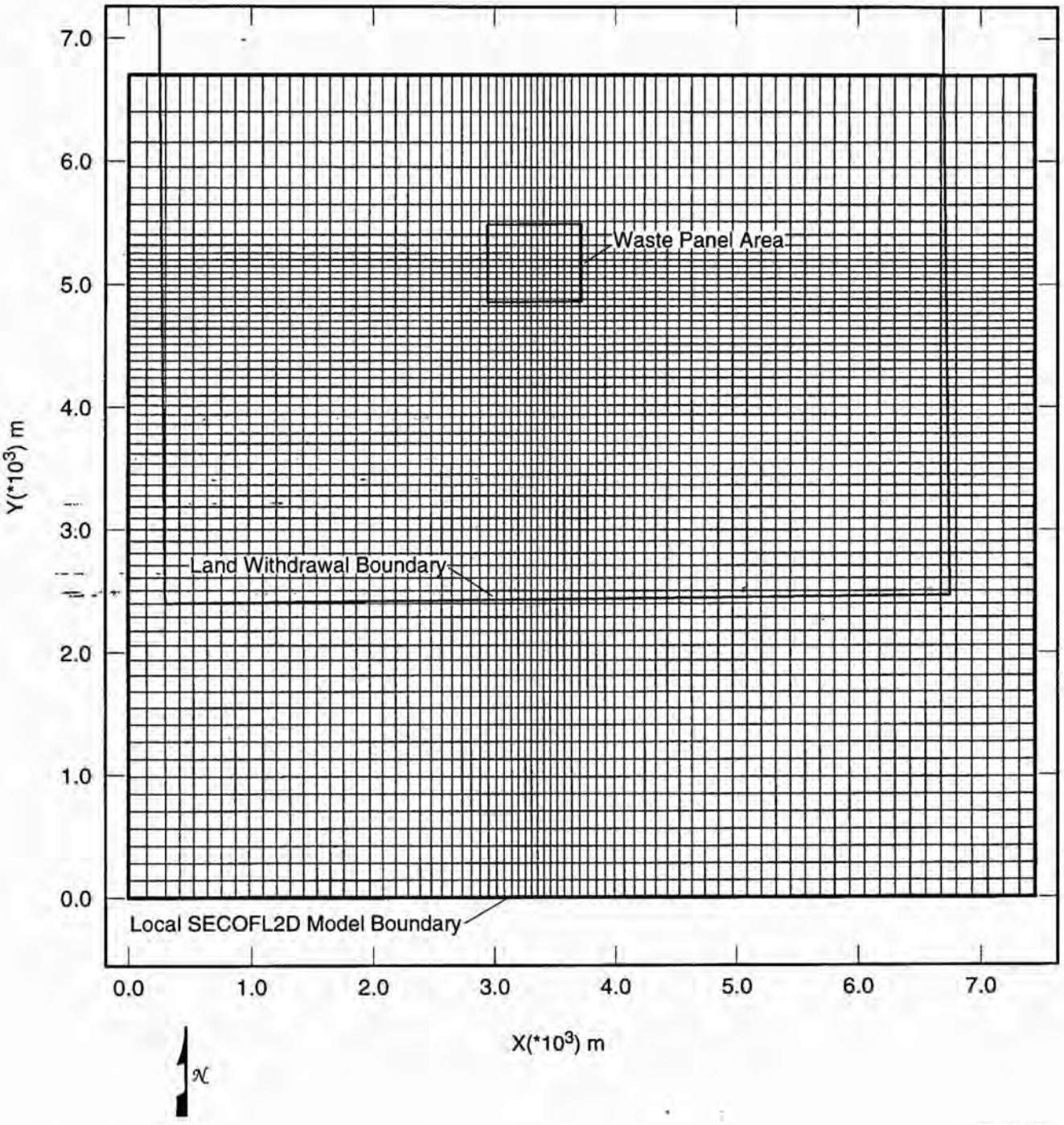

Figure 2.5. Local Domain Discretization

Information Only

conductivity fields used in the past. The increased local variation in hydraulic conductivity was not anticipated, nor were the ramifications of this change considered prior to performing the analysis. It is apparent now, however, that a more appropriate interpolation scheme should have been used to determine the hydraulic conductivity at the local scale.

The problem with the bi-linear interpolation scheme is that when the value of one or more of the interpolation points is substantially larger than its neighbors, the interpolated data are dominated by the large values. Because the regional hydraulic conductivities vary several orders of magnitude between adjacent elements in certain locations, the interpolated hydraulic conductivities in the local domain are somewhat on the high side. Hence, the computed flow fields are also on the high side and most likely overestimate transport.

2.5.2 Groundwater transport

In the transport simulations, the dependent variable solved for by SECOTP2D is isotope concentration. The initial isotope concentration was assumed to be zero, and the boundary conditions were automatically controlled by SECOTP2D. The SECOTP2D automatic boundary condition option uses the direction of flow to set the boundary condition type. At boundary locations where the flow direction is outward and therefore leaving the computational domain, a zero concentration gradient Neumann boundary condition is imposed. At boundary locations where the flow directions is inward, a zero concentration Dirichlet boundary condition is used.

Spatial discretization of the diffusive (matrix) continuum is accomplished using the grid stretching algorithm in PRESECOTP2D. The equation used to discretize the matrix domain is,

$$\Delta\ell_i = \Delta\ell_o(1+\varepsilon)^i \quad \text{for } i = 1, n-2 \tag{2.15}$$

Eq. 2.15 is written in dimensionless form such that, $\Delta\ell_i = \Delta\chi_i / B$, where $\Delta\chi_i$ is the length of grid block i (m), and B is the matrix block half length (m). The total number of nodes, n, and the size of the first grid block in relative terms, $\Delta\ell_o$, are supplied to the preprocessor which then computes ε such that,

$$\Delta\ell_o + \sum_{i=1}^{n-2} \Delta\ell_i = 1 \tag{2.16}$$

In each transport simulation, n was set to 20, and $\Delta\ell_o$ was chosen to be 10^{-3}. The resulting nodal positions in dimensionless space are shown in Figure 2.6.

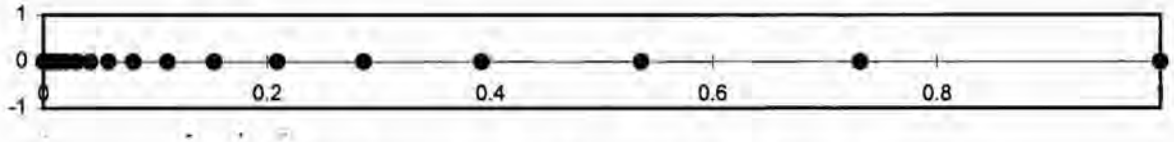

Figure 2.6. Diffusive Continuum Spatial Discretization

Information Only

2.6 Potash Mining

The maps used to implement the effects of potash mining on flow and transport in the Culebra are presented in Figures 2.7 and 2.8. Figure 2.7, shows the impacted areas when mining takes place outside the land withdrawal boundary (partial mining scenario), and Figure 2.8 shows the impacted area if all economically-extractable potash is mined (full mining scenario). The basis and rationale for these maps can be found in Wallace (1996b). In the analysis, the hydraulic conductivity of each grid block in the computational mesh shown in white was multiplied by a single value obtained by sampling from the parameter distribution of the potash mining multiplier. The potash mining multiplier parameter distribution, MINP_FAC, consist of a uniform distribution possessing a range from 1 to 1000 (see Appendix D).

For about a third of the realizations, the full mining scenario was not invoked in the 10,000 year period. For these realizations, the transport results of the partial mining scenario can be used directly to compute releases at the land withdrawal boundary. However, in the remaining two third realizations, it was necessary to account for changes in the velocity field in both direction and magnitude due to mining inside the land withdrawal boundary. To incorporate this scenario in the performance assessment in a computationally efficient manner, it was necessary to simplify the transport problem. The simplification is that isotopes released prior to the time of full mining are assumed to be transported by the partial mining flow field from the time of release to the end of the 10,000 year regulatory period. Isotopes released after the time of full mining are transported according to the full mining flow field.

An important limitation of this simplifying assumption is that isotopes released prior to the time of full mining are never influenced by the full mining flow field. Obviously, if at some point in time the flow field were to change, one would expect isotopes in transit to follow the new flow field rather than the old. This assumption is defendable however, because the results are generally conservative with respect to transport. The basis for considering the assumption to be conservative is that the effect of mining inside the land withdrawal boundary tends to alter the direction of flow in a manner that is beneficial to compliance (see Section 7.1). Therefore, by continuing to use the partial mining flow field for isotopes already in transit, when conceptually the full mining flow field should be in invoked, it is presumed isotope discharges will generally be greater.

Information Only

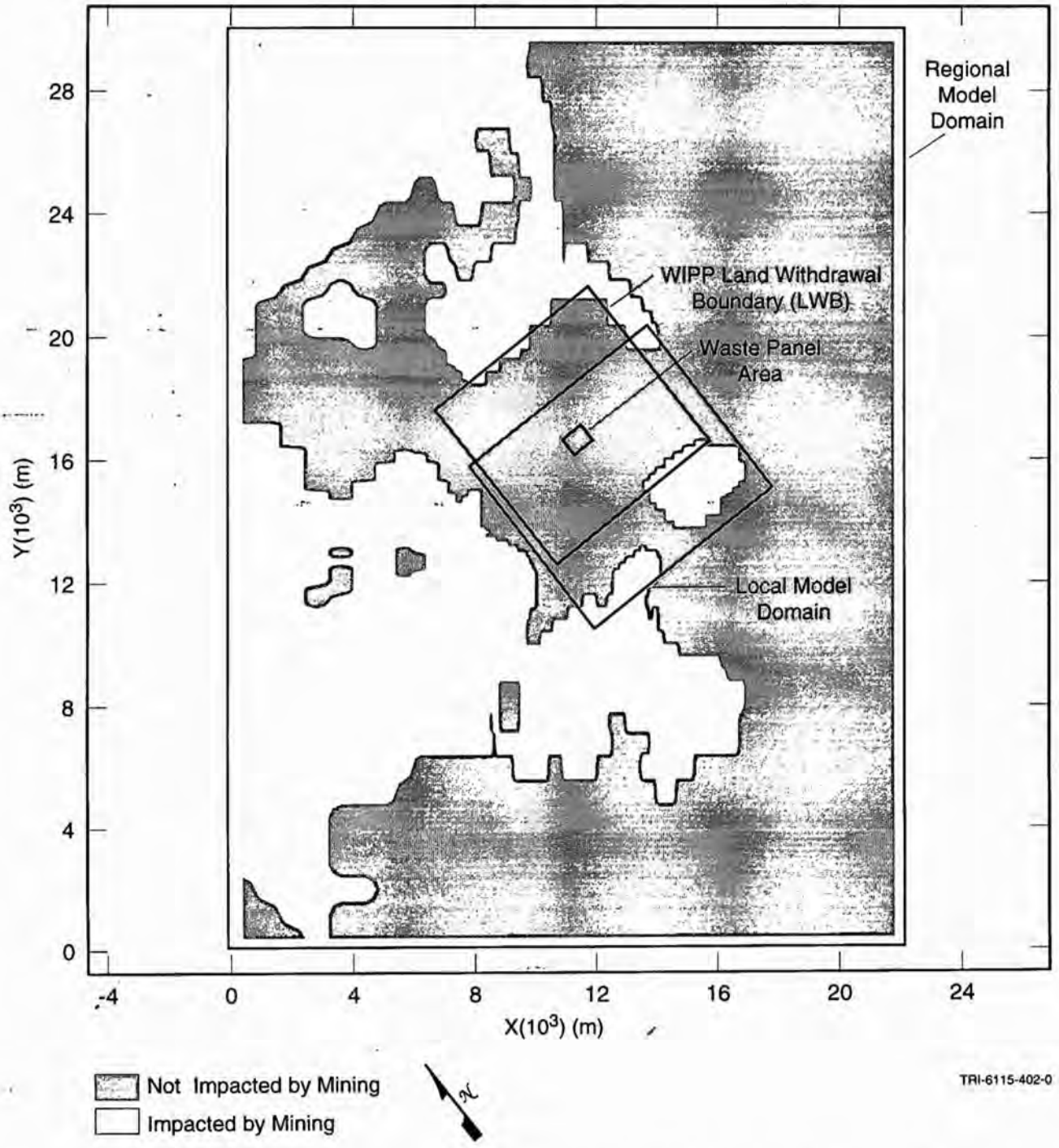

Figure 2.7 .--Extent of Impacted Area in the Culebra from Mining in the McNutt for Undisturbed Performance

Information Only

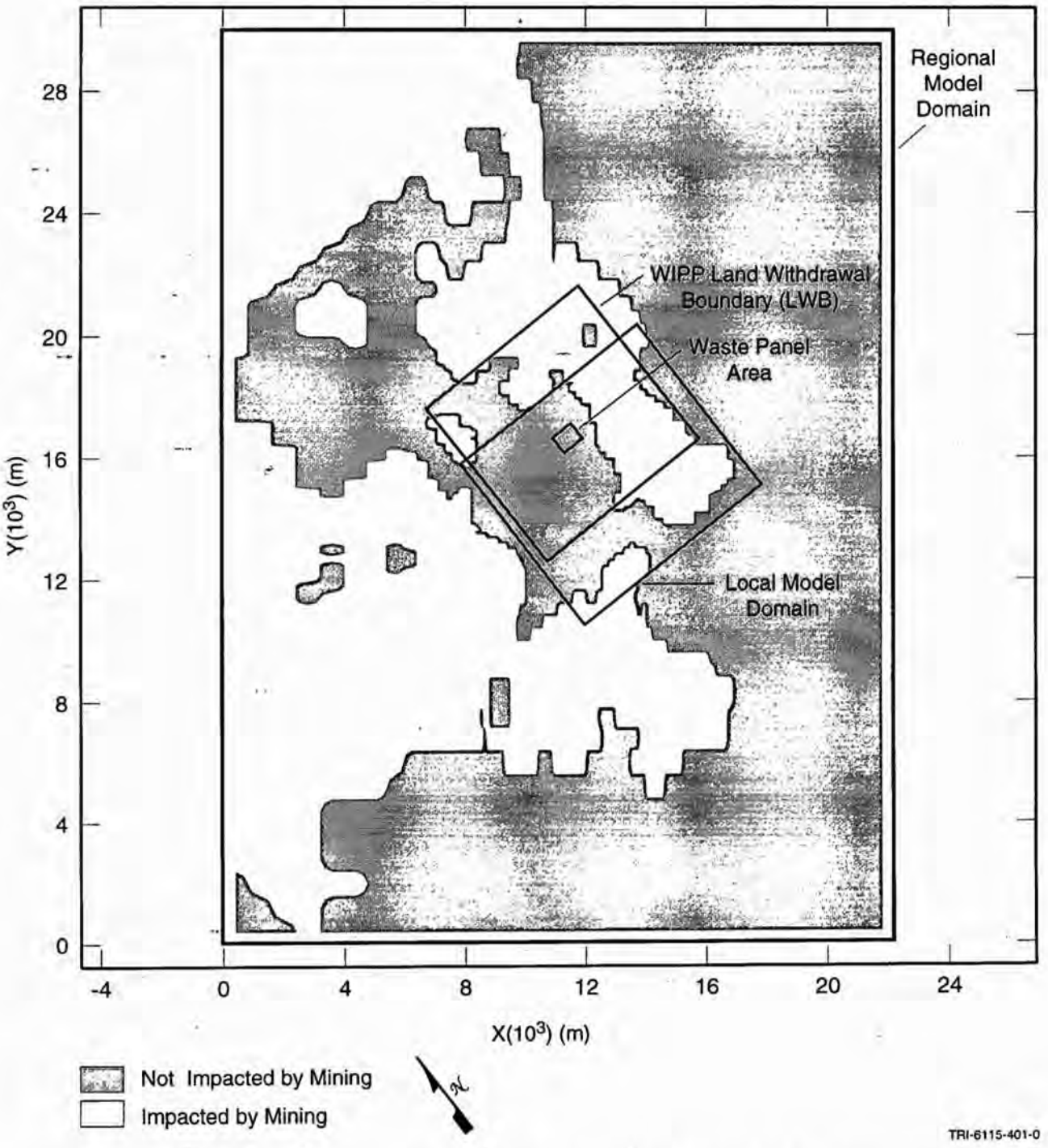

Figure 2.8. Extent of Impacted Area in the Culebra for Disturbed Performance if Mining Occurs in the Future within the Disposal System

Information Only

3.0 Personnel Assignments and Training Requirements

James Ramsey served as task leader and principal investigator for this work. Mike Wallace worked on the grid design, potash mining implementation, and other aspects of the calculations. Rebecca Blaine was in charge of scoping calculations and worked with the SCMS personnel to implement the analysis plan. All necessary input files and input streams required to perform the analysis were provided by Rebecca. Marsh Lavenue and others identified by Ruskauff (1996) were responsible for producing the transmissivity fields.

Additional contributions were made by Christine Stockman (parameter dependence on oxidation state), and Lanny Smith (LHS sampling).

These personnel were trained in the QA procedures listed in the following Section.

4.0 QA Requirements

The following SNL WIPP QA procedures were followed during this analysis:

QAP 6-3	Conducting and Documenting Reviews of Documents
QAP 9-1	Quality Assurance Requirements for Conducting Analyses
QAP 9-2	QA Requirements for Selection and Documentation of Parameter Values
QAP 9-5	Conducting and Documenting Routine Calculations
QAP 17-1	WIPP Quality Assurance Records Source Requirements
QAP 19-1	WIPP Computer Software Requirements

5.0 Technical Approach

Figures 5.1 and 5.2 consist of flow chart diagrams showing the flow of data and sequence of codes used in the Culebra flow and transport modeling. Tables 5.1 and 5.2 provide additional information about the codes and list the names of the specific input and output files used in the analysis. Table 5.1 list the steps performed in the groundwater flow calculations, and Table 5.2 list the steps of the transport calculations. Each code, its input files, primary output files, and the general purpose for running the code are given in the order of execution.

All input/output files and numerical codes are controlled in the CMS. Primary input files (files necessary to reproduce the calculations) are stored in CMS, and can be obtained using the CMS fetch utility. The primary input files are identified in Tables 5.1 and 5.2 with an * next to the input file name. These files are provided in their order of execution in Appendix E. File names ending in .cdb, .bin, .trn, and .vel, are binary output files and therefore, not included in Appendix E. Most output files have been deleted for disk space management purposes. To obtain such a file one must re-run the calculations up to the point the file is generated. A discussion of the calculation scripting and other information necessary to re-run all or a portion of the analysis is included in Williamson (1996).

Information Only

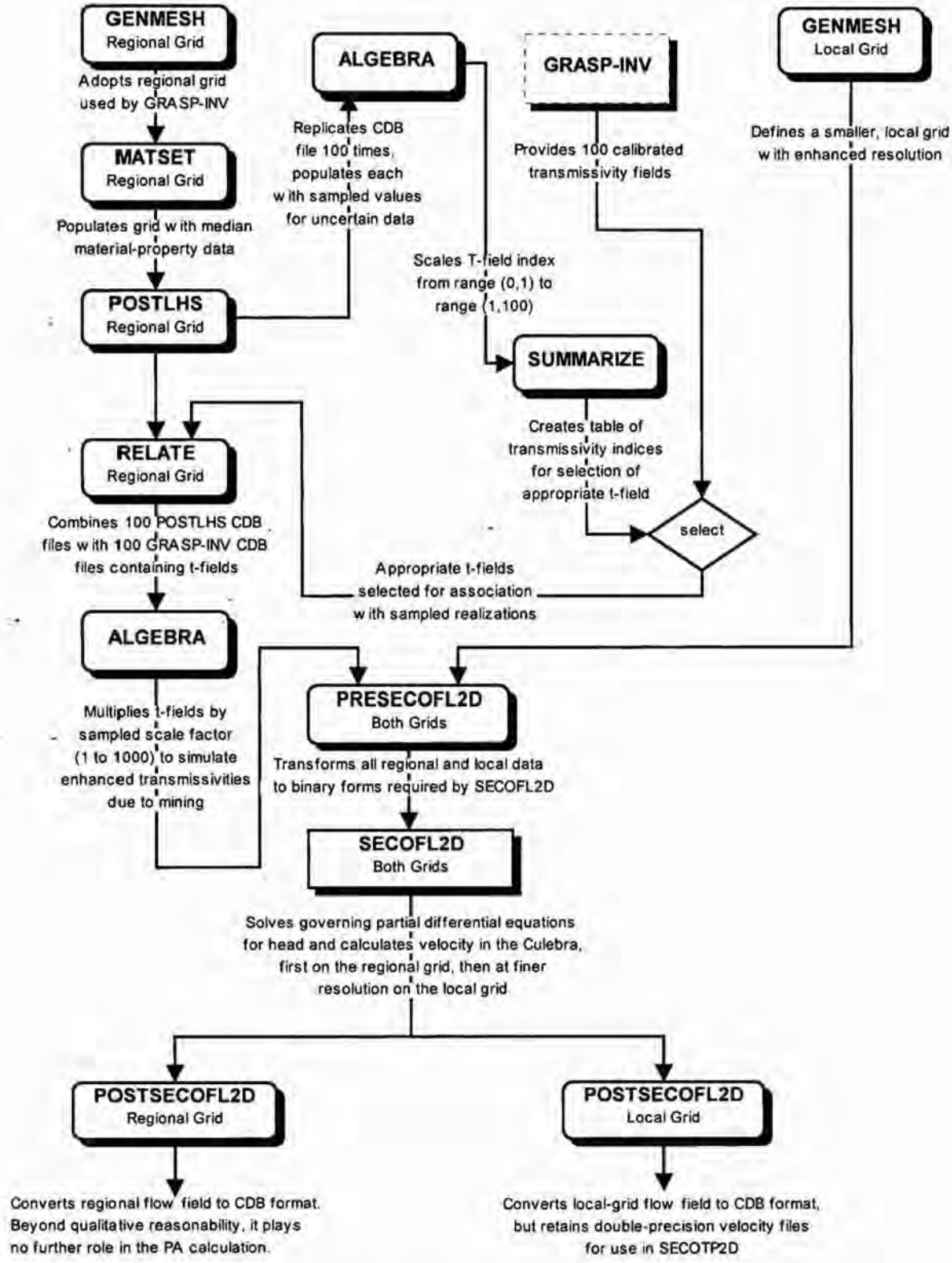

Figure 5.1. Flow Chart of the Culebra Groundwater Flow Calculations

Information Only

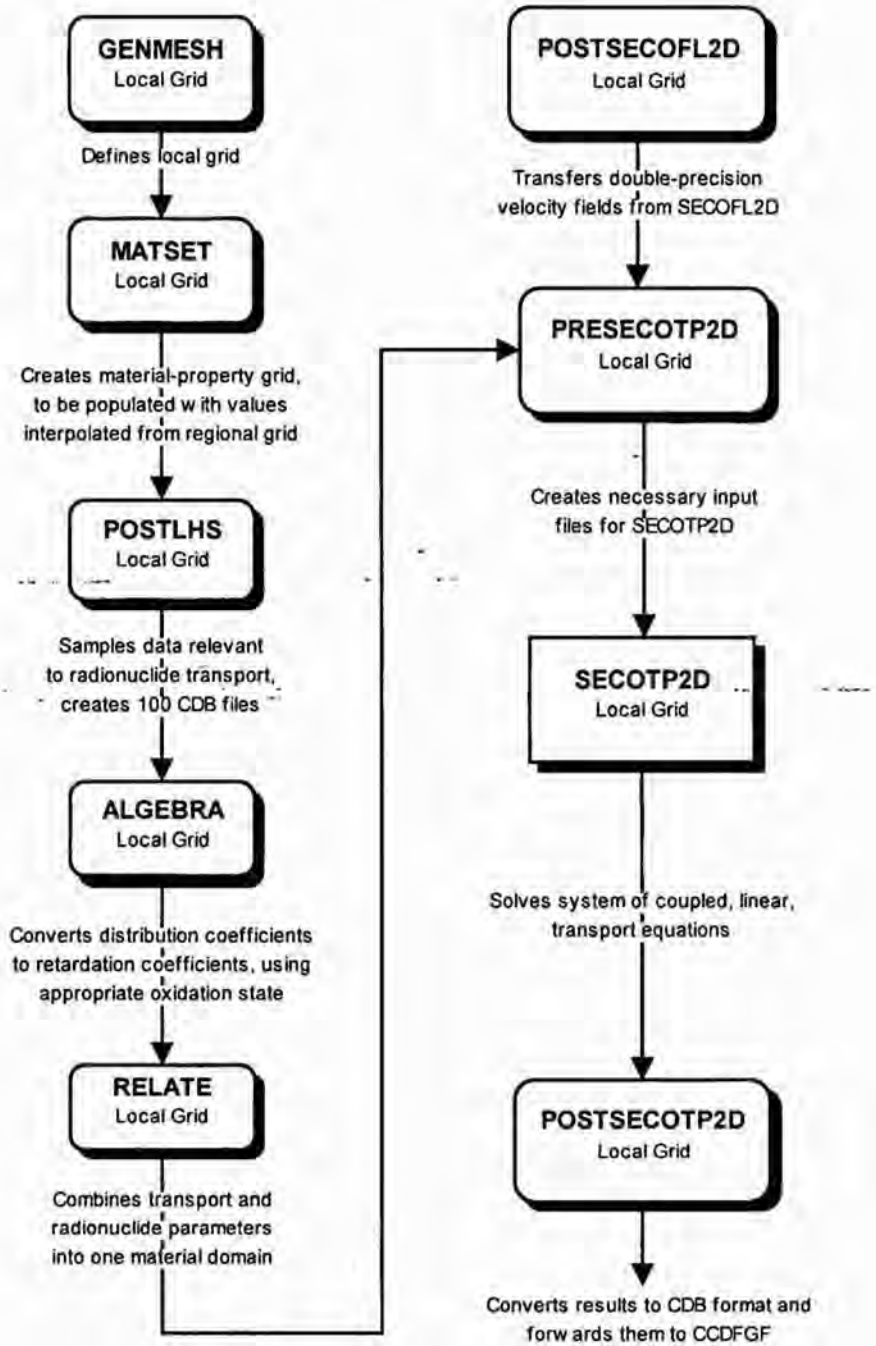

Note: Modeling codes are rectangular; utility codes are rounded.

Figure 5.2. Flow Chart of the Culebra Groundwater Transport Calculations

Information Only

Table 5.1 - Groundwater Flow Analysis

Code Name	Input Files	Purpose	Primary Output Files
GENMESH	gm_sf2d_cca_region.inp * 	Creates the regional groundwater flow mesh.	gm_sf2d_cca_region.cdb
GENMESH	gm_sf2d_cca_local.inp * 	Creates the local groundwater flow mesh.	gm_sf2d_cca_local.cdb
MATSET	ms_sf2d_cca.inp * gm_sf2d_cca_region.cdb	Sets material regions and extracts constant parameters from the secondary database.	ms_sf2d_cca_region.cdb
PRELHS	lhs1_sf2d_cca_Rx.inp *	Creates an input file in the format expected by LHS.	lhs1_sf2d_cca_trn_Rx.out
LHS	lhs1_sf2d_cca_trn_Rx.out	Performs the LHS sampling	lhs2_sf2d_cca_trn_Rx.out
POSTLHS	lhs2_sf2d_cca_trn_Rx.out ms_sf2d_cca_region.cdb lhs3_sf2d_cca.inp	Distributes LHS sampled values to individual computation data bases, CDB's.	lhs3_sf2d_cca_Rx_Vzzz.cdb
ALGEBRA	alg_sf2d_cca_region.inp * lhs3_sf2d_cca_Rx_Vzzz.cdb	Converts the transmissivity index from a real number from 0 to 1 to an integer from 1 to 100.	alg_sf2d_cca_Rx_Vzzz_region.cdb
SUMMARIZE	sum_sf2d_cca_Rx.inp * alg_sf2d_cca_Rx_Vzzz_region.cdb	Generates an ascii file of run number versus transmissivity index. This file is used in the relate script to match a specific T-field with each set of sampled parameters.	sum_sf2d_cca_Rx_transidx.tbl
RELATE	rel_sf2d_cca.inp * gri_cca_Rvvv.cdb alg_sf2d_cca_Rx_Vzzz_region.cdb	When the LHS sampling is performed, each set of sampled parameters are assigned to a single transmissivity field. RELATE copies the sampled values from the LHS output CDB's to the appropiate T-field determined by the transmissivity index.	rel_sf2d_cca_Rx_Vzzz_region.cdb
ALGEBRA	alg_sf2d_cca_fm.inp * alg_sf2d_cca_pm.inp * rel_sf2d_cca_Rx_Vzzz_region.cdb	Computes a hydraulic conductivity based on the effective thickness, then multiplies by the potash mining multiplier in regions predetermined to be mined. This and the following codes are run once for full mining and once for partial mining.	alg_sf2d_cca_Rx_Vzzz_M.cdb
PRESECOFL2D	sf2d1_cca.inp * alg_sf2d_cca_Rx_Vzzz_M.cdb gm_sf2d_cca_local.cdb	Configures the flow simulation, sets boundary conditions, assigns parameters, and defines the relative position of the local origin to the regional origin.	sf2d2_cca_Rx_Vzzz_M.inp sf2d2_cca_region_Rx_Vzzz_M.prp sf2d2_cca_local_Rx_Vzzz_M.prp
SECOFL2D	sf2d2_cca_Rx_Vzzz_M.inp sf2d2_cca_region_Rx_Vzzz_M.prp sf2d2_cca_local_Rx_Vzzz_M.prp	Performs flow simulations. First, the solution to the regional flow field is computed, then the solution to the local flow field is computed. The two step process is performed automatically.	sf2d3_cca_local_Rx_Vzzz_M.bin
POSTSECOFL2D	gm_sf2d_cca_local.cdb sf2d3_cca_local_Rx_Vzzz_M.bin sf2d2_cca_local_Rx_Vzzz_M.prp	Copies SECOFL2D local output to a CDB format, and outputs velocity field to be used in the transport simulations	sf2d3_cca_local_Rx_Vzzz_M.cdb sf2d3_cca_veloc_Rx_Vzzz_M.trn
POSTSECOFL2D	alg_sf2d_cca_Rx_Vzzz_M.cdb sf2d3_cca_region_Rx_Vzzz_M.bin sf2d2_cca_region_Rx_Vzzz_M.prp	Copies SECOFL2D regional output to a CDB format.	sf2d3_cca_region_Rx_Vzzz_M.cdb

Information Only

Table 5.2 - Groundwater Transport Analysis

Code Name	Input Files	Purpose	Primary Output Files
GENMESH	gm_st2d_cca.inp *	Creates the local groundwater flow mesh.	gm_st2d_cca.cdb
MATSET	ms_st2d_cca.inp * gm_st2d_cca.cdb	Sets material regions and extracts constant parameters from the secondary database.	ms_st2d_cca.cdb
PRELHS	lhs1_st2d_cca_Rx.inp *	Creates an input file in the format expected by LHS.	lhs1_st2d_cca_trn_Rx.out
LHS	lhs1_st2d_cca_trn_Rx.out	Performs the LHS sampling	lhs2_st2d_cca_trn_Rx.out
POSTLHS	lhs2_st2d_cca_trn_Rx.out ms_st2d_cca.cdb lhs3_st2d_cca.inp	Distributes LHS sampled values to individual computation data bases, CDB's.	lhs3_st2d_cca_Rx_Vzzz.cdb
ALGEBRA	alg_st2d_cca.inp * lhs3_st2d_cca_Rx_Vzzz.cdb	Computes decay constants, specific activity, and retardation coefficients. Parameter dependence on oxidation state is also accounted for here. The desired free water molecular diffusion and the matrix distribution coefficients are selected based on the value of OXSTAT.	alg_st2d_cca_Rx_Vzzz.cdb
RELATE	rel_st2d_cca.inp * alg_st2d_cca_Rx_Vzzz.cdb gm_st2d_cca.cdb	It was necessary in the previous steps to create a number of additional material blocks to accomodate parameter dependence on oxidation state. This step is performed to consolidate all parameters into a single material block prior to running PRESECOTP2D.	rel_st2d_cca_Rx_Vzzz.cdb
PRESECOTP2D	st2d1_cca.inp * rel_st2d_cca_Rx_Vzzz.cdb sf2d3_cca_veloc_Rx_Vzzz_M.trn	Configures the transport simulation, sets boundary conditions, and assigns parameters. This and the following codes are run once for full mining and once for partial mining.	st2d2_cca_Rx_Vzzz_M.inp st2d1_cca_Rx_Vzzz_M.prp st2d1_cca_Rx_Vzzz_M.vel
SECOTP2D	st2d2_cca_Rx_Vzzz_M.inp st2d1_cca_Rx_Vzzz_M.prp st2d1_cca_Rx_Vzzz_M.vel	Performs transport simulation.	st2d3_cca_Rx_Vzzz_M.bin
POSTSECOTP2D	rel_sf2d_cca_Rx_Vzzz.cdb st2d3_cca_Rx_Vzzz_M.bin	Copies SECOTP2D output to a CDB format.	st2d3_cca_Rx_Vzzz_M.cdb

Information Only

6.0 Conclusions

The release of radioisotopes from an intrusion borehole to the accessible environment in 10,000 years via transport through the Culebra is highly improbable. In only two of the 600 transport simulations performed were non-zero integrated discharge results obtained. This conclusion is substantially different than those of previous performance assessments of the WIPP. The primary reason for the difference in results is thought to be the use of larger matrix distribution coefficients (k_d) in this analysis.

7.0 Results

The results of a performance assessment of this magnitude are often difficult to analyze and even harder to present. In an attempt to address the general behavior of the calculations, a select few of the 600 flow and transport calculations are discussed in detail. The runs presented provide the reader with a basic understanding of the Culebra flow and transport results. There are however, many simulations that do not exhibit the "general behavior" discussed. Abnormal results are presented only when the abnormality has implications on compliance. It is beyond the scope of this report to conduct a detailed analysis of each simulation. Calculation results are available in CMS should questions arise about a particular run.

In addition to providing tables and diagrams of the results, this section includes a preliminary investigation into the spatial and temporal convergence of the solution. It is stated here and again in Section 7.3 that this is a preliminary study, provided mainly to support the conclusion given above. The findings presented in Section 7.3 often give rise to more questions than answers. Consequently, this Section does not contain a definitive position regarding solution convergence, nor was it intended to do so.

7.1 Culebra Flow Results

Results of the Culebra flow calculations are analyzed using a particle tracking simulator, called TRACKER. TRACKER computes the flow path and travel time of a non-reactive non-sorbing particle released into the velocity field computed by SECOTP2D. The computed flow path shows the direction of flow of a particle from the point of release to the land withdrawal boundary. The travel time provides a quantitative measure of the magnitude of the velocity field along this flow path.

The travel times reported here are termed "relative travel times" because they were computed using a porosity equal to one. They are reported in this manner to emphasis the fact that travel times cannot be used to predict isotope transport times. This is because travel times are computed assuming an equivalent porous medium (single porosity). As discussed in Appendix A, a dual porosity formulation is a more accurate representation of flow and transport processes in the Culebra. Because particle travel times are based on the assumption of an equivalent

Information Only

porous media, they do not incorporate the effects of rapid flow through the advective continuum, diffusion into the matrix, sorption, or dispersion. Consequently, it does not matter what value of porosity is chosen to compute a travel time, the resulting value simply does not quantify isotope transport in the Culebra. Actual travel times could be larger or smaller than those reported here.

On the other hand, travel times (relative or not) do provide a means of comparing hydraulic conductivity fields in a quantitative manner. Such a comparison is presented in Figure 7.1, where the relative travel times of a particle released at the center of the waste panel area to the land withdrawal boundary are plotted for the Replicate 1, full mining, partial mining, and no mining cases. The no mining hydraulic conductivity fields (K-fields), from which the no mining travel times are derived, consist of the K-fields computed by GRASP-INV modified to represent the effective thickness rather than the total thickness of the Culebra. These flow calculations are not part of the CCA analysis, and are presented here only to examine the effect of mining on groundwater flow. The travel times presented in Figure 7.1 have been sorted according to the results of the no mining simulations. The data are plotted such that each vertical field contains the relative travel time of the original and associated K-fields altered by mining.

In the no mining flow fields, there is roughly an order of magnitude difference in the computed travel times. This variation is representative of the uncertainty in the Culebra transmissivity field given the Project's current knowledge of the site. When the effects of mining are incorporated into the flow field, the range in predicted travel times are substantially greater. For partial mining the range is roughly two orders of magnitude, and for full mining the range is about two and half orders magnitude. Clearly, a large degree of the uncertainty associated with the flow fields of the CCA can be attributed to the incorporation of potash mining in the analysis.

The impact of mining on the Culebra flow field generally resulted in an increase in travel time. In 70% of the comparisons presented in Figure 7.1, the shortest travel times were obtained using the non-mined K-fields. This result is somewhat counter intuitive because the hydraulic conductivity over a large portion of the problem domain is always greater for the mined K-fields than it is in the corresponding non-mined K-field. All other things being equal (i.e.. boundary conditions), one would assume that an increase in hydraulic conductivity would lead to an increase in discharge, and therefore, a reduction in travel time. This was generally not the case however, due to an alteration in the direction of flow within the land withdrawal boundary.

Changes in the hydraulic conductivity over such a wide area, frequently produced a refraction in the normal groundwater flow paths. The altered flow paths were generally longer and much slower than those in the non-mined simulations. Groundwater flow results computed from the non-mined K-fields show the direction of flow in the Culebra to be from the north to the south or southeast. Flow paths from the waste panel area to the land withdrawal boundary generally pass through a highly transmissive region that has become known as the "high-T zone". The high-T zone is located south and slightly to the east of the waste panel area. After applying the effects of mining to the flow domain, particle tracking results show a more westward route, no longer passing through the high-T zone.

Information Only

In the southwestern portions of the land withdrawal boundary, the hydraulic conductivities are much lower than they are the high-T zone. Mining is presumed to not occur in this region so there is no increase in hydraulic conductivity as a consequence of mining. Due to relatively low hydraulic conductivities and head gradients, fluid velocities also tend to be low in the southwestern portion of the land withdrawal boundary. Consequently, when the direction of flow is diverted only slightly to the west from its original flow path, the effect on travel time can be dramatic.

To illustrate this behavior, results of the flow calculations performed for Run #40 of Replicate 1 are presented below. This run has the eighth fastest non-mined travel time and is considered to possess a more or less typical response to the effects of mining. The K-field used in this run was selected during the LHS sampling (see Appendix D). For Run #40 of Replicate 1, the K-field chosen was vector #53, which is shown in Figure 7.2. The location of the high-T zone is identified on this Figure, as are the locations of the land withdrawal boundary and waste panel area. The partial and full mining K-fields were derived from vector #53 using the mining location maps given in Figures 2.7 and 2.8. The resultant partial and full mining K-fields are shown in Figures 7.3, and 7.4, respectively. The sampled hydraulic conductivity multiplier for this run was 271.4.

The regional groundwater flow solution for each of the three cases is presented in Figures 7.5, through 7.7, in the form of hydraulic head contour plots. In the case of no mining, Figure 7.5, the contours depict a relatively steep gradient just north of the waste panel area which flattens out to the south and southeast. Based on the contour lines, the direction of flow inside the land withdrawal boundary is predominately to the southeast. In the case of partial mining, Figure 7.6, the additional spread between the C and D contour intervals demonstrates the head gradients south of the waste panel area are somewhat reduced. More importantly the contour lines show that the direction of flow inside the land withdrawal boundary has shifted from a southeastern flow pattern to more of a southwestern flow pattern. Finally, the full mining solution, Figure 7.7, shows the direction of flow has shifted just about 90 degrees to the west from the non-mined solution inside the land withdrawal boundary.

For the same three cases, flow paths of thirteen particles released along a horizontal east/west line through the center of the waste panel area are shown in Figures 7.8 through 7.10. In the no mining case, Figure 7.8, the direction of flow is south to southeast with all particles eventually ending up in the high-T zone where they are rapidly transported to the land withdrawal boundary.

Particle tracks of the partial mining flow field are similar to that of the non-mined flow field except for a slight bend to the southwest near the discharge boundary, Figure 7.9. If one overlays the partial mining particle tracks on top of the non-mined particle tracks it can be seen the partial mining flow paths are slightly west of the non-mined flow paths. This slight shift to the west combined with somewhat lower head gradients resulted in a much longer travel time to the land withdrawal boundary (position 8 in Figure 7.1).

Information Only

When the effects of full mining are imposed on the original K-field, the direction of flow south of the waste panel area was altered substantially, Figure 7.10. Particles initially flow in a south to southeastern direction but quickly turn to the southwest and ultimately due west. The travel path and travel time are consequently considerably larger than those of either the partially mined or non-mined cases.

This specific example is just one of many runs in which this type behavior is exhibited. As shown in Figure 7.1, the non-mined travel times are generally the smallest, and the fully mined travel times are generally the largest. Further evidence is given in Figures 7.11, 7.12, and 7.13. Here the travel path of a single particle released in the center of the waste disposal region is ploted for each run in replicate 1.

These results support the assumption made in Section 2.6 that the effects of mining are generally conservative with respect to isotope transport. This counter intuitive result is caused by a change the direction of flow in and around the waste panel area. It is important to point out that this finding is highly dependent on the location of the potash reserves. Should the mining maps depicted in Figures 2.7 and 2.8 be altered at some point, the assumption made in Section 2.6 may no longer be true.

Information Only

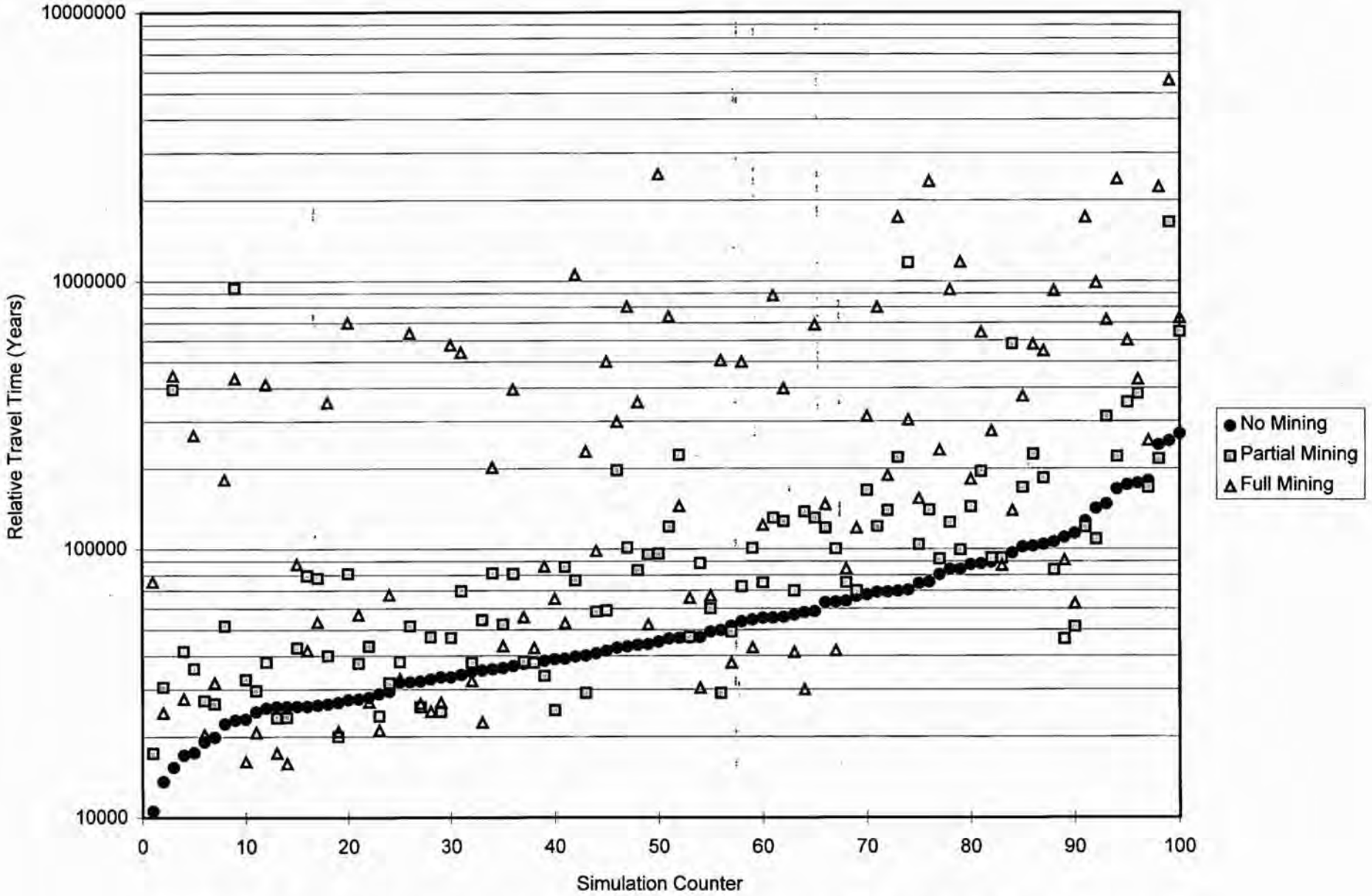

Figure 7.1. Relative Travel Times of the Replicate 1 Full, Partial, and Non-mined Flow Fields

Information Only

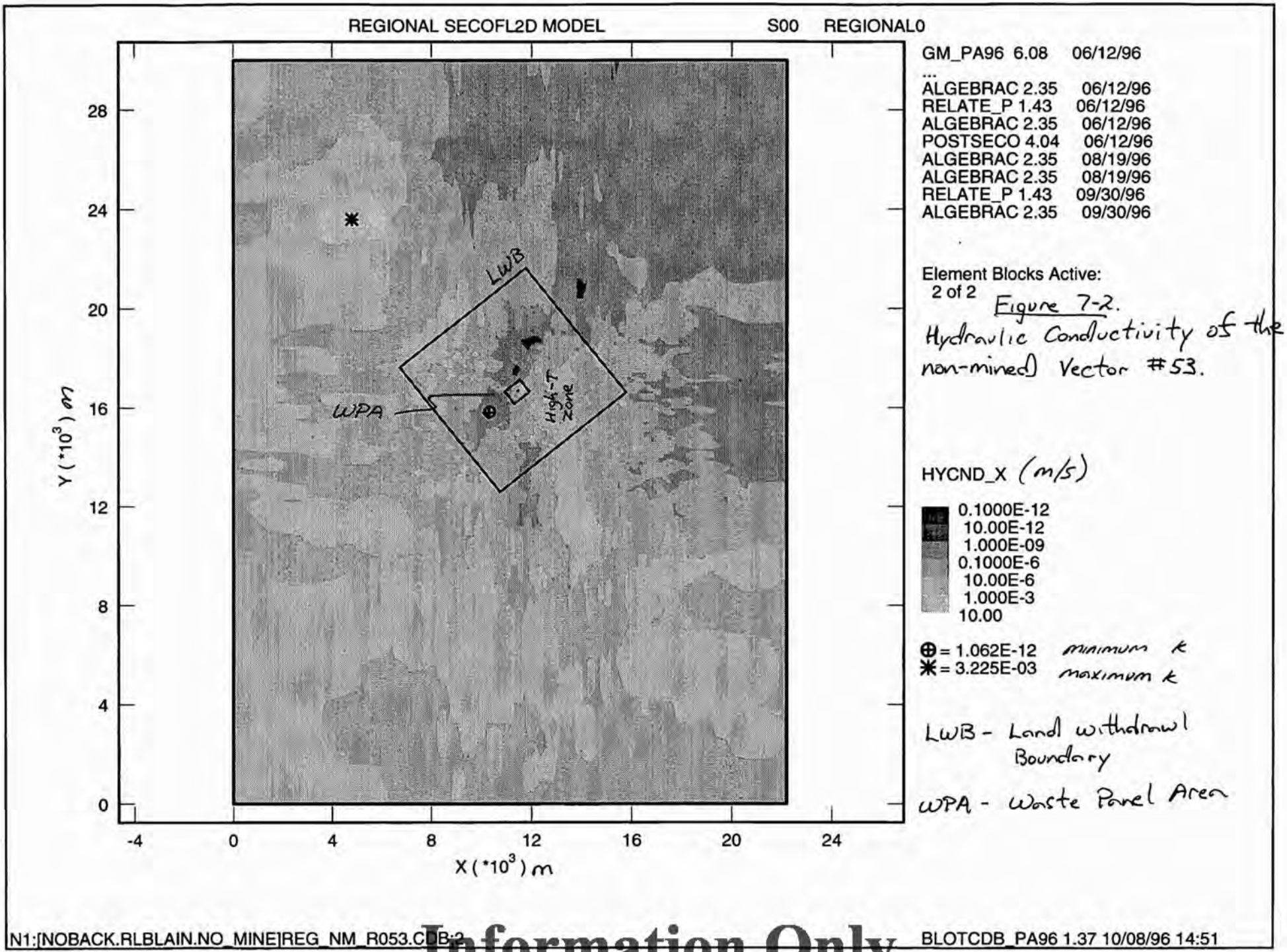

Figure 7-2. Hydraulic Conductivity of the non-mined Vector #53.

Information Only

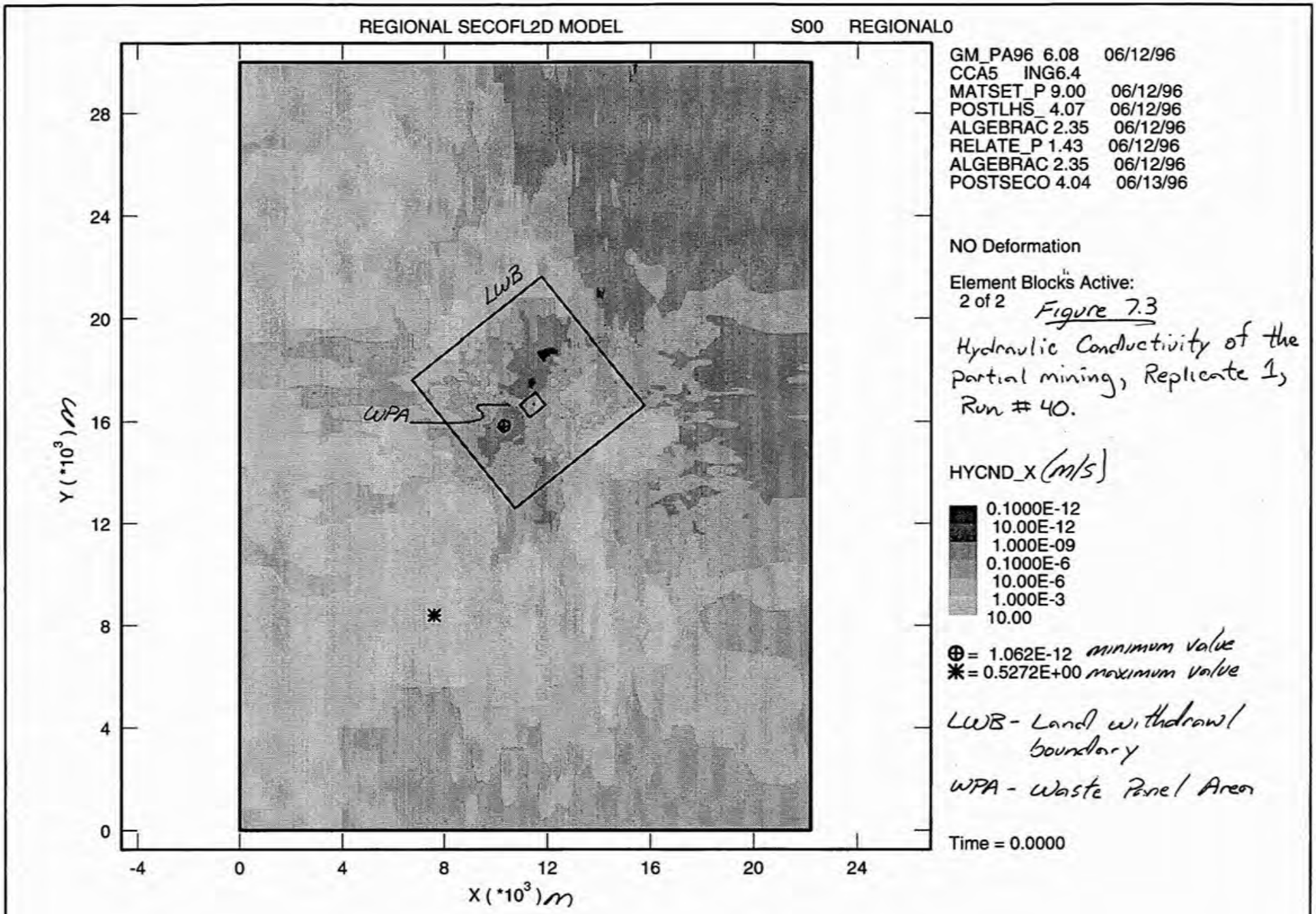

Figure 7.3
Hydraulic Conductivity of the partial mining, Replicate 1, Run # 40.

LWB - Land withdrawl boundary

WPA - Waste Panel / Area

Information Only

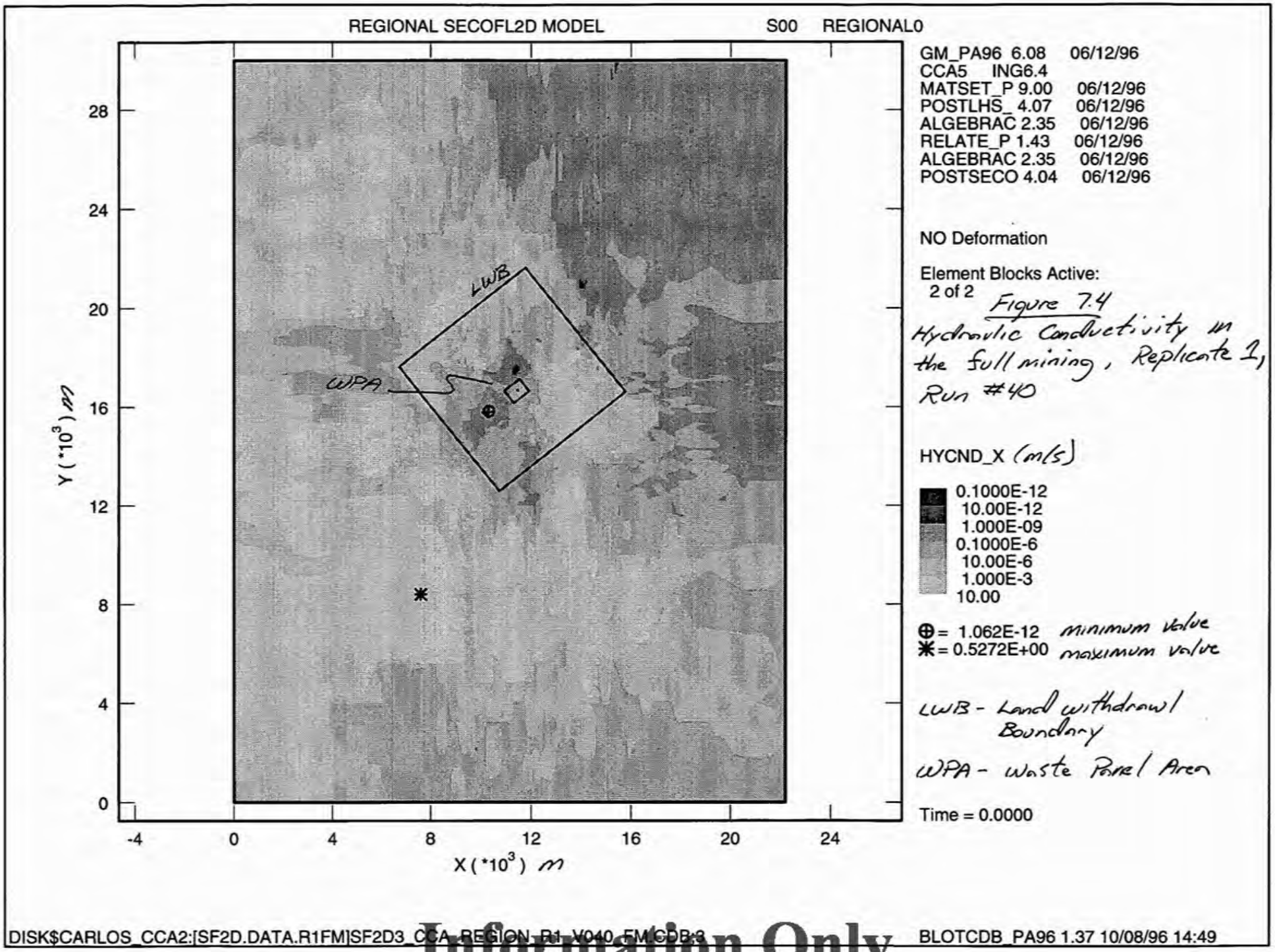

Figure 7.4
Hydraulic Conductivity in the full mining, Replicate 1, Run #40

Information Only

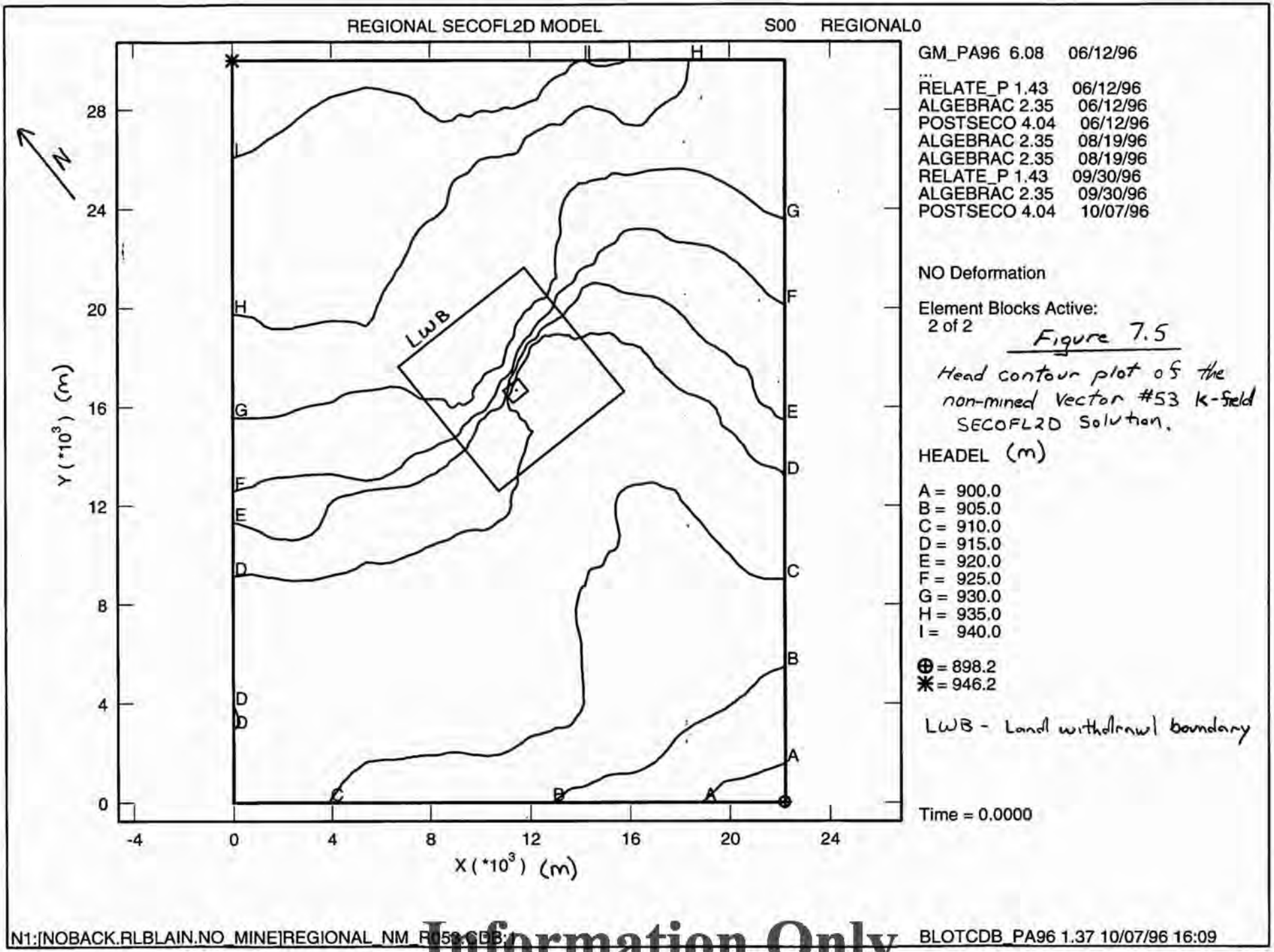

Figure 7.5

Head contour plot of the non-mined Vector #53 k-field SECOFL2D Solution.

LWB - Land withdrawl boundary

Information Only

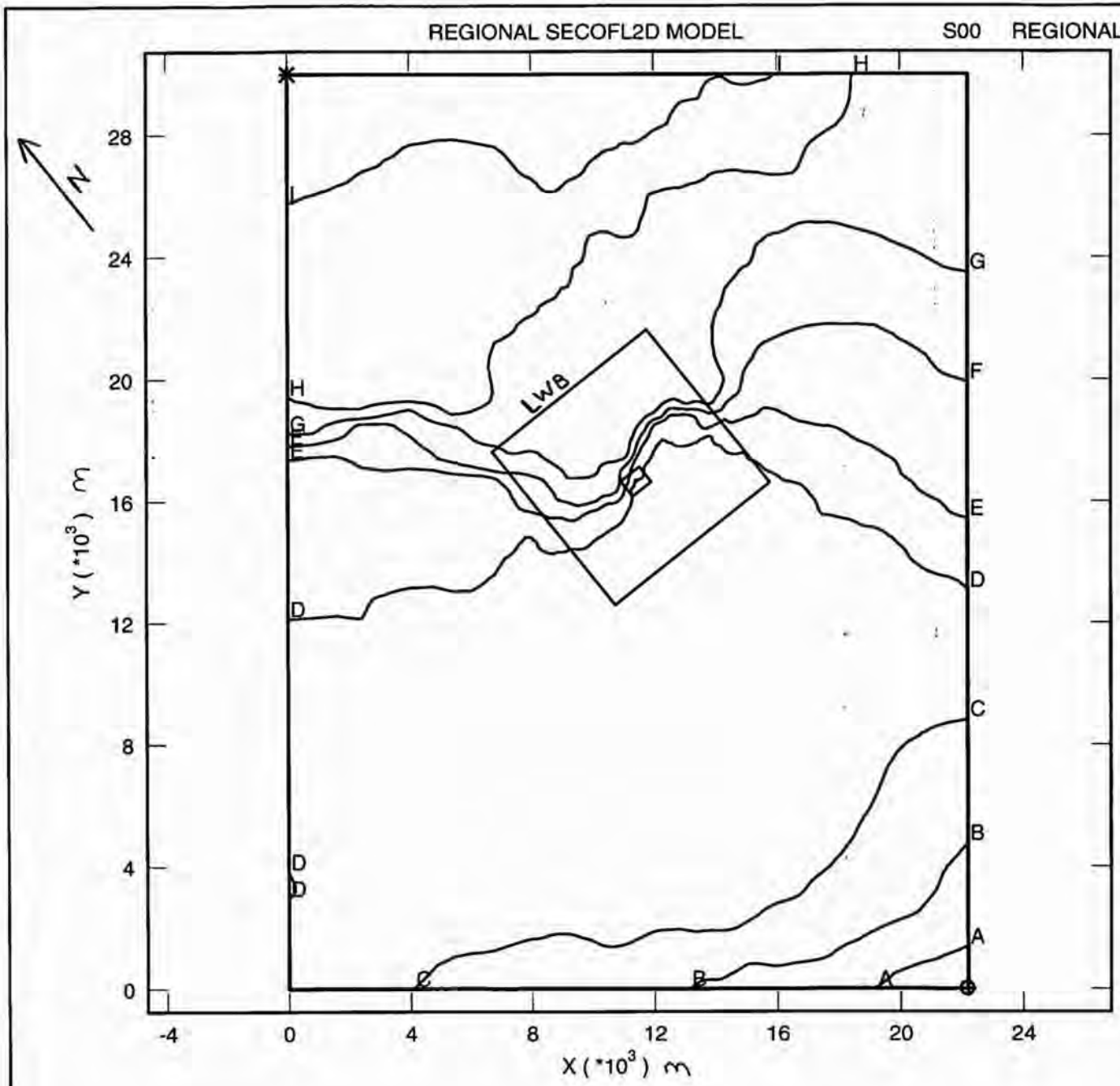

GM_PA96 6.08 06/12/96
CCA5 ING6.4
MATSET_P 9.00 06/12/96
POSTLHS_ 4.07 06/12/96
ALGEBRAC 2.35 06/12/96
RELATE_P 1.43 06/12/96
ALGEBRAC 2.35 06/12/96
POSTSECO 4.04 06/13/96

NO Deformation

Element Blocks Active:
2 of 2

Figure 7.6

Head contours of the regional Replicate 1, partial mining, Run #40 groundwater flow solution.

HEADEL (m)

A = 900.0
B = 905.0
C = 910.0
D = 915.0
E = 920.0
F = 925.0
G = 930.0
H = 935.0
I = 940.0

⊕ = 898.3
✳ = 946.2

LWB - Land withdrawl boundary

Time = 0.0000

DISK$CARLOS_CCA2:[SF2D.DATA.R1PM]SF2D3_CCA_REGION_R1_V040_PM.CDB;3

BLOTCDB_PA96 1.37 10/07/96 15:43

Information Only

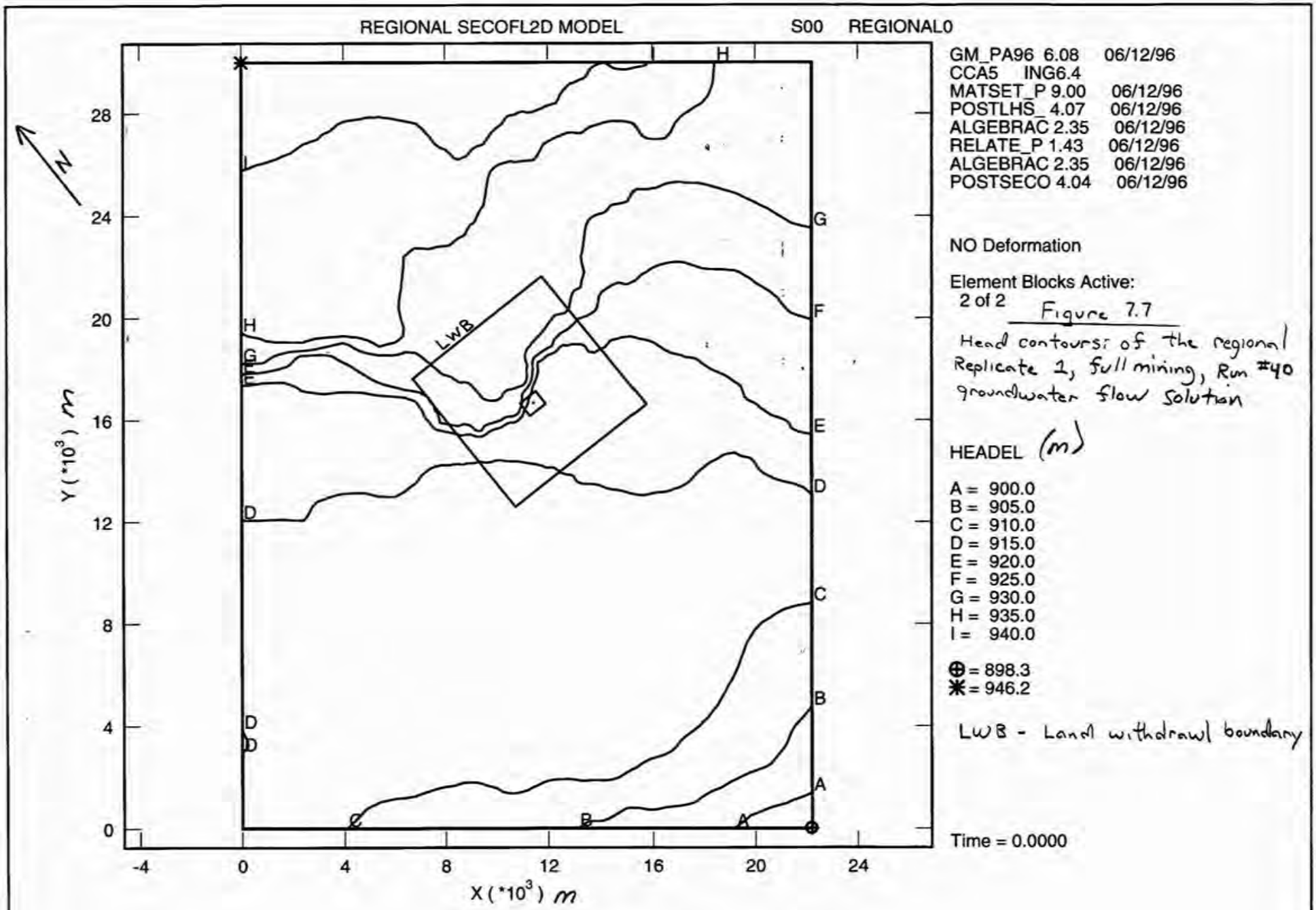

Figure 7.7
Head contours of the regional Replicate 1, full mining, Run #40 groundwater flow solution

Information Only

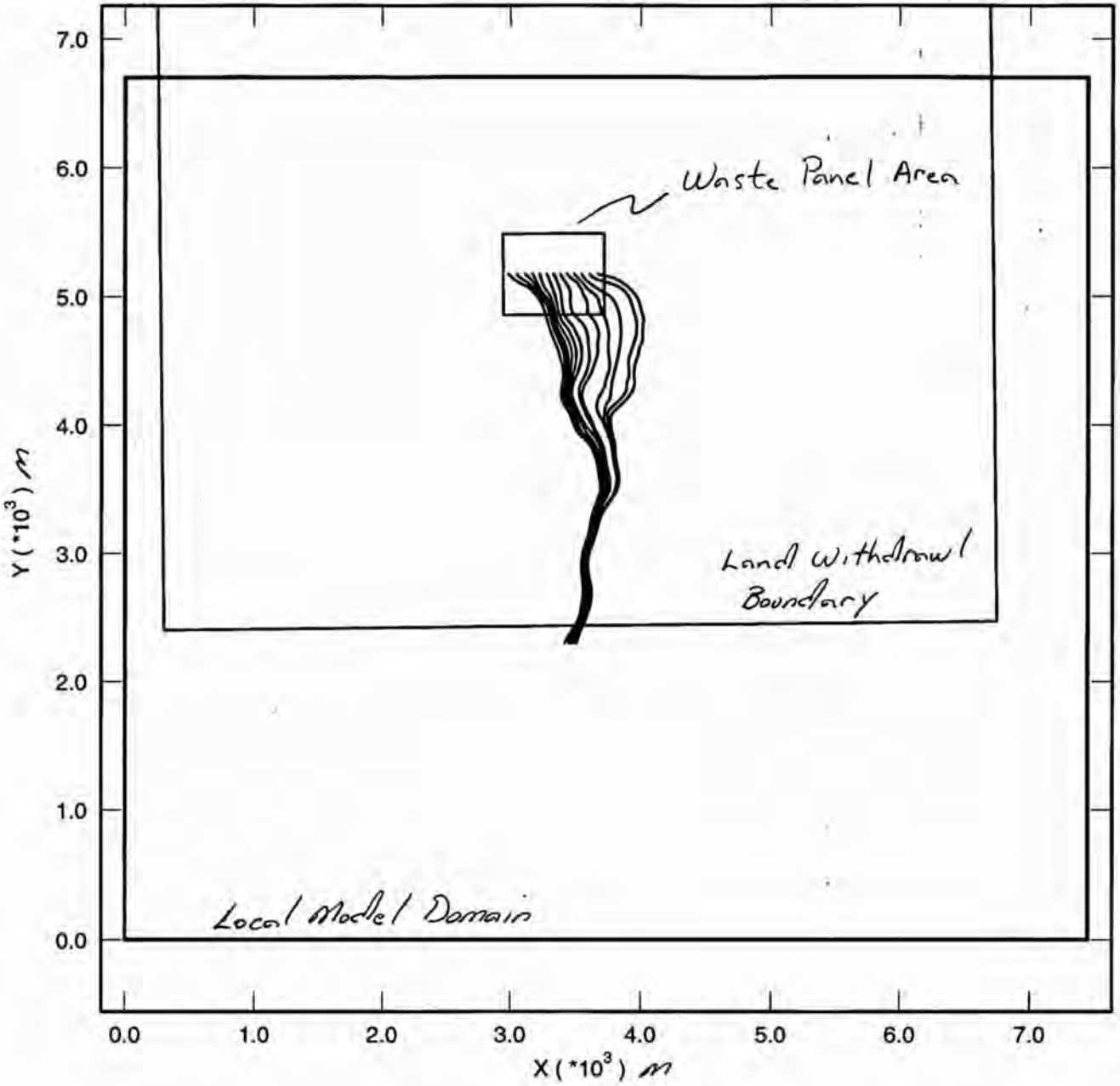

GM_PA96 6.08 06/12/96
POSTSECO 4.04 09/30/96
TRACKER C-5.01ZO 10/08/96

Element Blocks Active:
1 of 1

Figure 7.8
Particle Tracks of the non-mined k-field #53

X001 Y001
X002 Y002
X003 Y003
X004 Y004
X005 Y005
X006 Y006
X007 Y007
X008 Y008
X009 Y009
X010 Y010
X011 Y011
X012 Y012
X013 Y013

Times 0.0E+9
to 637.8E+9

N1:[NOBACK.RLBLAIN.NO_MINE]TRACK_NM_R053.CDB;1

BLOTCDB_PA96 1.37 10/09/96 08:15

Information Only

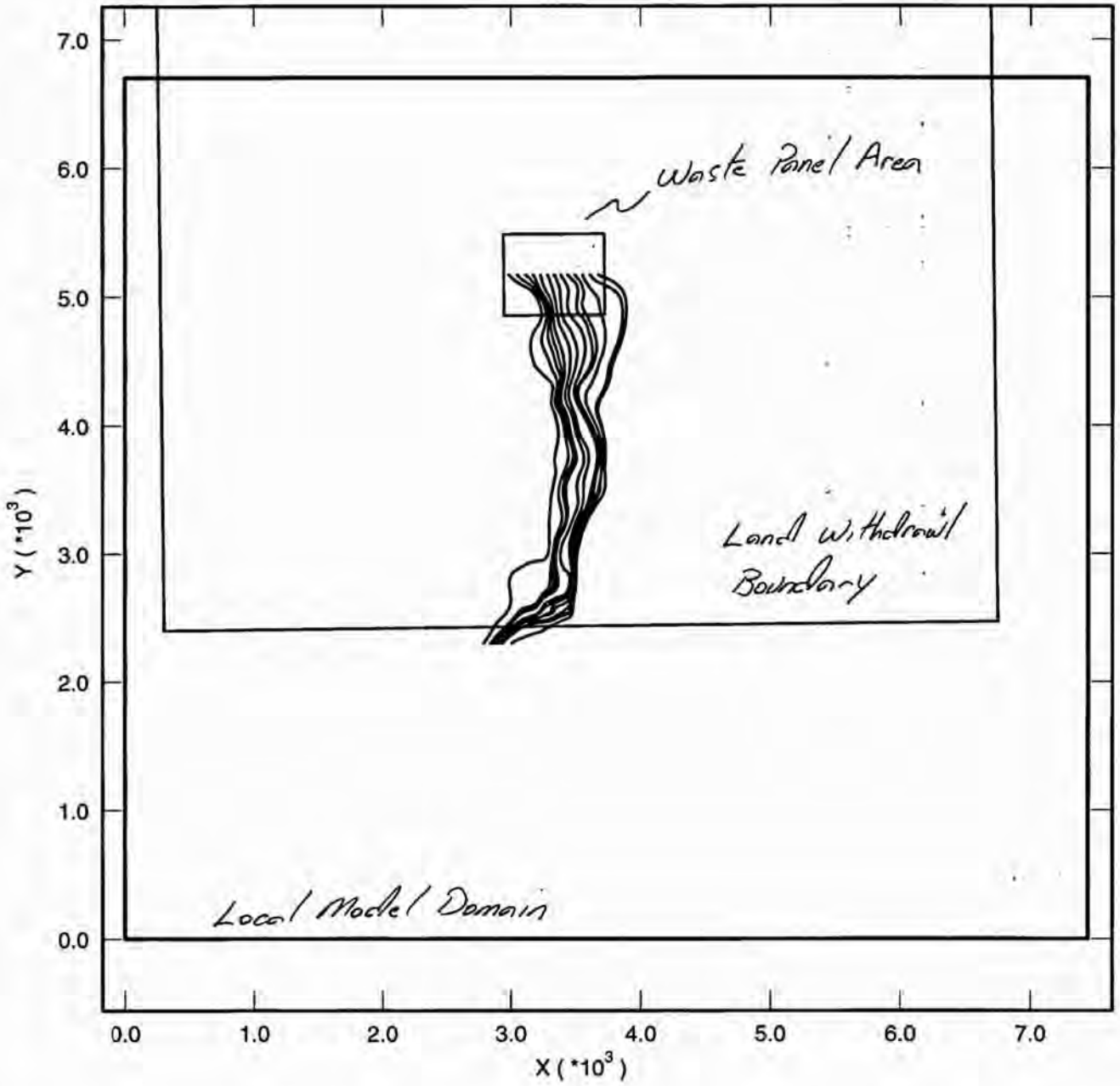

GM_PA96 6.08 06/12/96
POSTSECO 4.04 06/13/96
TRACKER 10/08/96

Element Blocks Active:
1 of 1

Figure 7.9
Particle Tracks of the Partial Mining Run #40 in Replicate 1.

X001 Y001
X002 Y002
X003 Y003
X004 Y004
X005 Y005
X006 Y006
X007 Y007
X008 Y008
X009 Y009
X010 Y010
X011 Y011
X012 Y012
X013 Y013

Times 0.0E+9
to 830.9E+9

N1:[NOBACK.RLBLAIN.TRACK]TRACK_R040_PM.CDB;1

BLOTCDB_PA96 1.37 10/09/96 08:15

Information Only

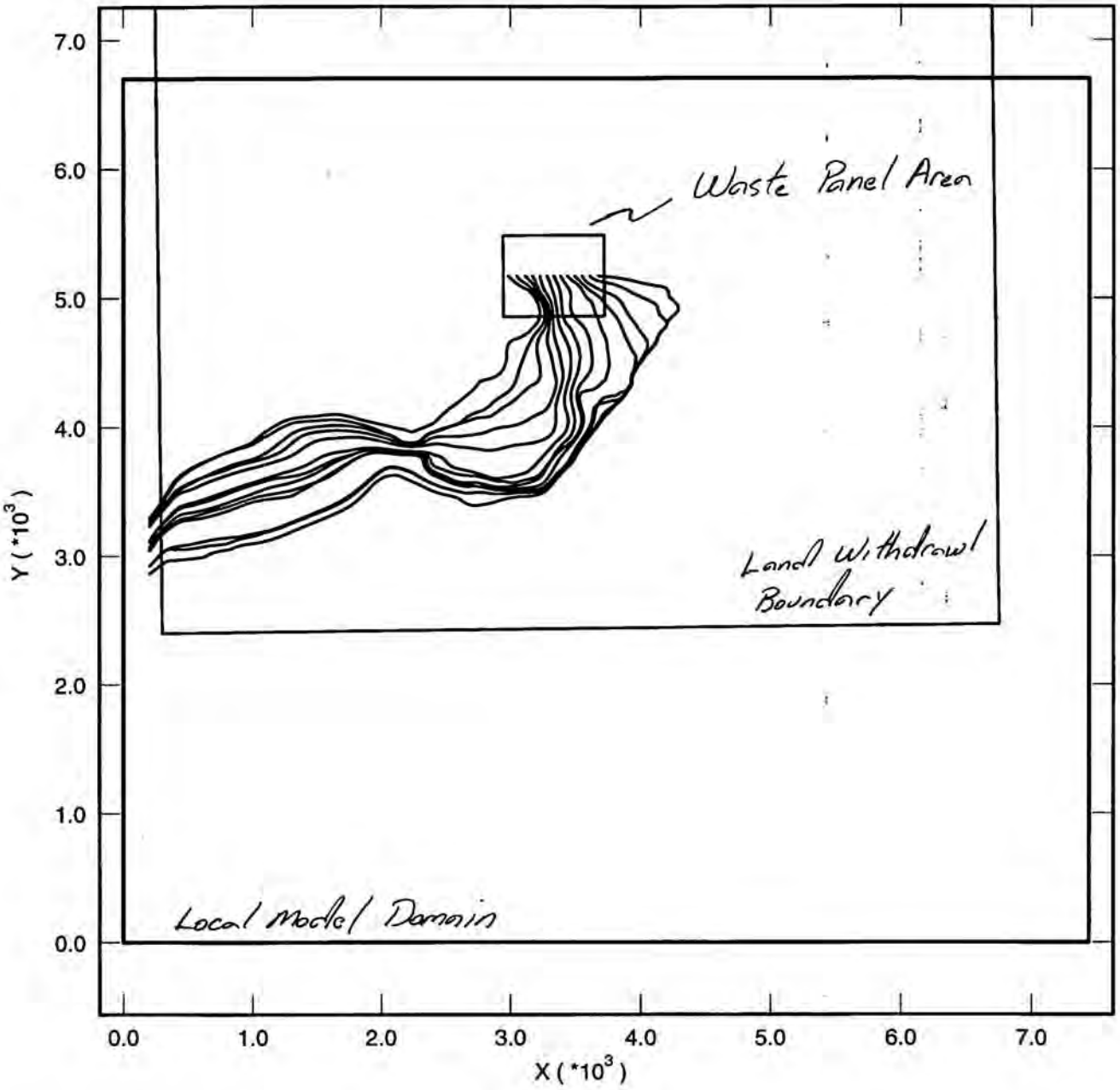

GM_PA96 6.08 06/12/96
POSTSECO 4.04 06/12/96
TRACKER 10/08/96

Element Blocks Active:
1 of 1

Figure 7.10
Particle Tracks of the Full Mining Run #40 in Replicate 1.

X001 Y001
X002 Y002
X003 Y003
X004 Y004
X005 Y005
X006 Y006
X007 Y007
X008 Y008
X009 Y009
X010 Y010
X011 Y011
X012 Y012
X013 Y013

Times 0.000E+12
to 2.233E+12

N1:[NOBACK.RLBLAIN.TRACK]TRACK_R040_FM.CDB;1

BLOTCDB_PA96 1.37 10/09/96 08:14

Information Only

Figure 7.11.

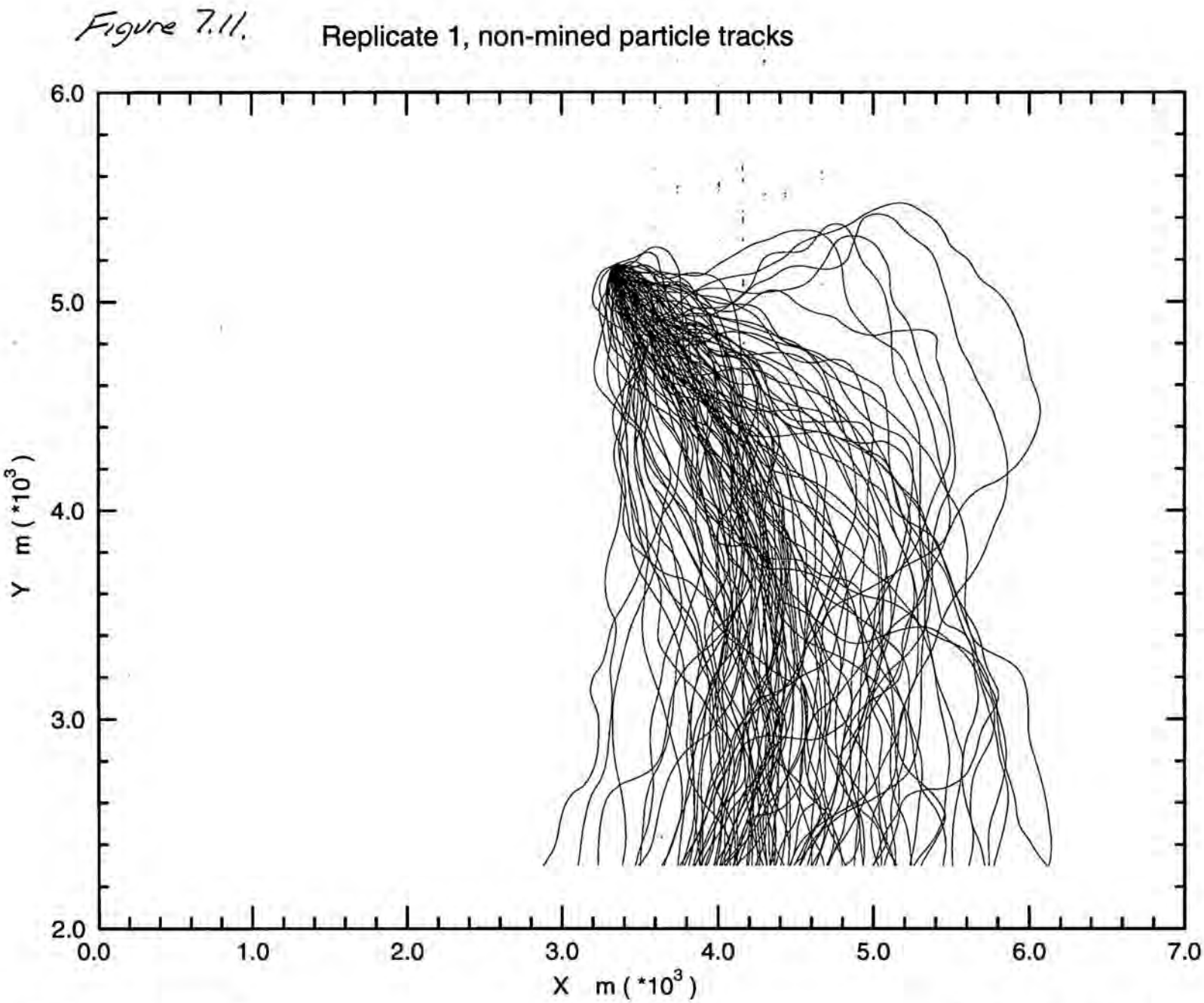

N1:[NOBACK.JLRAMSE.CCA.TRACKER]N_MINE.CMD;2

SPLAT_PA96_2 1.02 10/29/96 15:47:07

Information Only

Figure 7.12. Replicate 1, partial mining particle tracks

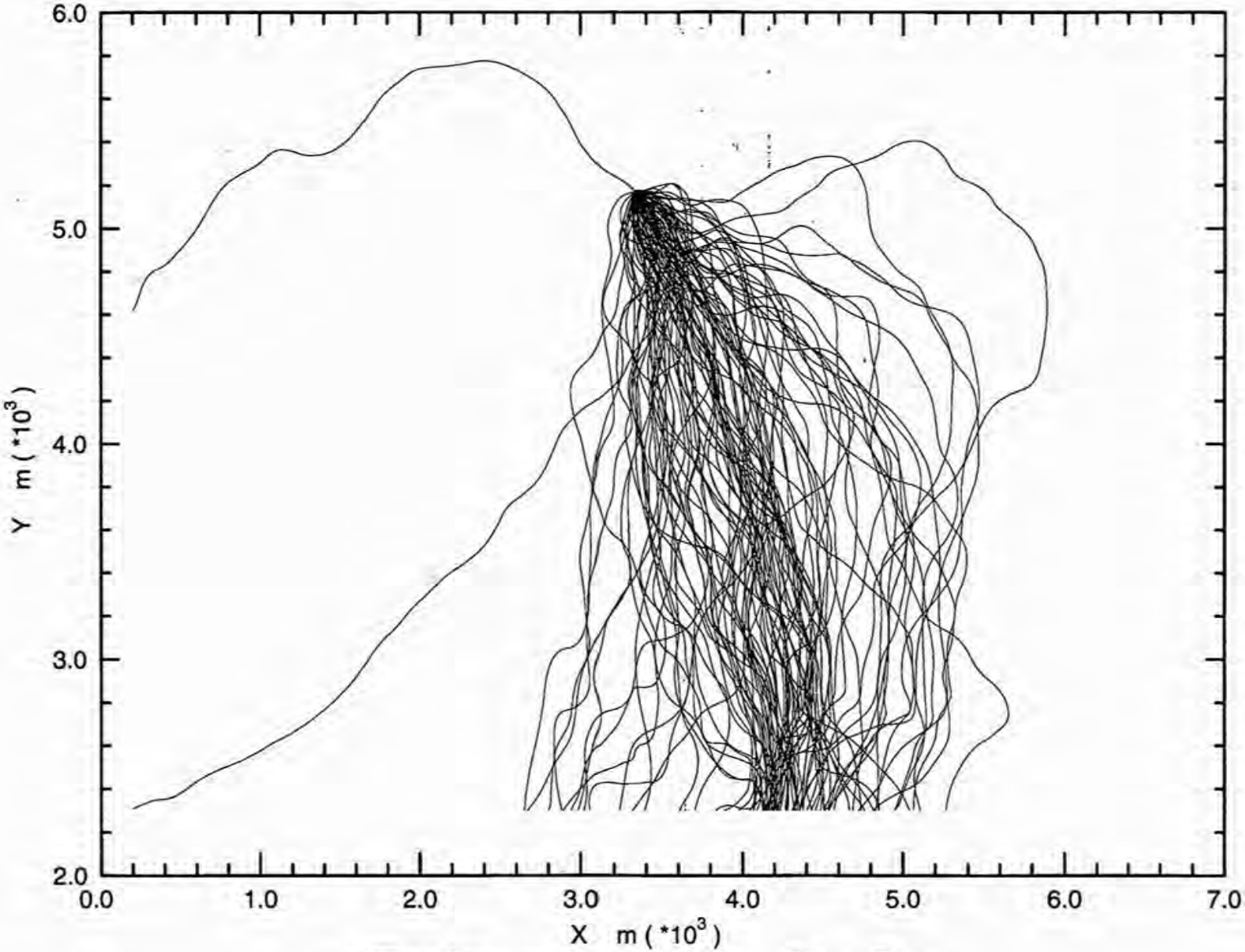

N1:[NOBACK.JLRAMSE.CCA.TRACKER]P_MINE.CMD;6

Information Only

SPLAT_PA96_2 1.02 10/29/96 16:32:08

Figure 7.13

Replicate 1, full mining particle tracks

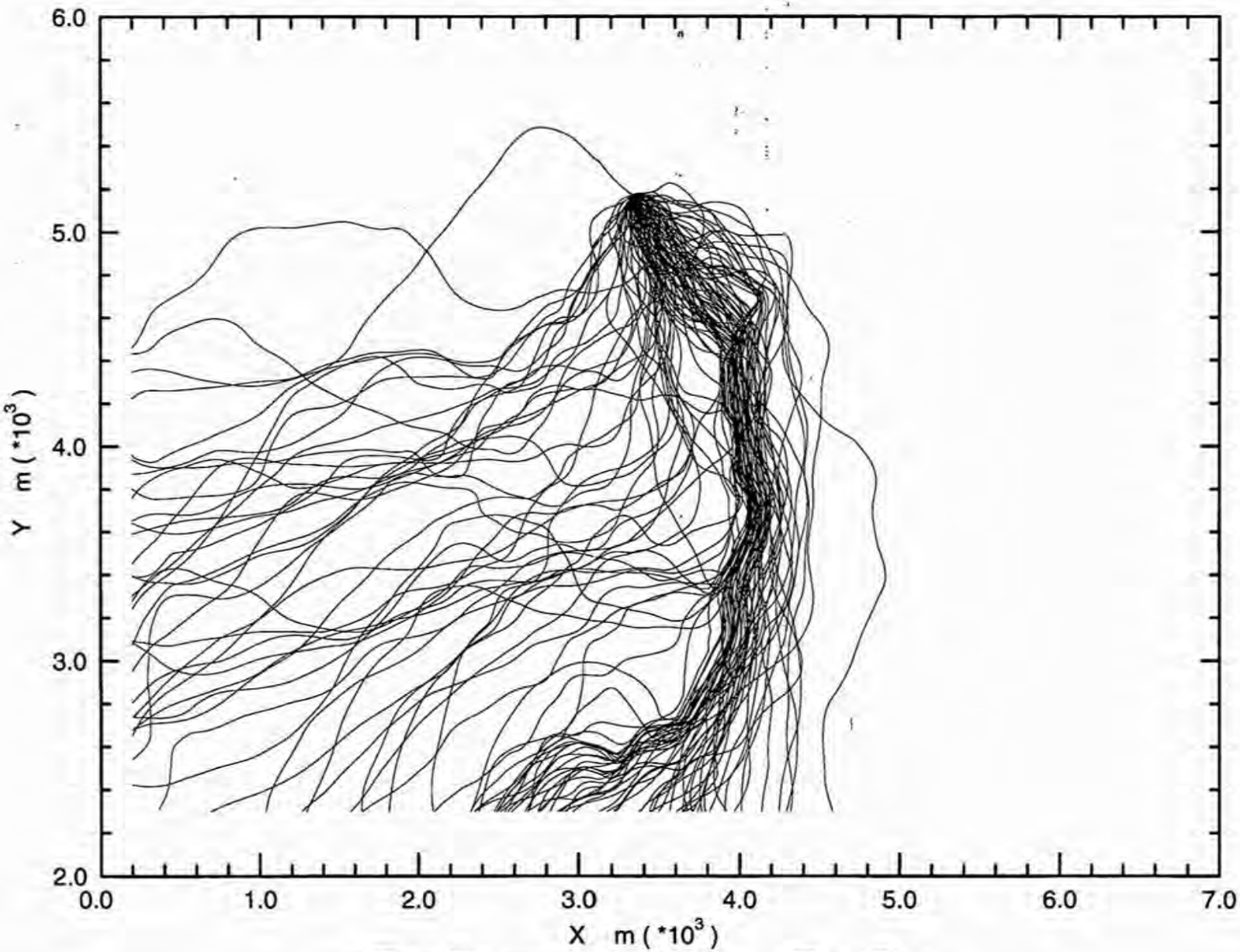

N1:[NOBACK.JLRAMSE.CCA.TRACKER]F_MINE.CMD;2

Information Only

SPLAT_PA96_2 1.02 10/29/96 16:49:46

7.2 Culebra Transport Results

In the first two replicates, there were no runs (input parameters combinations) in either the full or partial mining scenario's which led to a release at the WIPP land withdrawal boundary exceeding 10^{-30} kg in 10,000 years. In fact, most isotopes rarely moved outside the waste panel area in quantities considered to be significant. Only ^{234}U and its daughter product ^{230}Th were occasionally transported beyond the waste panel area, and then only when the sampled oxidation state for uranium was +6, or ^{234}U(VI). The reason ^{234}U(VI) is transported much further than ^{234}U(IV), ^{239}Pu(III), ^{239}Pu(IV), ^{241}Am(III), or injected ^{230}Th(IV), is thought to be a consequence of the relatively low range of matrix distribution coefficients (kd) for this species. As shown in Table 7.1, the range of kd's are significantly lower for ^{234}U(VI) than for any other isotope / oxidation state investigated.

Table 7.1 Matrix Distribution Coefficients

Isotope Low / High Oxidation State	Low Oxidation State kd range (m^3/kg)	High Oxidation State kd range (m^3/kg)
^{234}U (IV) / (VI)	0.9 to 20	0.00003 to 0.03
^{239}Pu (III) / (IV)	0.02 to 0.5	0.9 to 20
^{241}Am (III) / (III)	0.02 to 0.5	0.02 to 0.5
^{230}TH (IV) / (IV)	0.9 to 20	0.9 to 20

In the first replicate, the transport of ^{234}U was greatest in run #78 of the partial mining scenario. In this run, the sampled oxidation state is above 0.5, so the "high" oxidation state kd's were used (see Appendix D). The sampled ^{234}U(VI) kd for this run is not, however, all that small ($1.14 * 10^{-2}$ m^3/kg), indicating other input parameters such as the groundwater flow velocities, matrix block half length, and/or advective porosity may also influence transport behavior.

Contour plots of the concentration of ^{234}U in the advective continuum at 10,000 years for run #78 of replicate 1 with partial mining are presented in Figures 7.14 and 7.15. In Figure 7.14, the concentration of ^{234}U is plotted over the entire local problem domain, and in Figure 7.15, the plume and waste panel area are shown in more detail. The dot in the center of the waste panel area is the location of the intrusion borehole, or source point, and the star near the center of the plume is the maximum concentration. Notice the plume of ^{234}U extends only slightly beyond the waste panel area and does not even approach the land withdrawal boundary.

Filled contour plots of ^{239}Pu, ^{241}Am, ^{230}Th, and ^{230}Th daughter product, for the same run are presented in Figures 7.16 through 7.19, respectively. Only the ^{234}U daughter product, ^{230}Th, is transported beyond the waste panel area, and one can deduce from Figures 7.18 and 7.19 that the transport of this species is predominately a consequence of ^{234}U transport.

Information Only

The effects of full mining versus partial mining on the transport ^{234}U in run #78 of replicate 1, are shown in Figure 7.20. This diagram clearly shows that mining as implemented in the performance assessment is sometimes beneficial to compliance. This finding is consistent with that of Section 7.1, which showed that potash mining generally leads to a diversion of flow in the waste panel area, reducing the magnitude and potentially changing the direction of flow in this region.

In contrast to the ^{234}U transport depicted in Figures 7.13 and 7.14, most runs exhibited significantly lower transport distances. For the partial mining scenario of replicate 1, the run with the lowest maximum concentration of ^{234}U at the end of the simulation was run #100. A contour plot of the ^{234}U advective continuum concentration for this run is shown in Figure 7.21.

Therefore, in replicate 1, the transport of ^{234}U was bounded by that shown in Figures 7.15 and 7.18, and the transport of the remaining isotopes was generally less than that of ^{234}U and always contained within the waste panel area. The lone exception to the preceding statement is the ^{234}U daughter product, ^{230}Th, was also observed outside the waste panel area but thought to be due to the decay of ^{234}U rather than transport characteristics of ^{230}Th. Furthermore, none of the isotopes simulated in either of the first two replicates moved anywhere near the land withdrawal boundary in quantities sufficient to be characterized as a release (greater than 10^{-30} kg integrated discharge).

Replicate 3 was very similar to the first two replicates in that the transport of all isotopes was generally restricted to the waste panel area. The single exception involved run #33, in which ^{234}U and daughter product ^{230}Th were transported to the land withdrawal boundary and beyond in both the full and partial mining scenario's. Contour plots of the concentration of both isotopes in the advective continuum are presented in Figures 7.22 and 7.23 for the partial mining scenario, and Figures 7.24 and 7.25 for the full mining scenario. These diagrams show the transport of ^{234}U can be substantial given the appropriate combination of input parameters. The integrated discharge of each isotope after 10,000 years for run #33 of replicate 3 is provided in Table 7.2.

Table 7.2 - Integrated Discharge, Run #33, Replicate 3

Run #	Replicate	Mining	$^{239}Pu(IV)$ (kg)	$^{241}Am(III)$ (kg)	$^{234}U(VI)$ (kg)	$^{230}Th(IV)$ (kg)	$^{234}U(VI) \rightarrow {}^{230}Th(IV)$ (kg)
33	3	Full	0	0	0.91158	0	2.99276E-7
33	3	Partial	0	0	0.11183	0	1.46536E-8

Run #33 of replicate 3 was the only combination of input parameters leading to a non-zero release at the land withdrawal boundary. This vector contains a sampled oxidation state for ^{234}U of VI, one of the lowest sampled values of k_d for $^{234}U(VI)$, $3.96 * 10^{-5}$ m^3/kg, and a velocity field capable of transporting ^{234}U to the highly conductive flow regions to the east. ^{230}Th is also released in small quantities, but only as the daughter product of ^{234}U. After careful analysis of this and similar parameter combinations it appears a relatively small k_d and a flow field

Information Only

possessing a certain magnitude and direction are necessary to transport radioisotopes to the land withdrawal boundary. This particular combination occurred only twice (run #33 partial mining and run #33 full mining) in the 600 parameter sample sets indicating a low probability of occurrence. The driving force of the low probability appears to be k_d, however, additional simulations and sensitivity analysis are necessary to verify this interpretation.

Information Only

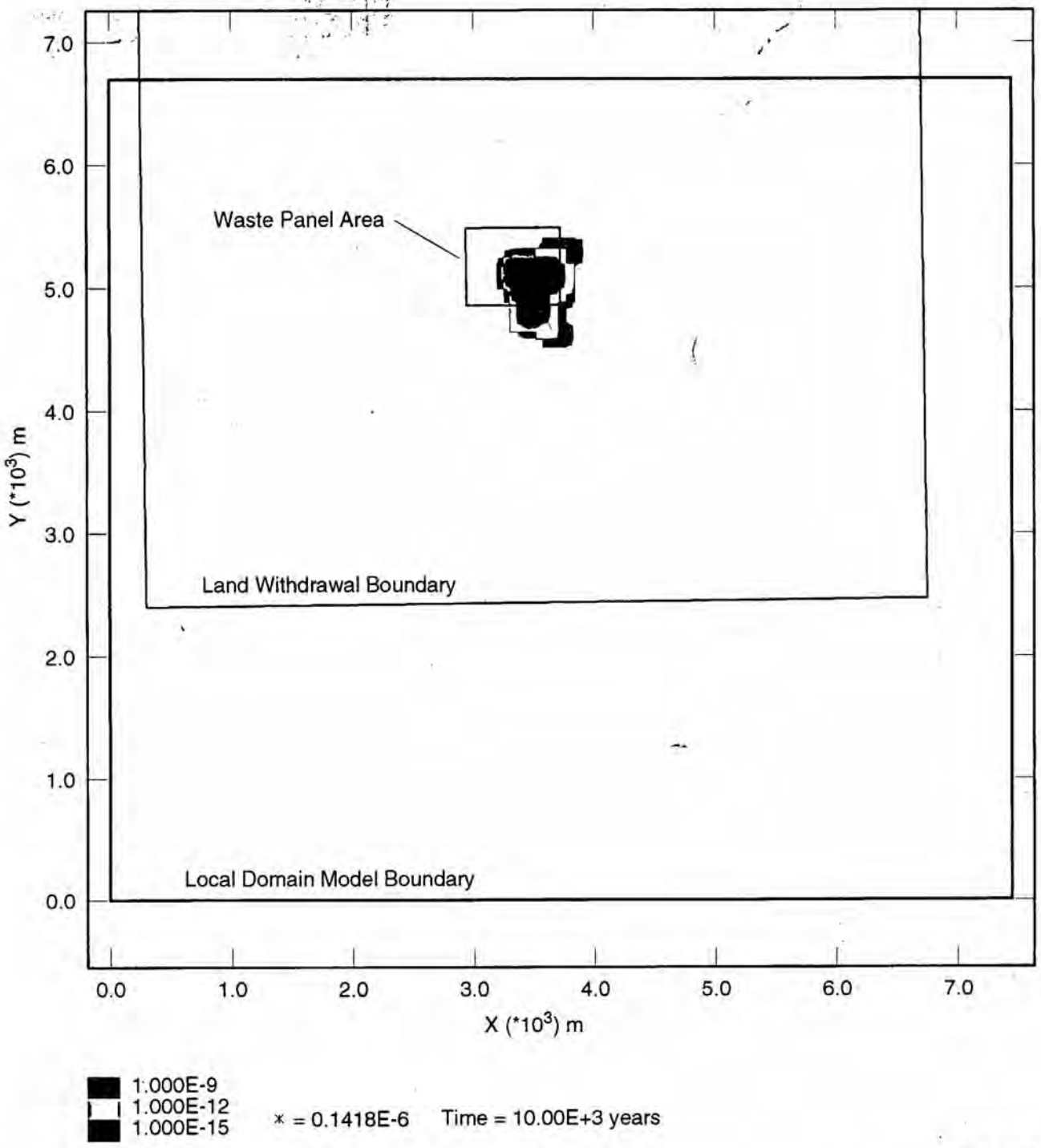

Figure 7.14. ^{234}U Fracture Concentration (kg/m^3) [ST2D3_CCA_R1_V078_PM.CDB;1]

Information Only

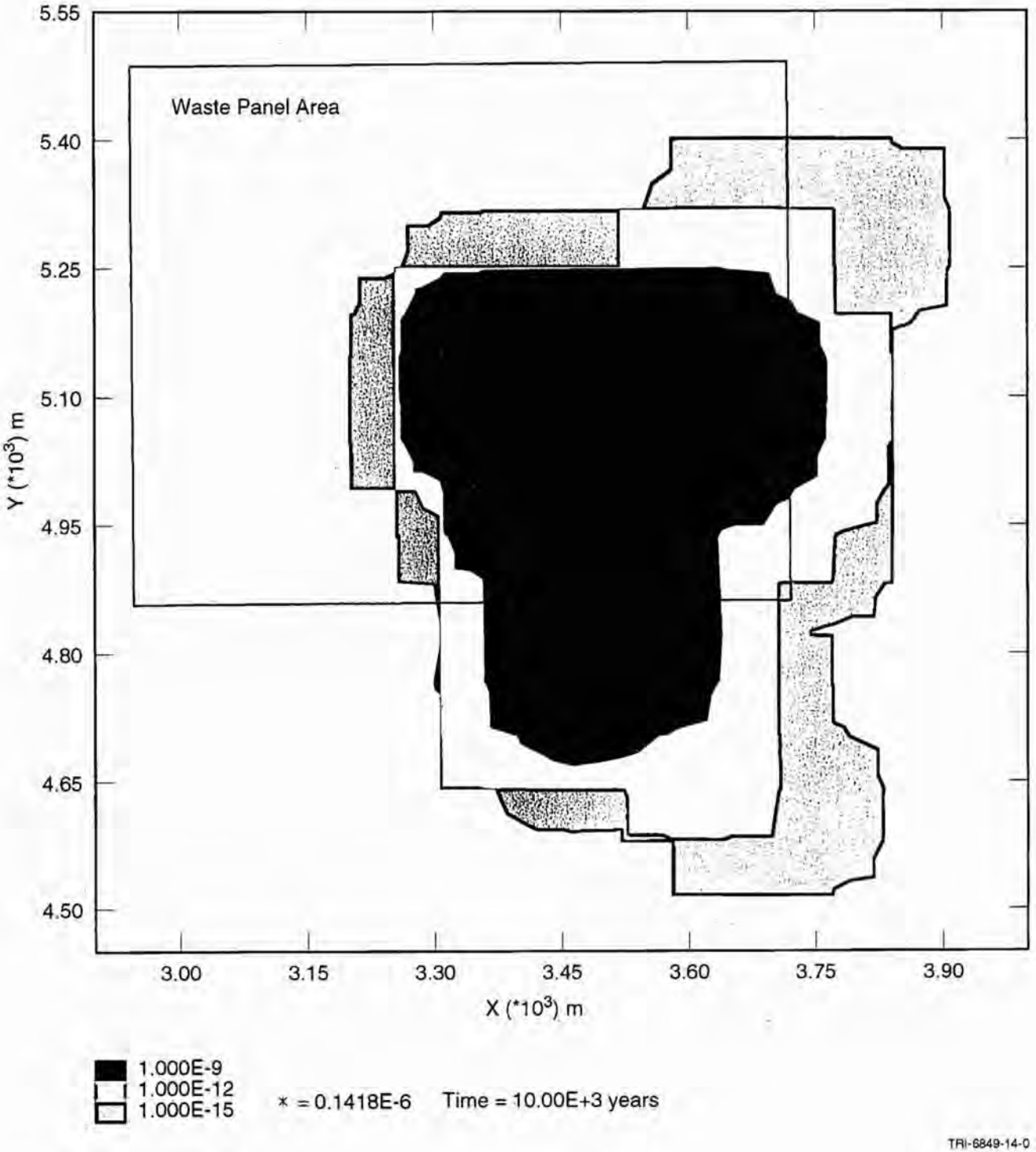

Figure 7.15. ^{234}U Fracture Concentration (kg/m^3) [ST2D3_CCA_R1_V078_PM.CDB;1]

Information Only

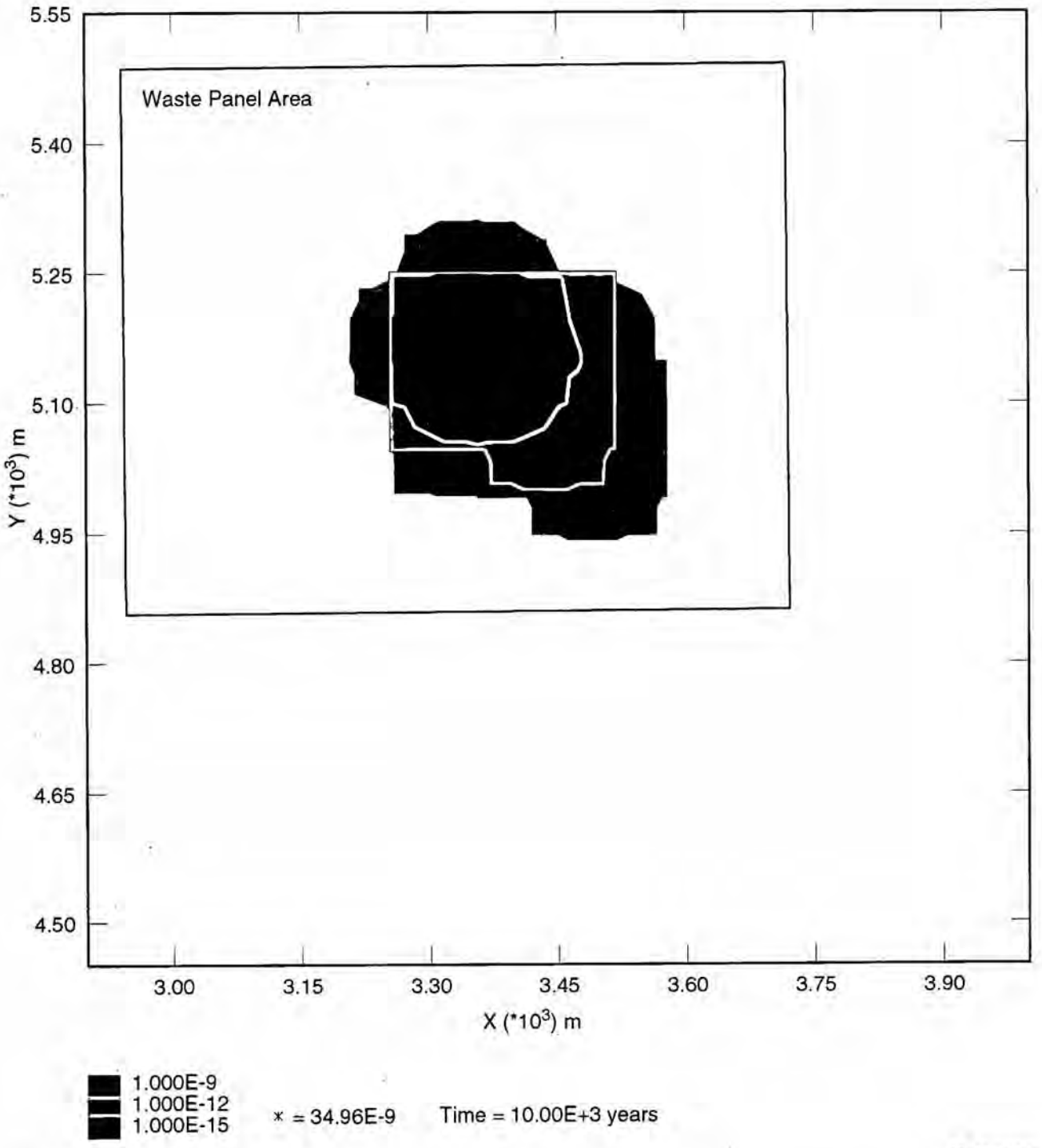

Figure 7.16. ^{239}Pu Fracture Concentration (kg/m^3) [ST2D3_CCA_R1_V078_PM.CDB;1]

Information Only

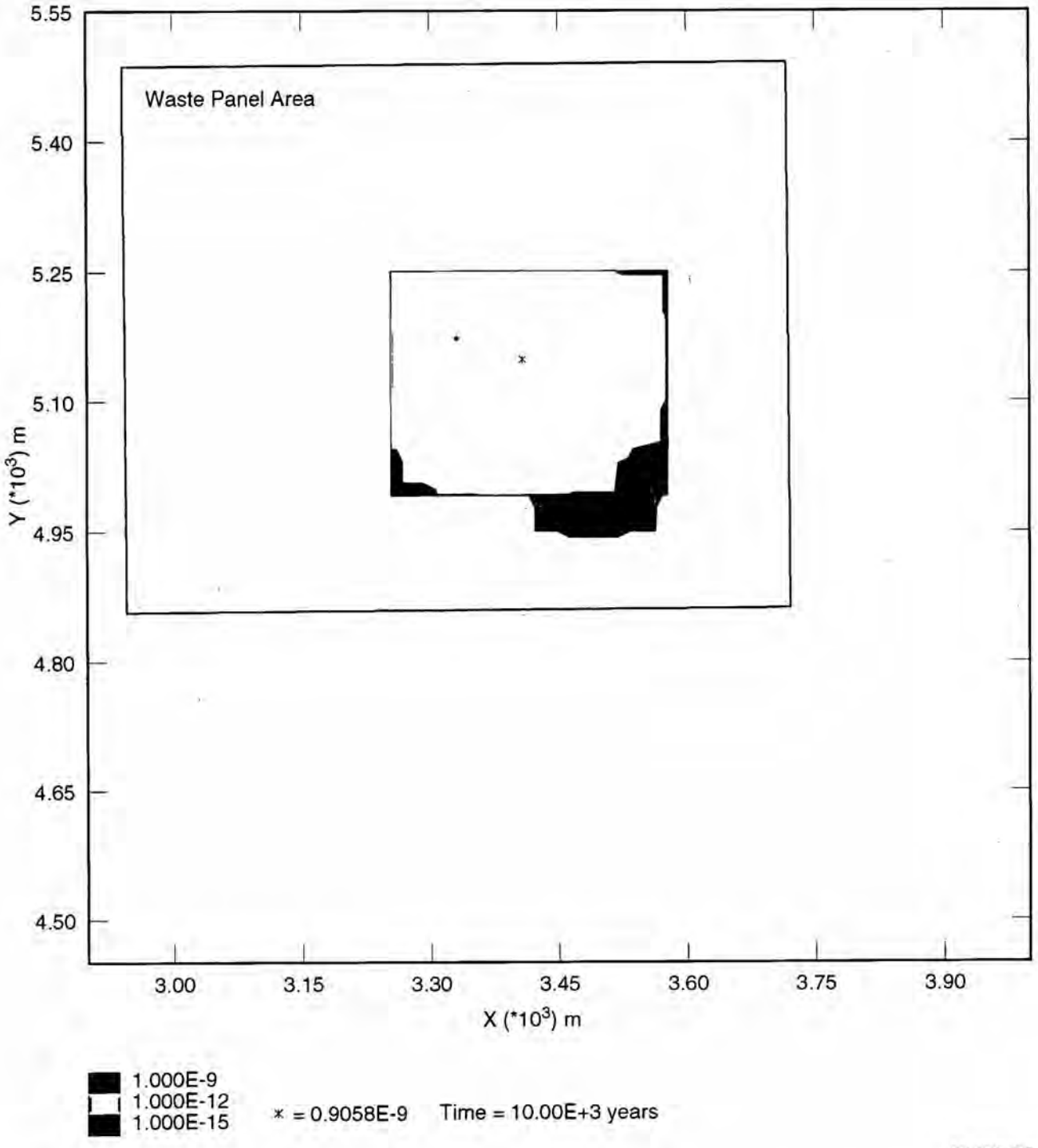

Figure 7.17. ^{241}Am Fracture Concentration (kg/m^3) [ST2D3_CCA_R1_V078_PM.CDB;1]

Information Only

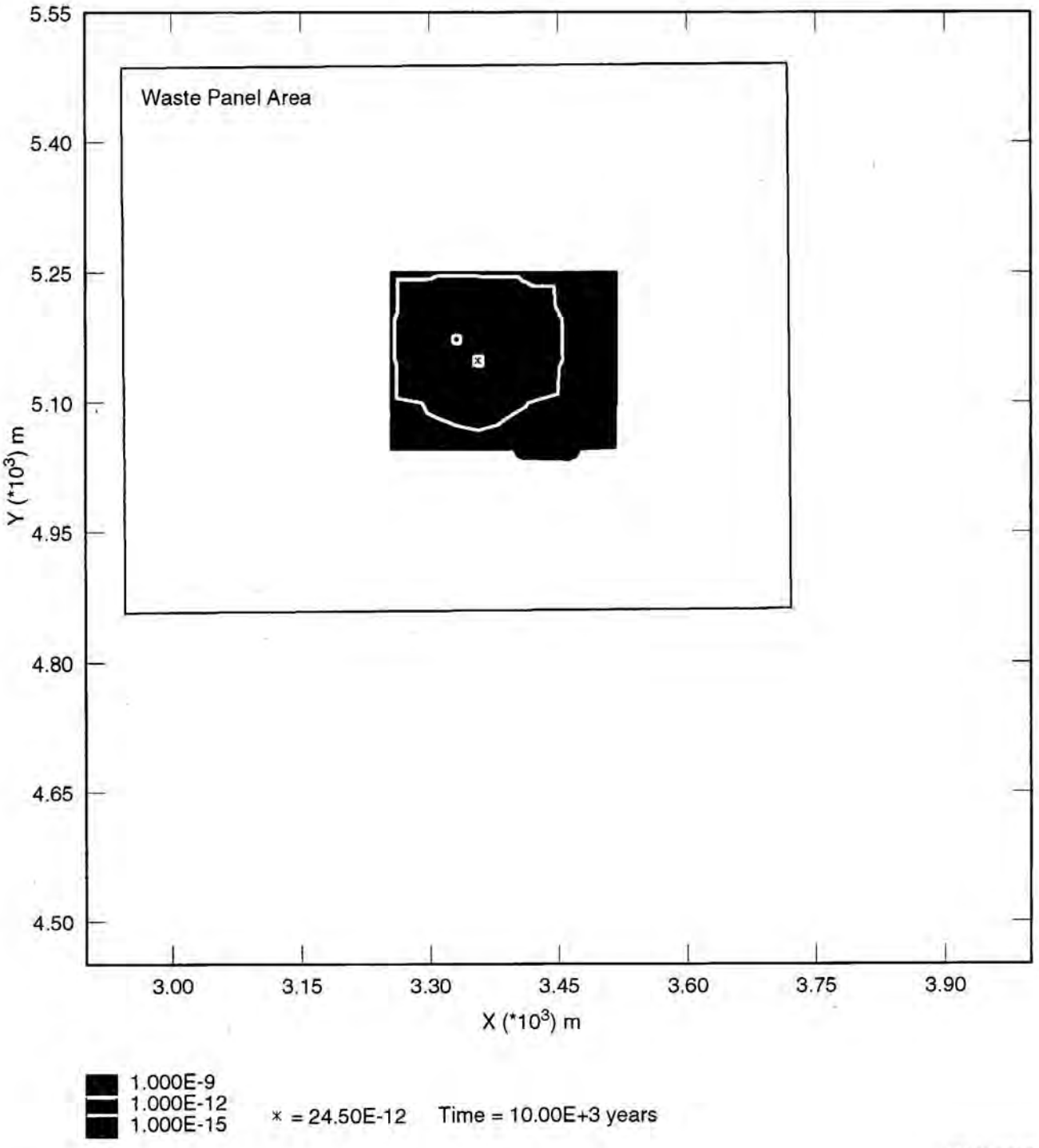

Figure 7.18. ^{230}Th Fracture Concentration (kg/m^3) [ST2D3_CCA_R1_V078_PM.CDB;1]

Information Only

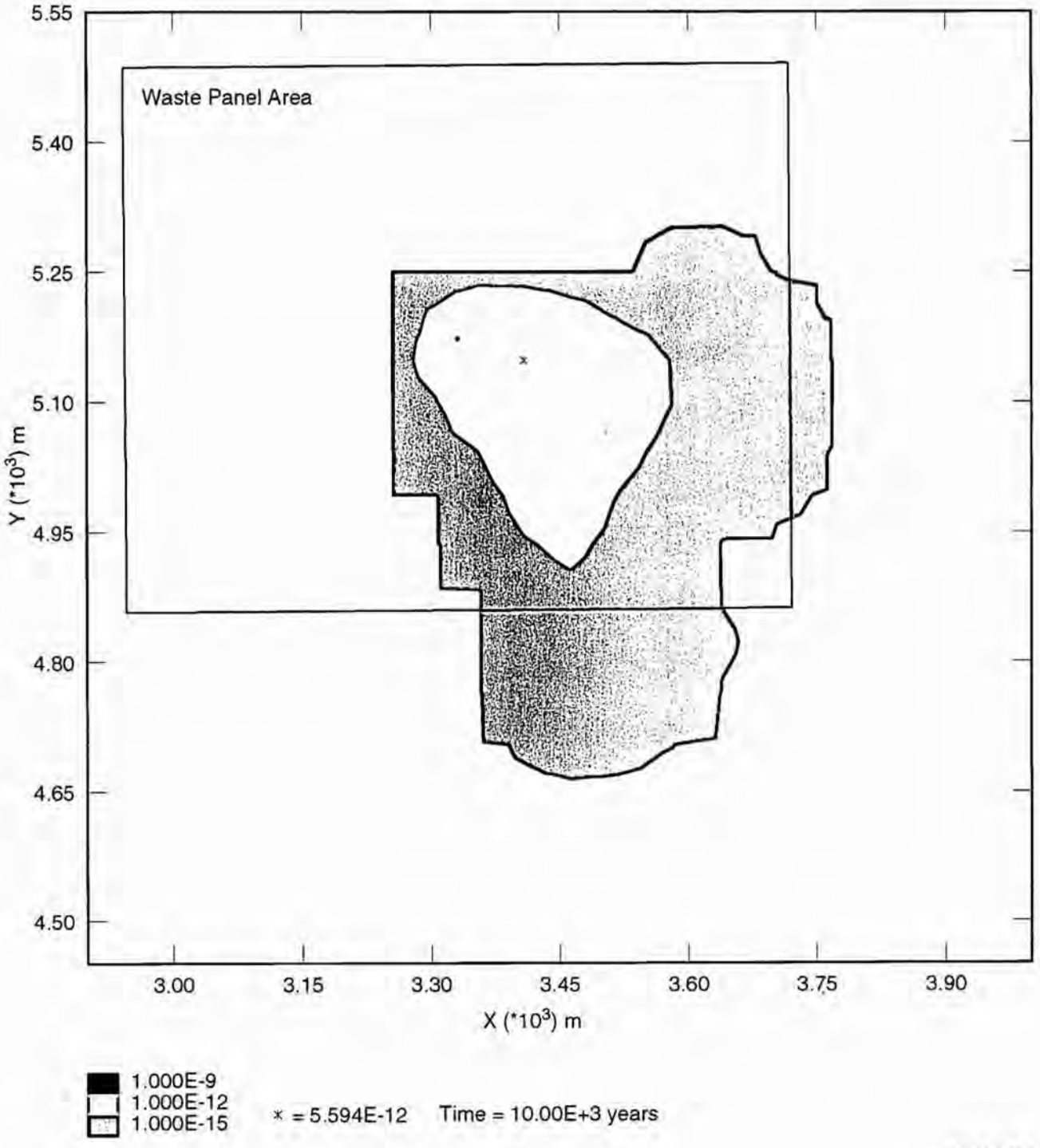

Figure 7.19. ^{230}Th Daughter Product Fracture Concentration (kg/m^3) [ST2D3_CCA_R1_V078_PM.CDB;1]

Information Only

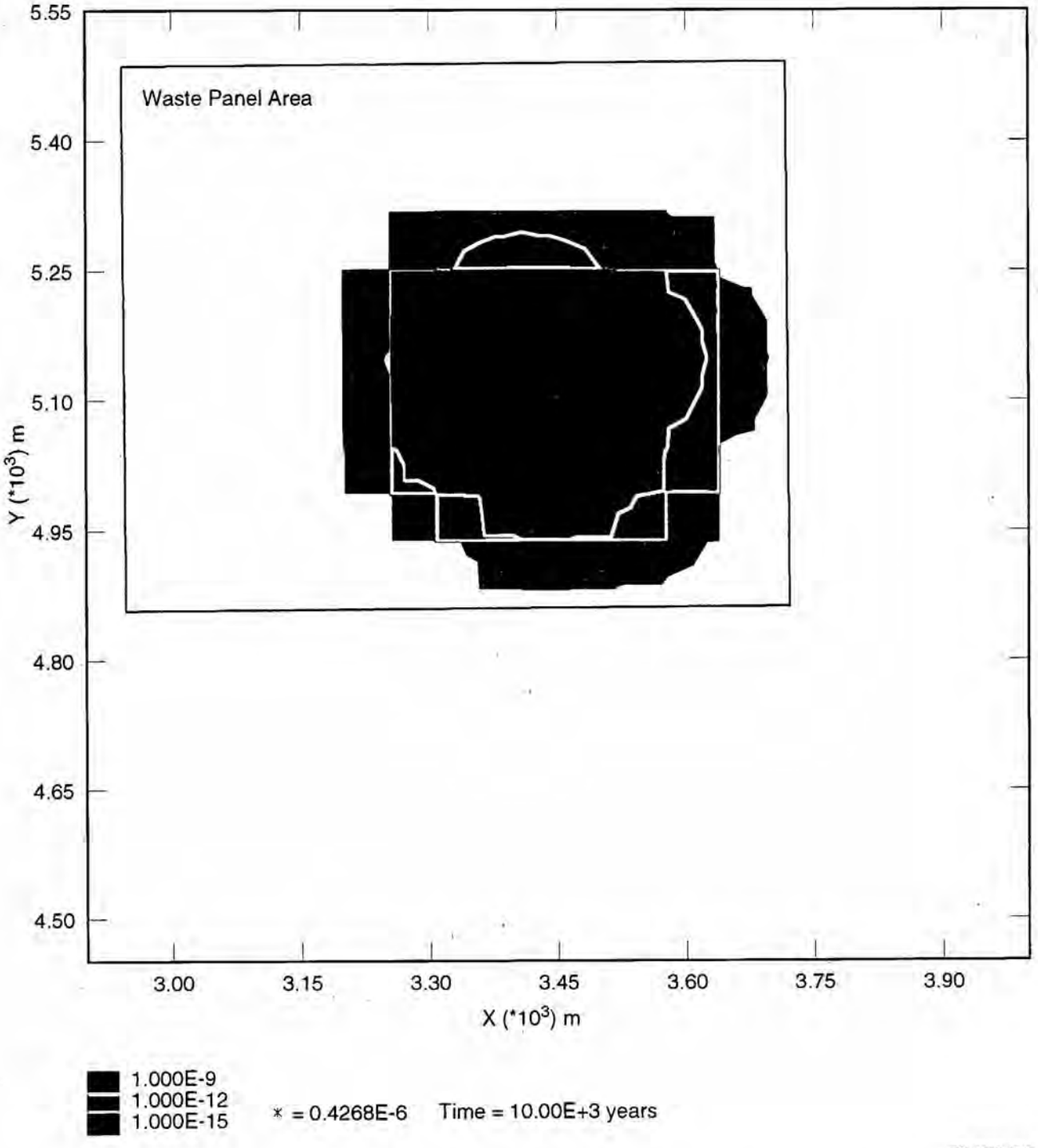

Figure 7.20. ^{234}U Fracture Concentration (kg/m^3) [ST2D3_CCA_R1_V078_FM.CDB;1]

Information Only

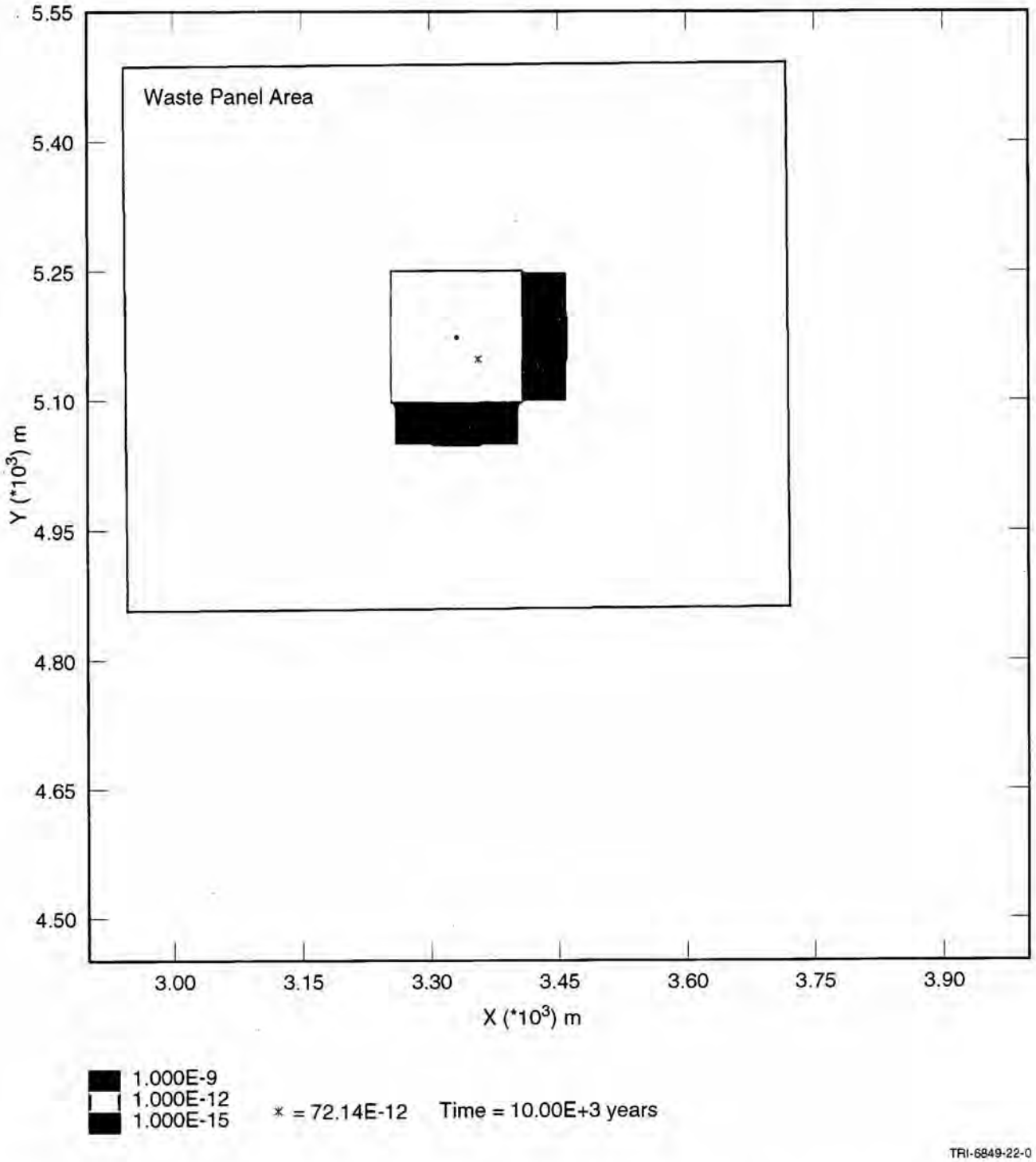

Figure 7.21. ^{234}U Fracture Concentration (kg/m^3) [ST2D3_CCA_R1_V100_PM.CDB;1]

Information Only

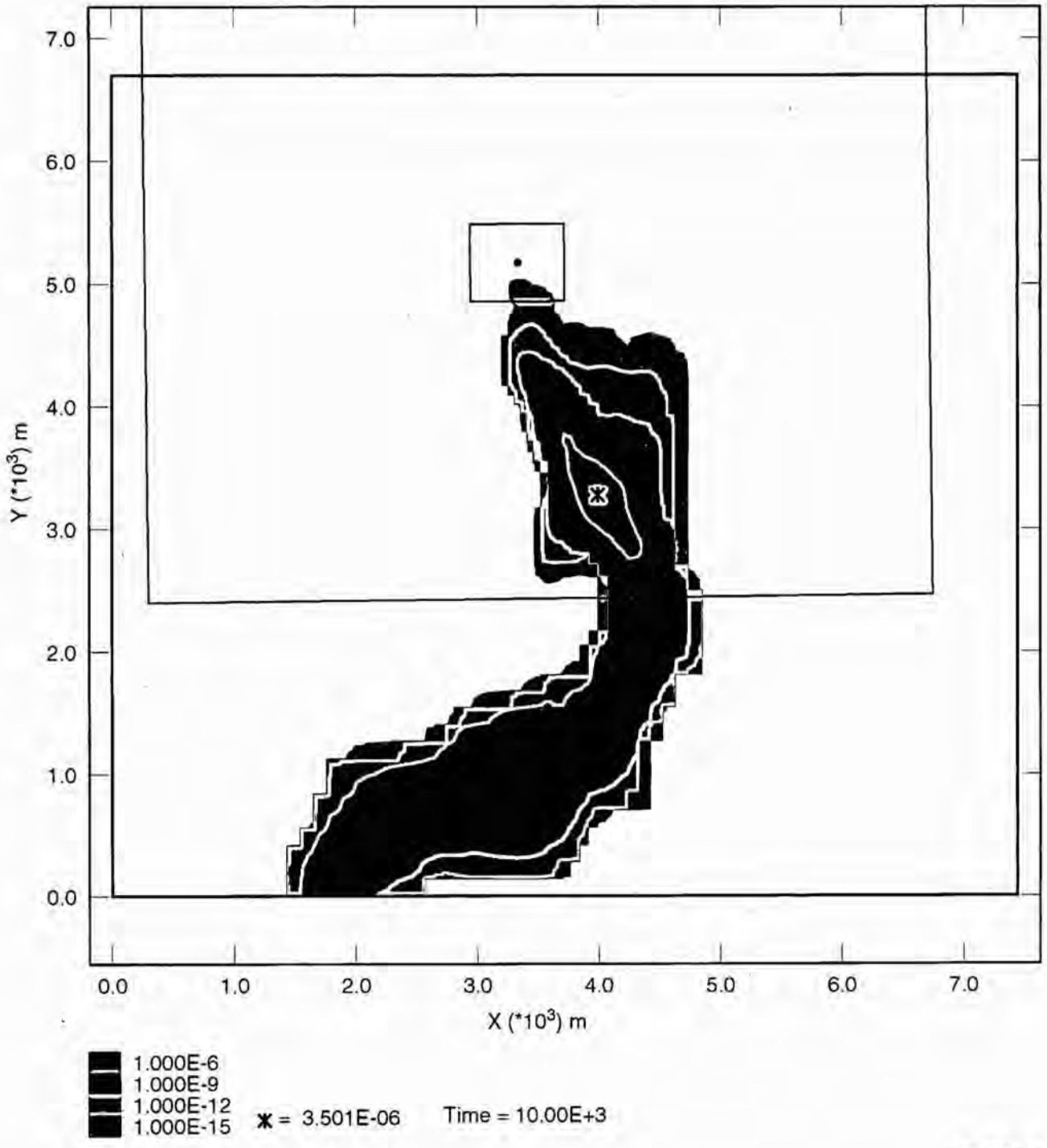

Figure 7.22. U_{234} Fracture Concentration (kg/m^3) [ST2D3_CCA_R3_V033_PM.CDB;1]

Information Only

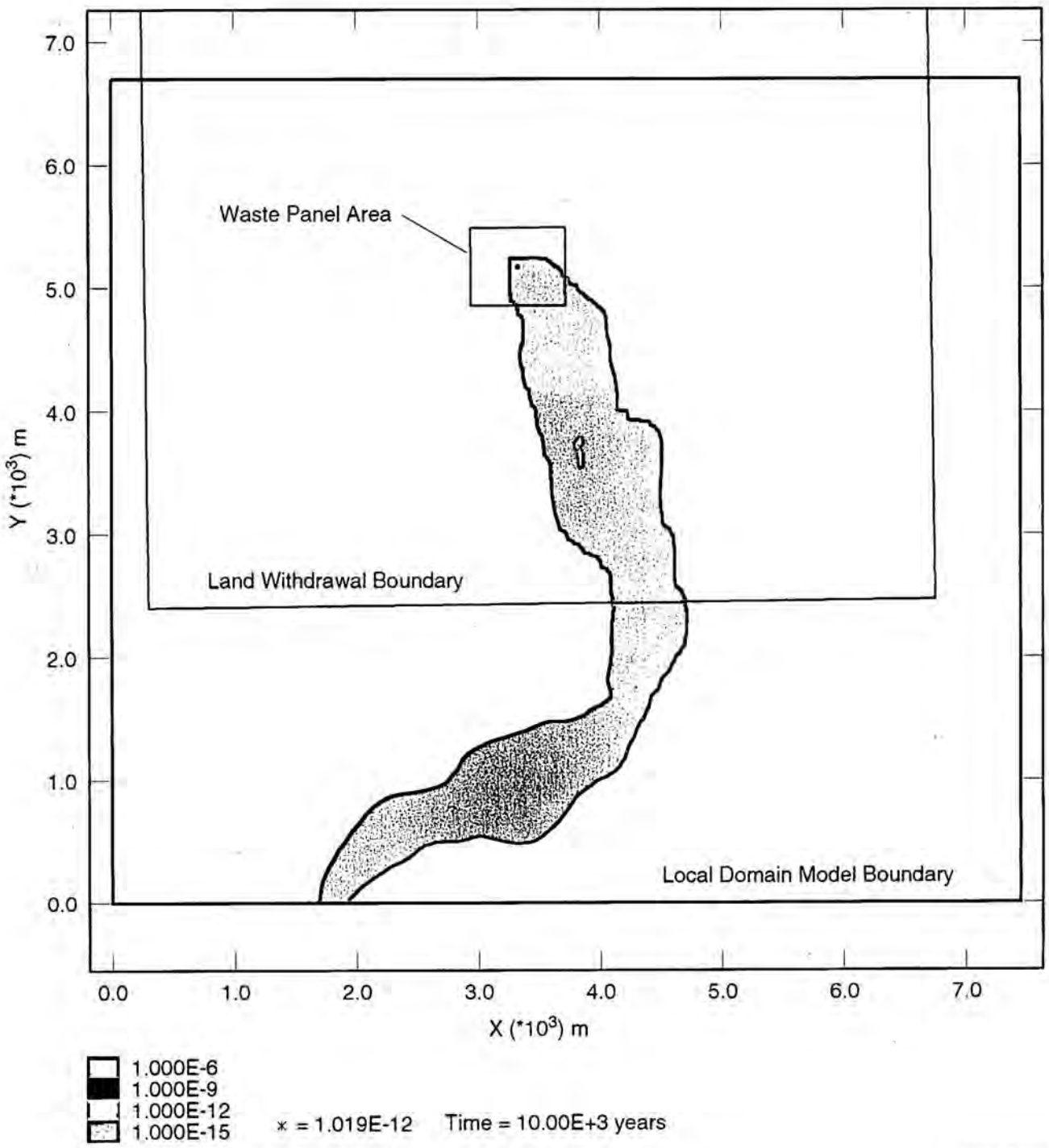

Figure 7.23. ^{230}Th Daughter Product Fracture Concentration (kg/m^3) [ST2D3_CCA_R3_V033_PM.CDB;1]

Information Only

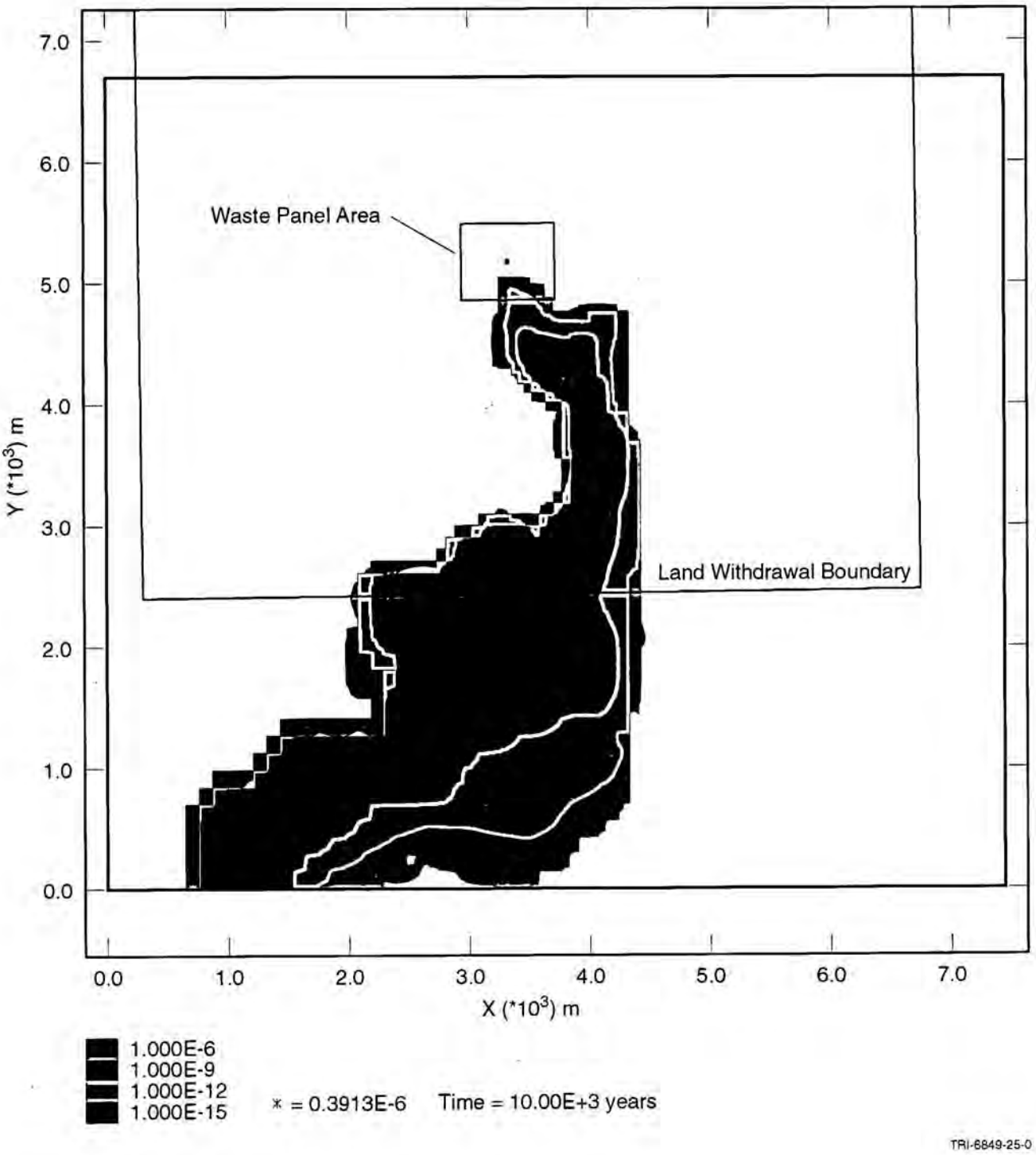

Figure 7.24. ^{234}U Fracture Concentration (kg/m^3) [ST2D3_POSTCCA_R3_V033_UTH.CDB;1]

Information Only

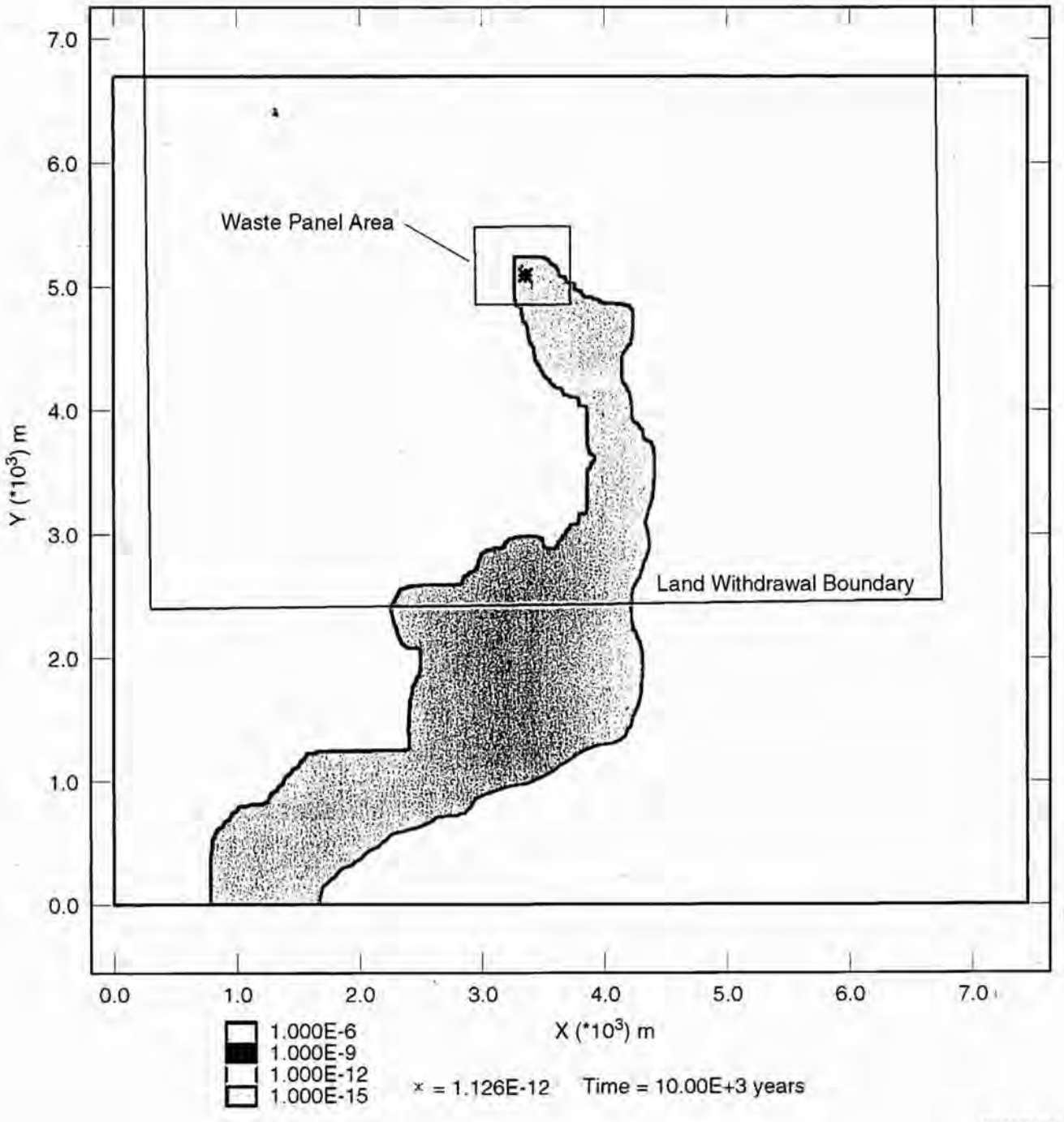

Figure 7.25. 230Th Daughter Product Fracture Concentration (kg/m³) [ST2D3_POSTCCA_R3_V033_UTH.CDB;1]

Information Only

7.3 Solution Convergence

In preparation for this analysis, the temporal and spatial discretization of the flow and transport governing equations was studied to design a computational mesh and select a time step which limits truncation error to an acceptable level in a computationally feasible manner (Wallace, 1996c). This work was performed using the transmissivity fields and transport parameters used in the 1992 performance assessment. The metric used to evaluate solution convergence was isotope integrated discharge at the land withdrawal boundary and isotope contour plots. This study resulted in the local domain computational mesh used this in analysis, Figure 2.5, and the selection of a time step for the transport simulations of 1.333 years (7500 time steps). With the addition of potash mining and parameter changes to the matrix distribution coefficients it is uncertain whether the solution convergence work done in this study is entirely applicable to this analysis. This work does however, suggest the CCA solutions are reasonably converged in space for parameter sets possessing relatively low matrix distribution coefficients.

This section does not contain a thorough and detailed study of the solution convergence in the 1996 CCA Culebra flow and transport calculations. Such a study is most certainly warranted but may be difficult to conduct given the number of simulations performed and a perceived influence the model input parameters may have on solution convergence. Preliminary findings are however, presented in Section 7.3.1 to examine the spatial discretization of the 1996 CCA calculations. These findings were drawn from a set of calculation in which a highly discretized, much smaller, problem domain was studied. The primary purpose of this study was to examine parameter sensitivity, but some questions regarding spatial discretization can be addressed. The parameter sensitivity study is currently in progress so the results of this study are not included in this report.

Temporal convergence of the transport solutions is investigated in Section 7.3.2 by examining the Courant number at different locations in the computational domain. Several simulations identified using the Courant number as a time step criteria were found to possess some degree of temporal discretization error. A select few of these simulations were chosen to be re-run with a smaller time step to investigate the magnitude of this error and the resulting impact on the integrated discharge at the land withdrawal boundary.

7.3.1 Spatial Discretization

The spatial discretization error of the 1996 CCA Culebra flow and transport calculations appears to be large for some runs but probably small for others. These errors can be attributed two sources; misrepresentation of the radioisotope source, and limited resolution in the computation mesh leading to spatial truncation error. The degree to which both types of error influence the transport solution appears to be a function of the input parameters to the transport model. Hence, the spatial discretization error is thought to vary from one simulation to the next.

The first source of error, results from the use of a 50 x 50 m grid block to inject radioisotopes into the Culebra. Conceptually, the source of radioisotopes to the Culebra is a intrusion borehole

Information Only

with a diameter of 12.25 inches (0.3115 m). By injecting radioisotopes into a relatively large 50 x 50 m grid block rather than a grid block more representative of an intrusion borehole (i.e. 0.25 by 0.25 m), the source is artificially dispersed. The impact of this artificial dispersion on the transport solution can be conservative in that the transport distance is enhanced through the initial dispersion. The impact however, can also be nonconservative due to the substantial reduction in radioisotope concentrations.

To examine the severity of the intrusion borehole misrepresentation on the results of this analysis, selected results from a study initiated to investigate parameter sensitivity are presented below. The study is based on a set of 100 calculations performed using the 1996 CCA replicate 1 partial mining parameter sets. Only ^{234}U was simulated in this set of calculations. ^{234}U was selected as the sole isotope to transport because the parameter range for the matrix distribution coefficient, k_d, encompasses the parameter ranges of all other isotopes modeled in the CCA.

To ensure meaningful discharges for the sensitivity analysis, the local model domain was substantially reduced in size from the CCA analysis, and the transport of ^{234}U was recorded across four different boundaries. The model domain, shown in Figure 7.26, extends 13m in each direction except to the North where it extends only 8m. The discharge boundaries, also shown in Figure 7.26, are positioned at 3, 5, 7, and 10m from the center of the source. The minimum grid size is 0.25 x 0.25 m at the source, and the largest elements are 1 x 1 m.

The resulting local model domain is 26 x 21 m which when centered at the intrusion borehole is encapsulated by a single grid block in the regional model domain. Due to the relatively small local model domain the flow field was assumed to be uniform and steady. The direction and magnitude of the flow field was linearly interpolated from the regional groundwater flow simulation to the location of the intrusion borehole. The interpolated x and y components of the Darcy velocity were then applied uniformly over the entire local domain.

Time steps were chosen based on the Courant number, Cr, discussed in the following section. The minimum number of time steps needed to satisfy the criteria $Cr \leq 1$ in the 1 x 1 m cells, is presented in Figure 7.27. A minimum of 100,000 time steps were used in the analysis. Due to small cell sizes and occasionally high effective velocity (V/ϕ), as many as 10 million time steps were needed to satisfy the Courant number time step criteria. Runs requiring between 100,000 to 1,000,000 time steps were simulated using 1,000,000 time steps, and those runs requiring more than 1,000,000 time steps were run with the computed value in Figure 7.27.

Cumulative releases of ^{234}U across the 10m discharge boundary at the end of the 10,000 year simulation are shown in Figure 7.28. The isotope source consisted of the same 1 kg fifty year step function used the CCA calculations (see Section 2.0). The 10m integrated discharge values show that in the majority of the simulations the ^{234}U was essentially contained within this boundary. Furthermore, in only six of the one hundred simulations did 90% or greater of the isotope injected into the problem domain transport beyond the 10m discharge boundary. These six simulations possessed relatively low matrix distribution coefficients, ranging from $1.86 * 10^{-3}$ to $6.16 * 10^{-3}$ m^3/kg.

Information Only

Also of interest, is the lack of transport exhibited in run #78. This run, as discussed in Section 7.2, possessed the most significant ^{234}U transport of the partial mining, replicate 1, CCA calculations. The dramatic difference in results is due to several factors. First, the Darcy velocity is several orders of magnitude smaller in the sensitivity analysis calculation than in the CCA calculation (10^{-11} versus 10^{-8} m/s). This is due solely to the interpolation scheme used by SECOTP2D to transfer hydraulic properties from the regional to the local domain. As discussed in Section 2.5.1, deriving the local domain hydraulic conductivity through bi-linear interpolation of the regional hydraulic conductivity can result in artificially large flow fields. This potential problem was avoided in the sensitivity analysis calculations by assigning a uniform velocity derived through linear interpolation of the regional velocity field.

Other factors responsible for reduced transport in the sensitivity analysis shown by run #78 and many others are those discussed above. The inherent dispersion of the isotope by injecting the source into a 50 x 50m cell, combined with numerical dispersion due to the use of even larger cells in the surrounding area, clearly resulted in an overestimate of the transport distance in many of the simulations. For parameter sets containing relatively large matrix distribution coefficients the spatial discretization used in the CCA analysis was obviously inadequate to arrive at the unique solution to the governing set of partial differential equations

On the other hand, for parameter sets with relatively small matrix distribution coefficients, much of the ^{234}U was transported beyond the 10m boundary but it generally took several thousands of years to reach the arbitrary 0.90 kg discharge level. This behavior is displayed in Figure 7.29, where the integrated discharge of ^{234}U at the 10m discharge boundary is plotted as a function of time. The run numbers of each simulation with early releases and/or large cumulative releases are also shown on the diagram. Two of these runs are examined more closely to investigate the impact of injecting the source into a 50 x 50m cell in the CCA calculations. Run #93 and Run #10 were selected because they are the two largest releases, yet their transport behavior is quite different.

In Run #93, approximately 0.9 kg of the 1 kg source passed beyond the 10 m discharge boundary in the first 1,000 years. Contour plots of the concentration of ^{234}U in Run #93 at 1,000 and 10,000 years are presented in Figures 7.30 and 7.31, respectively. These Figures show the plume remains fairly compact in the transverse direction to flow but disperses significantly in the direction of flow due to matrix diffusion and retardation. Dispersion in the longitudinal direction is, however, obviously much smaller than the artificial dispersion created by injecting the source into a 50 x 50 m grid block. Based on these results, one can conclude that near borehole transport is not well represented in the CCA, and that for the case of Replicate 1 Run #93, this misrepresentation may cause the transport of ^{234}U to be underestimated.

As for Run #10, almost all of the ^{234}U injected into the problem moved beyond the 10m discharge boundary, but the transport was extremely slow. As shown in Figure 7.32, very little of the isotope penetrated the 10m discharge boundary in 1,000 years, and dispersion of the plume in the longitudinal direction is consistent with that observed in Run #93. Once again, the

Information Only

longitudinal dispersion is much smaller than the dispersion induced by injecting the source into a 50 x 50 m source term cell, however, it is probably safe to assume that the additional dispersion is more than compensated for by reduced travel time to the boundary of 50m grid block. From Figure 7.29, one can estimate it would take at least 5,000 years for the isotope to reach the boundary of the 50m grid block in any kind of appreciable quantity, where it would then be available for subsequent transport. This is in contrast to the CCA calculation in which all the mass injected into the problem domain is immediately available for transport beyond 50 meters.

One conclusion that can be drawn from this limited analysis of the spatial convergence of 1996 CCA calculations is that near borehole transport was not modeled well in the CCA resulting in an overestimation of the transport of isotopes possessing large matrix distribution coefficients and potentially underestimating the transport of isotopes with relatively small matrix distribution coefficients. The fact the near borehole transport was not modeled well in the CCA is not surprising since the computational mesh was designed to predict the migration of isotopes capable of reaching the land withdrawal boundary (approximately 2.5 km from the source). Obviously, quite a large population of the parameter sets simulated in the CCA do not stand a chance of reaching the land withdrawal boundary in 10,000 years. Perhaps a parameter screening argument should have been made to eliminate these runs from the analysis, rather than the brute force approach adopted.

Concerning runs with fairly fast and quantitatively significant transport (i.e.. Run #93), more time and effort are required to evaluate the spatial discretization used in the CCA. However, using 1992 PA parameters and flow fields, Wallace (1996c) found the spatial discretization used in the CCA calculations to be adequate. It is anticipated the same conclusion will be drawn regarding Run #93 and other similar runs at some point in the future.

Information Only

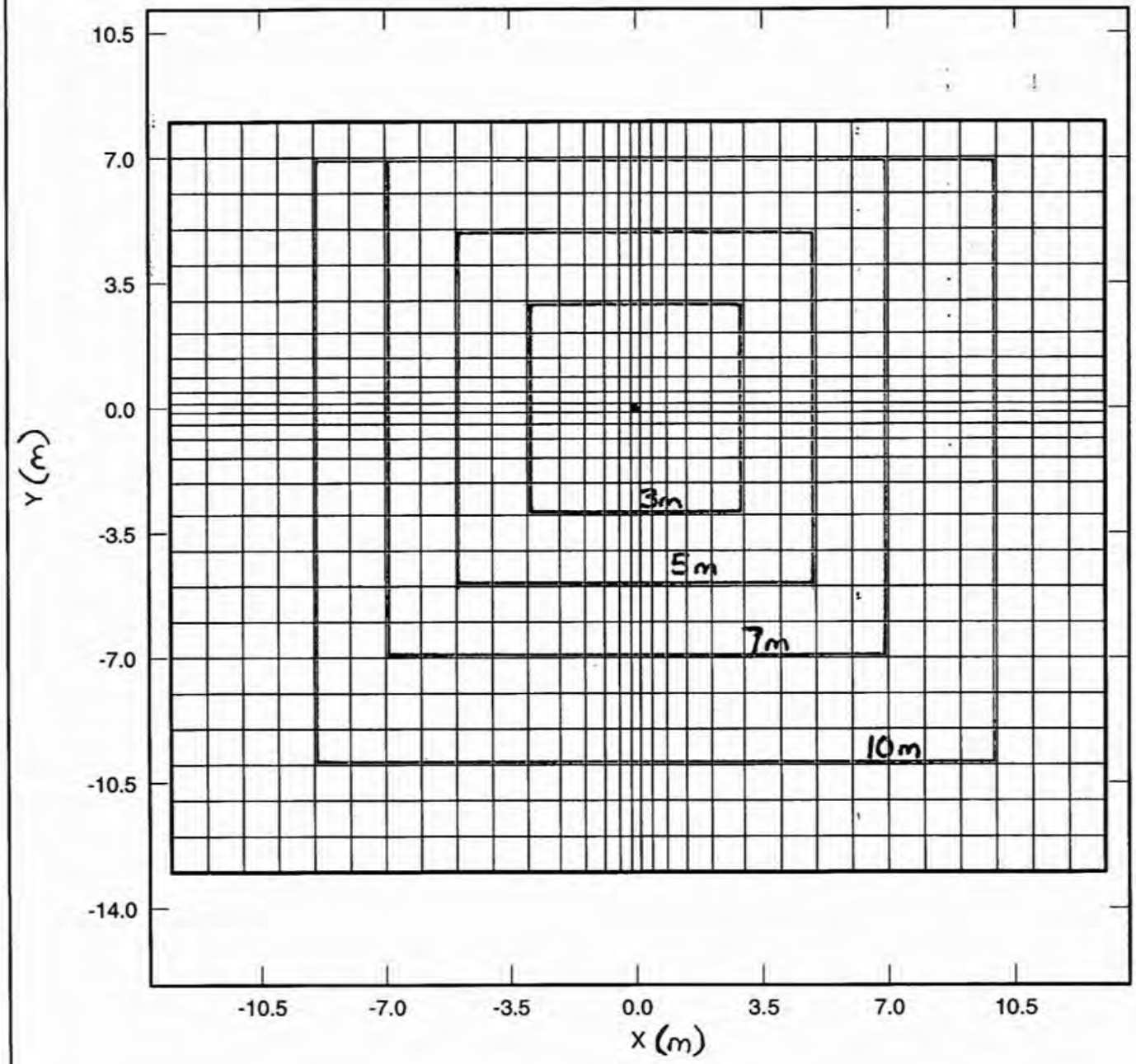

GM_PA96 6.08 08/26/96
RELATE_P 1.43 08/26/96
RELATE_P 1.43 08/27/96
POSTSECO 1.02 08/28/96
ALGEBRAC 2.35 09/15/96
ALGEBRAC 2.35 09/15/96

NO Deformation

Element Blocks Active:
1 of 1

Figure 7.26

Computation mesh used in the Culebra flow and transport sensitivity analysis

Time = 0.0000

DISK$IKE_CCA3:[PANEL.JWGARNE.SECO]ST2D3_SA1_R1_V078_PM.CDB;1 BLOTCDB_PA96 1.37 09/16/96 14:26

Information Only

Figure 7.27

Time Steps required to satisfy Cr = 1
Replicate 1, Partial Mining

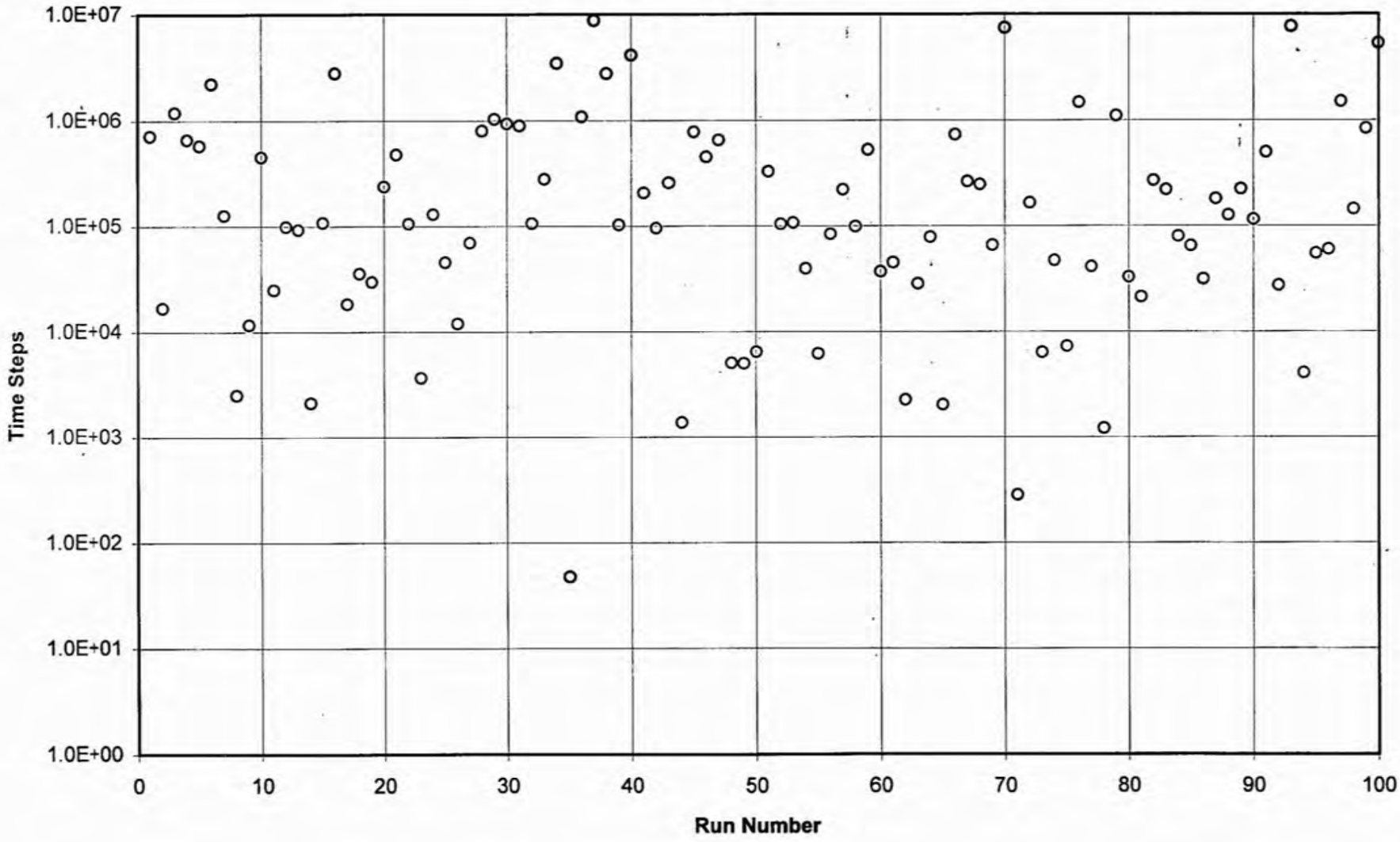

Information Only

Figure 7.28

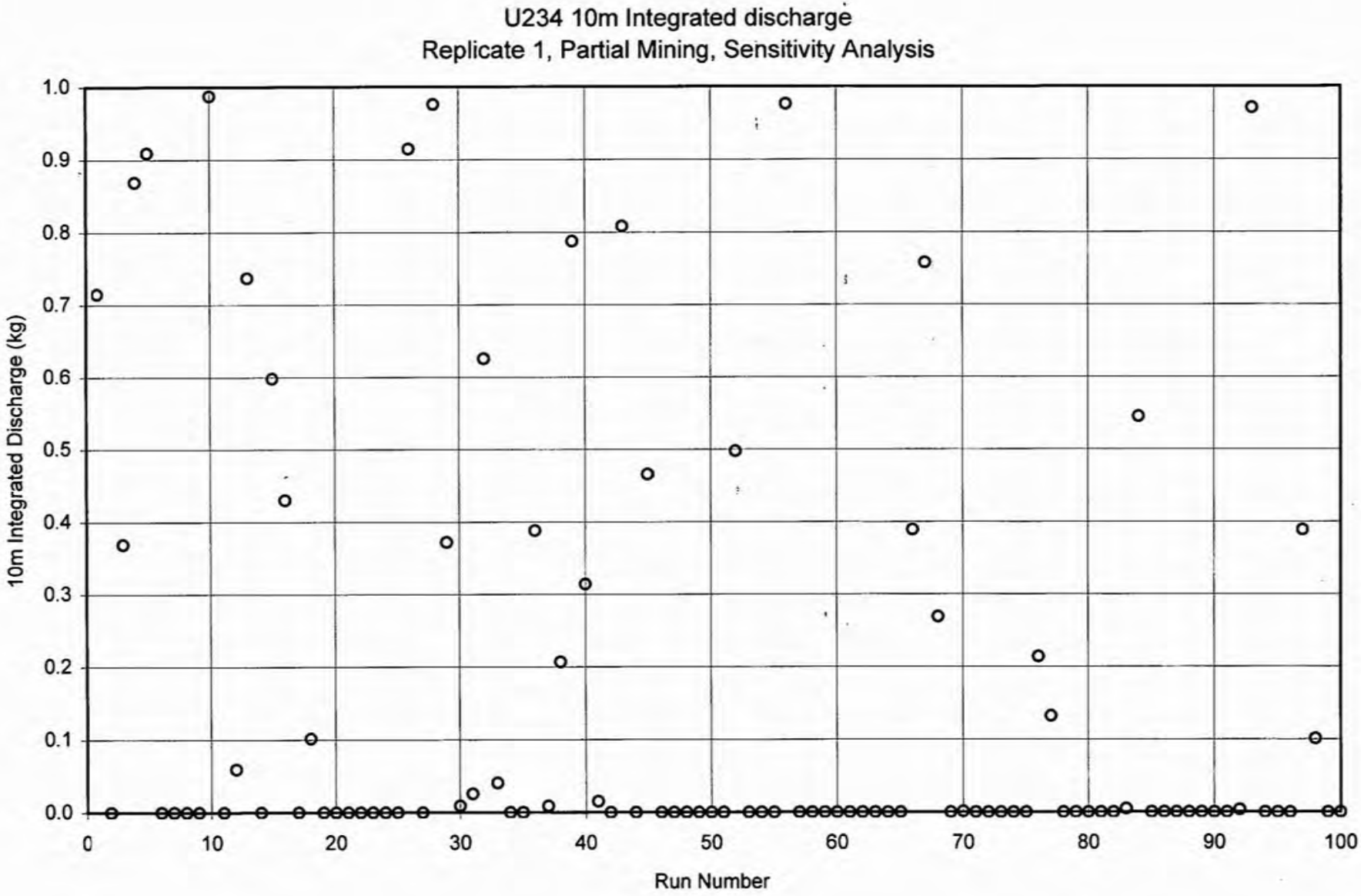

Information Only

Figure 7.29 Integrated Discharge of U234 at the 10m Discharge Boundary in the Sensitivity Analyses

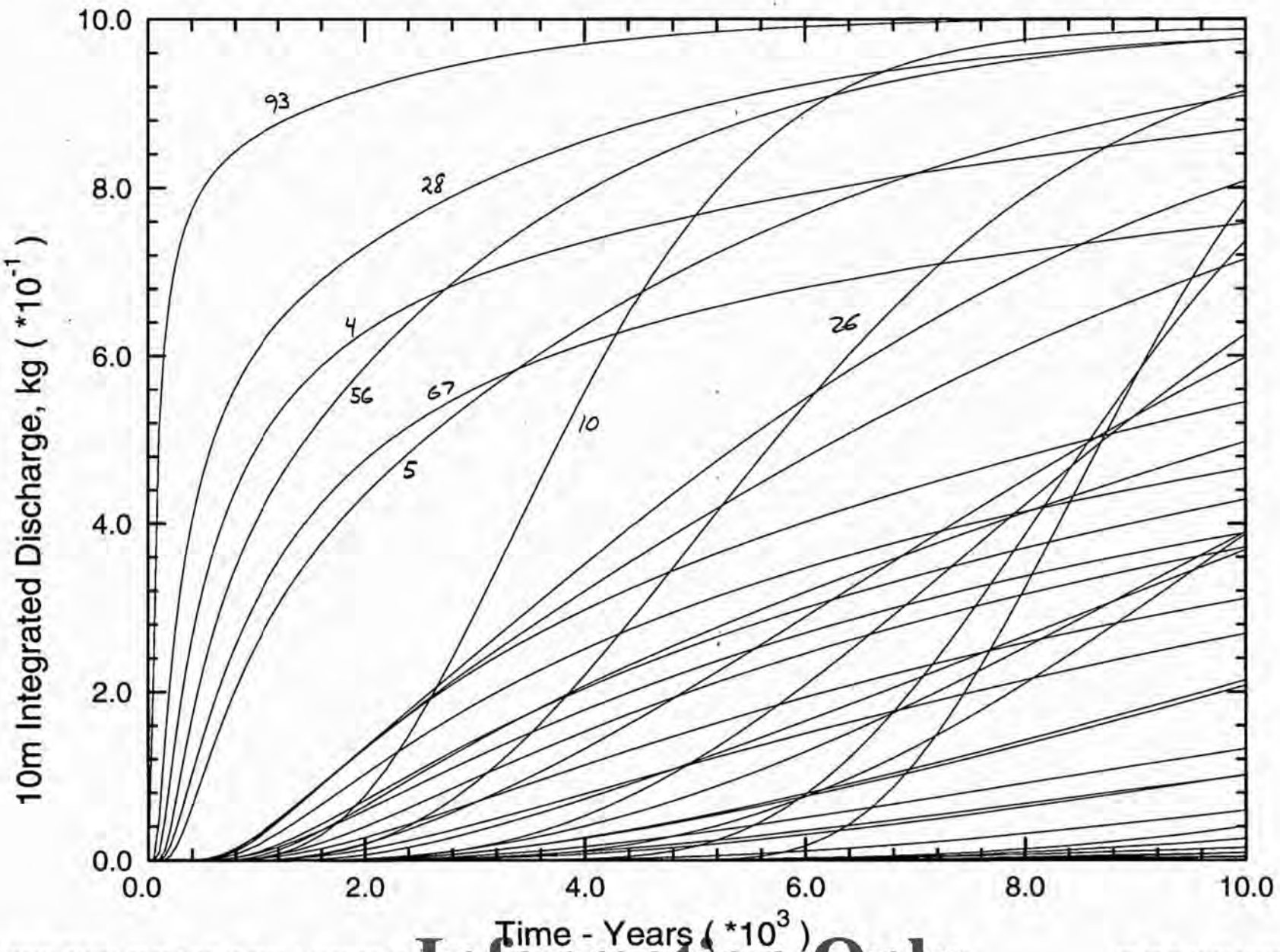

DISK$TINA_CCA3:[BF.MJSHORT.SECO]SPLAT_SECO_MT4U234C.INP;5 Information Only SPLAT_PA96_2 1.02 11/22/96 14:18:40

Figure 7.30 Concentration Contour Plot of ^{234}U at ~~10,000~~ 1,000 years in the Sensitivity Analysis.

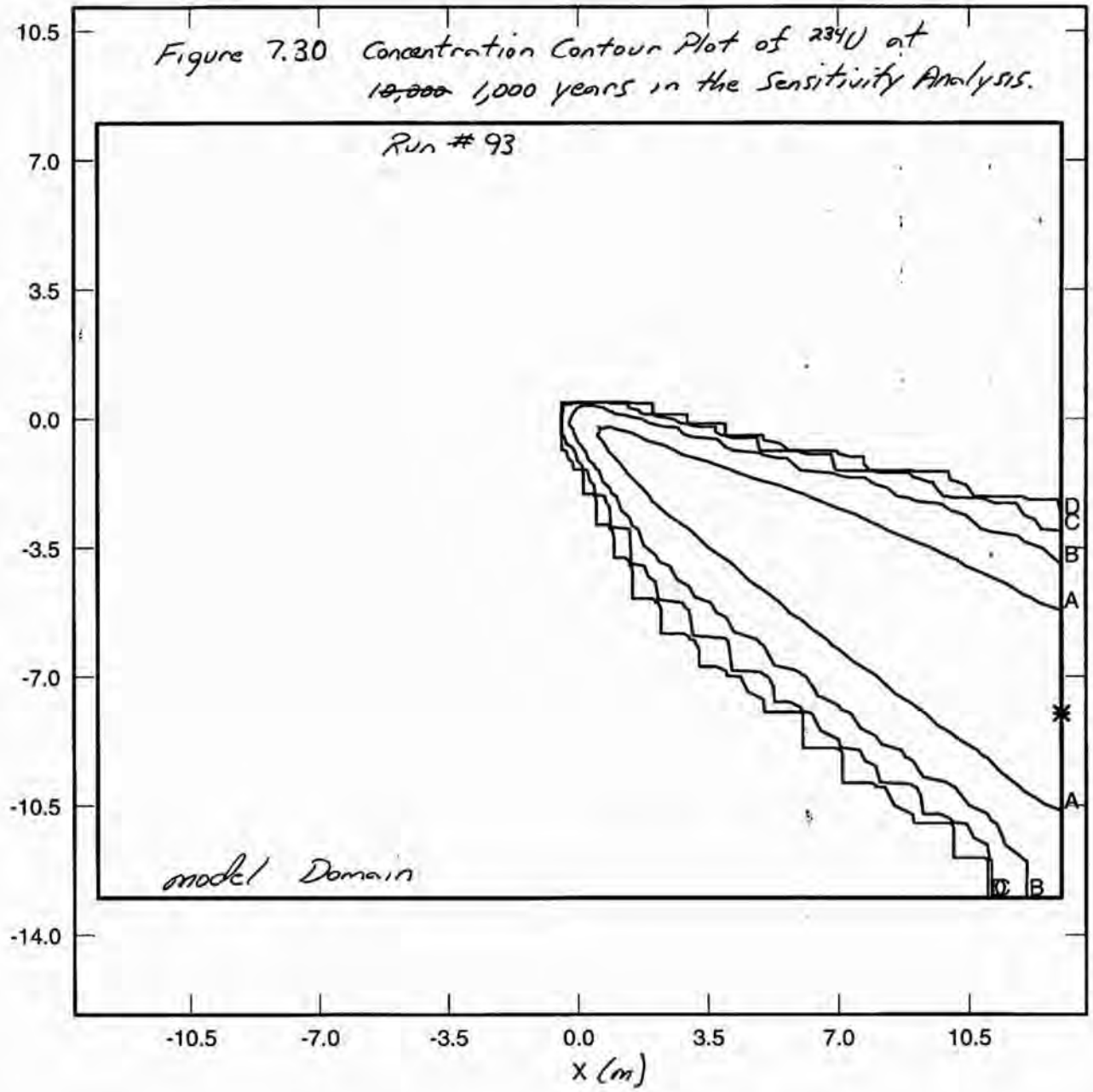

GM_PA96 6.08 08/26/96
RELATE_P 1.43 08/26/96
RELATE_P 1.43 08/27/96
POSTSECO 1.02 09/02/96
ALGEBRAC 2.35 09/16/96
ALGEBRAC 2.35 09/16/96

NO Deformation

Element Blocks Active:
1 of 1

CONU234 (kg/m^3)

A = 10.00E-6
B = 1.00E-6
C = 0.10E-6
D = 0.01E-6

= 0.00E-6
* = 36.47E-6 maximum Concentration (kg/m^3)

Time = 1.000E+3 years

DISK$IKE_CCA3:[PANEL.JWGARNE.SECO]ST2D3_SAT_R1_V093_PM.CDB;1

BLOTCDB_PA96 1.37 10/02/96 14:23

Information Only

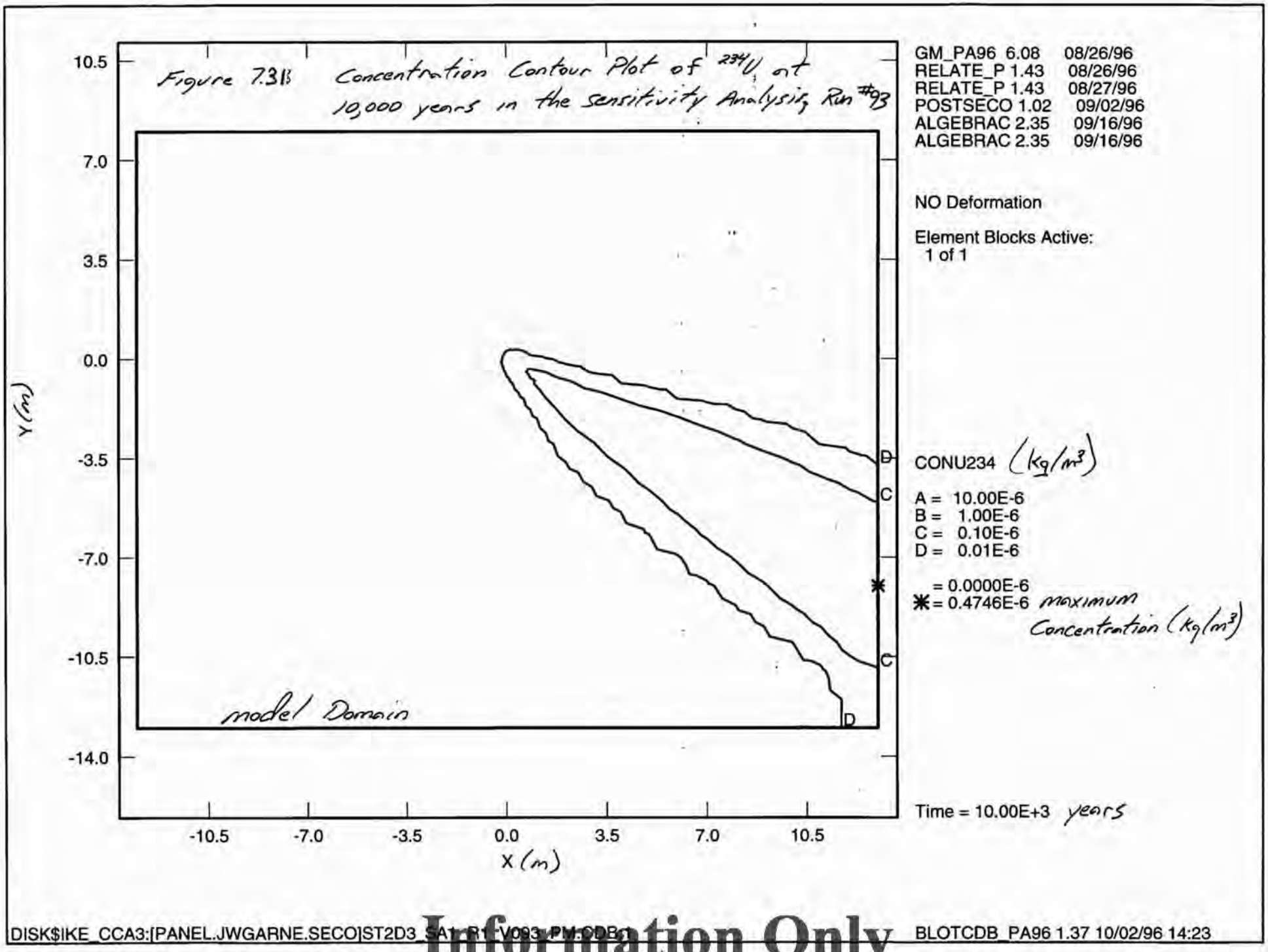

Information Only

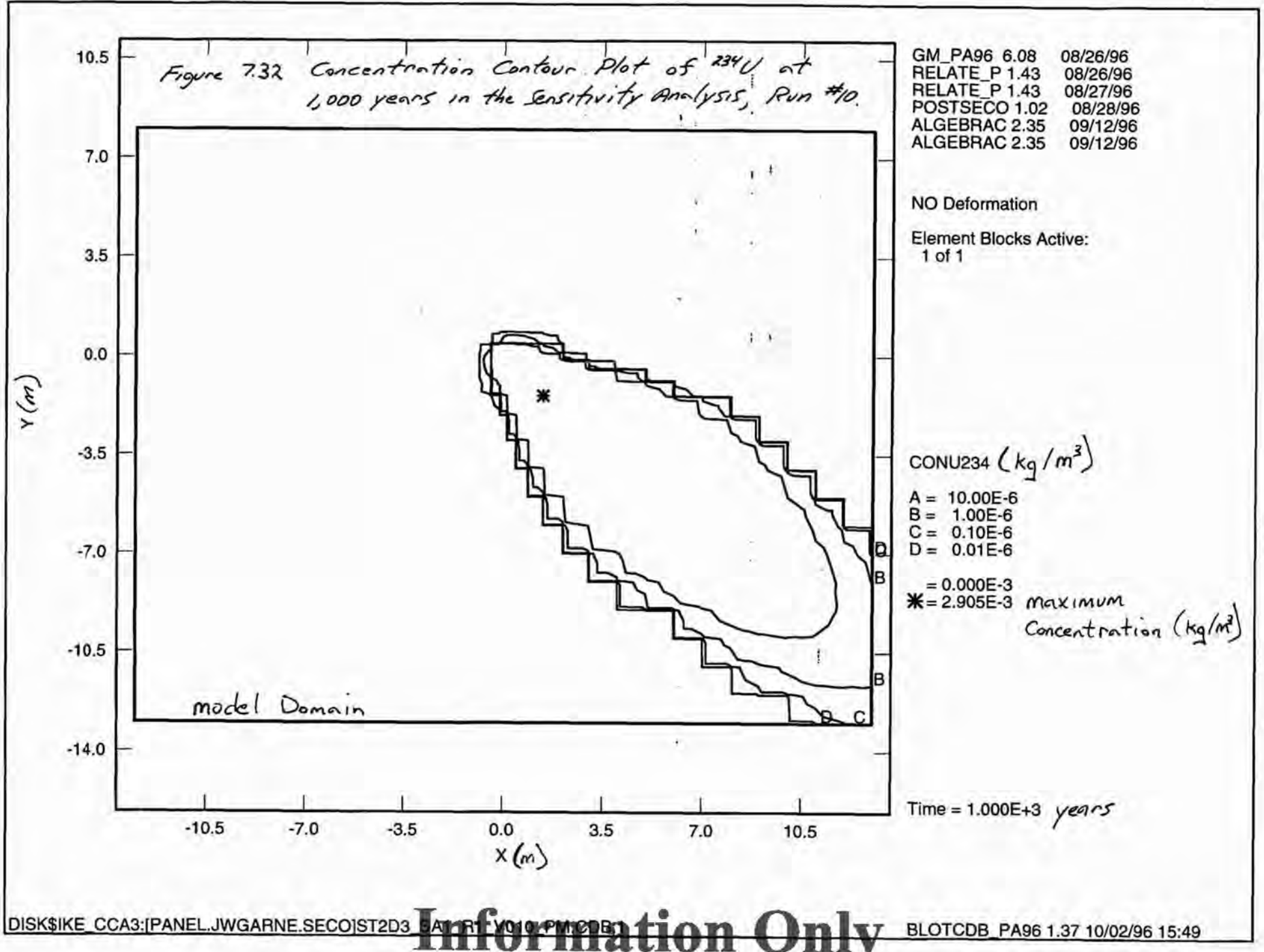

Information Only

7.3.2 Temporal Discretization

The proper selection of a time step size for a dual-porosity transport simulator is dependent on the characteristic response time of both the advective and diffusive continuums. In the advective continuum, the time step should be chosen such that the Courant number, Cr (dimensionless),

$$Cr = \frac{V\Delta t}{\phi \Delta \ell} \tag{7.1}$$

is less than unity (Huyakorn and Pinder, 1983, p. 206), where, V is the specific discharge ($m\ s^{-1}$), Δt the time step (s), ϕ the advective porosity (dimensionless), and $\Delta \ell$ is the spatial discretization.

During test simulations using SECOTP2D, it was found a reasonably converged solution was obtained in the diffusive continuum when the dimensionless time step, ΔT, was less than 10^{-2}. ΔT is defined as,

$$\Delta T = \frac{D' \Delta t}{B^2 R'} \tag{7.2}$$

where, D′ is the effective matrix diffusion coefficient, B is the matrix block half length, and R′ is the matrix retardation coefficient (see Section 2.2 for additional discussion of these parameters). From Eq. 7.2 it is clear the maximum time step, Δt, required to resolve transport in the diffusive continuum is proportional to $B^2 R' / D'$. Therefore, as B approaches zero, the time step required to solve the diffusion equation approaches zero as well. Fortunately, the parameter distributions for B and R are sufficiently large that the diffusive continuum time step criteria was seldomly violated.

The same cannot be said however, for the time step criteria recommended for the advective continuum. Ideally, a time step would have been chosen such that the $Cr < 1$ for each element in the entire flow domain. Such an evaluation has been performed for a few runs with the conclusion being hundreds of thousands to millions of timesteps are needed to resolve transport through the advective continuum at each point in the problem domain. On the other hand, isotope plumes generally remained near the point of injection so it was not necessary resolve transport throughout the problem domain. Groundwater flow velocities are generally much lower inside the waste panel area than at many locations outside the waste panel area. Consequently, a much larger time step can be used to resolve isotope transport when the plume remains predominately in the waste panel area.

To examine temporal convergence within the waste panel area, the Courant number was computed at the grid block containing the isotope source. This location is assumed to be representative of the Courant number in the waste panel area, though it is acknowledged the magnitude of the flow field varies somewhat within this region. Courant numbers computed at the source using a Δt of 1.333 years are presented for the Replicate 1, full and partial mining

Information Only

scenario's in Figures 7.33 and 7.34, respectively. The data has been sorted in ascending order to demonstate that the Courant number is fairly large in approximately 10% of the runs, in both the full and partial mining scenario's.

Concern regarding those simulations in which the Courant number exceeds unity was addressed by re-running the ^{234}U(VI) isotope of replicate 1, Run #93, full mining, with 100,000 time steps (0.1 year time step, Cr < 1). Run #93 was selected because it has relatively low ^{234}U(VI) matrix distribution coefficient, and also a Cr ≈ 10 at the source. As expected, and shown in Figures 7.35 and 7.36, the CCA solution is not as converged in time as one would hope. The 100,000 time step solution shows some degree of enhanced transport, however, the solution is still nowhere near the land withdrawal boundary. A similar analysis, except with one million time steps was performed with replicate 1, vector 1, full mining. Run #1 also has favorable transport parameters, but a Cr ≈ 1 at the source. As shown in Figures 7.37 and 7.38, the CCA solution and the million time step solution are quite similar.

One can conclude from this exercise that when the courant number at the source is less than or equal to one and the isotope plume remains in the waste panel area, the solution is converged in time. When the source point courant number exceeds one, the solution is potentially not converged. However, for plumes contained within or near the waste panel area, the temporal discretization error, in terms of transport distance, is shown to be small relative to the travel distance to the land withdrawal boundary. Therefore, when the isotope plume is contained within or near the waste panel area, the temporal discretization error is thought to be acceptably small such that the solution can be considered adequate to demonstrate zero discharge at the land withdrawal boundary.

For those runs in which transport distances were large, it was necessary to re-run the simulation with smaller time steps. Run #33 of replicate 3 was the only simulation possessing significant transport away from the source. Both the full and partial mining scenario's were re-run in CMS with 100,000 time steps. Due to instabilities along the southern boundary of the full mining run, it was necessary to run the simulation again with 400,000 time steps. The 400,000 time step simulation was not included in the CCDF construction, however, the integrated discharge of the 100,000 time step simulation (which was used in the CCDF construction) is essentially identical to the integrated discharge computed in the 400,000 time step simulation. Therefore, it can be concluded the instability did not affect the primary deliverable, isotope integrated discharge.

Information Only

Figure 7.33

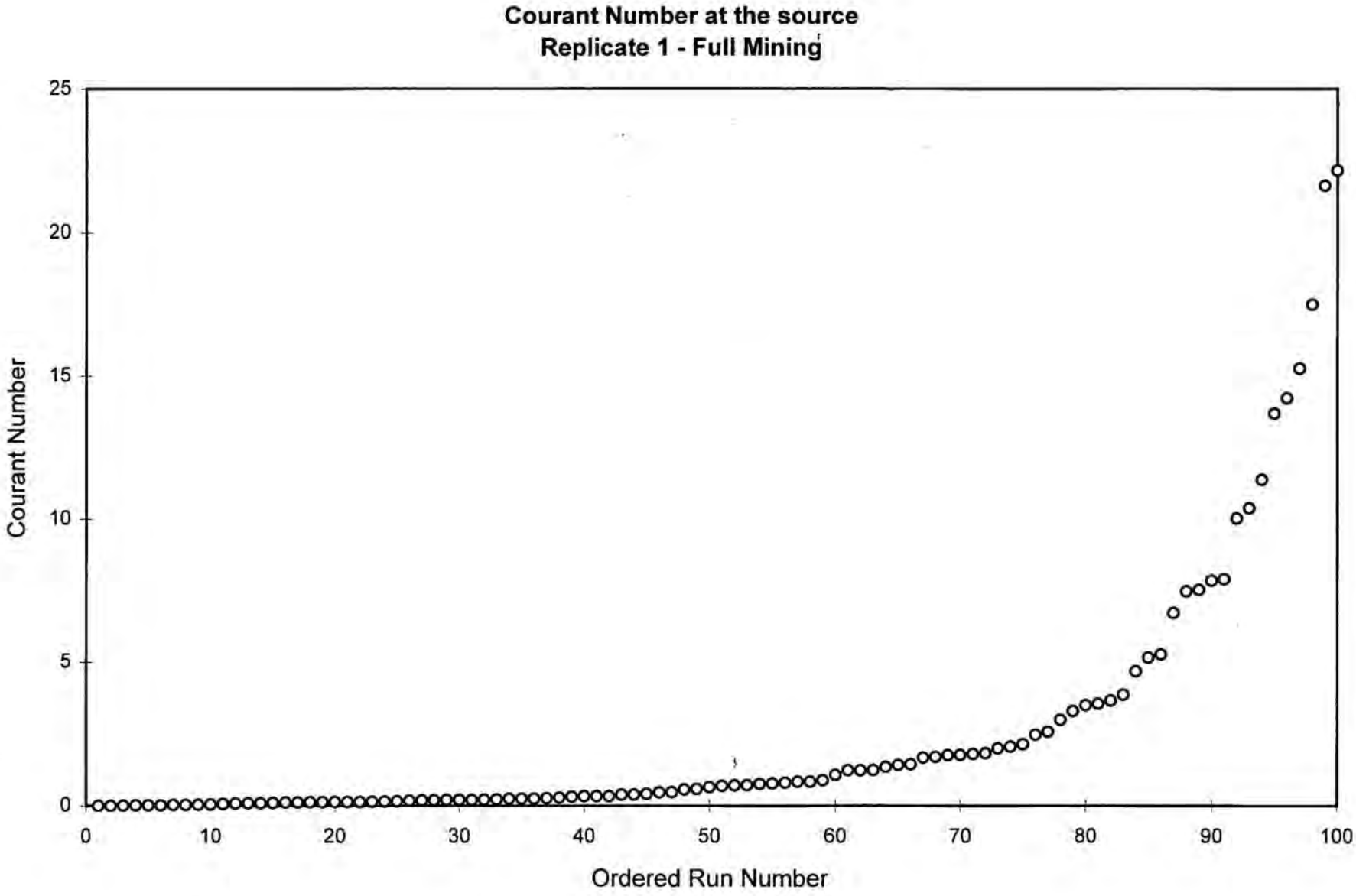

Information Only

Figure 7.34

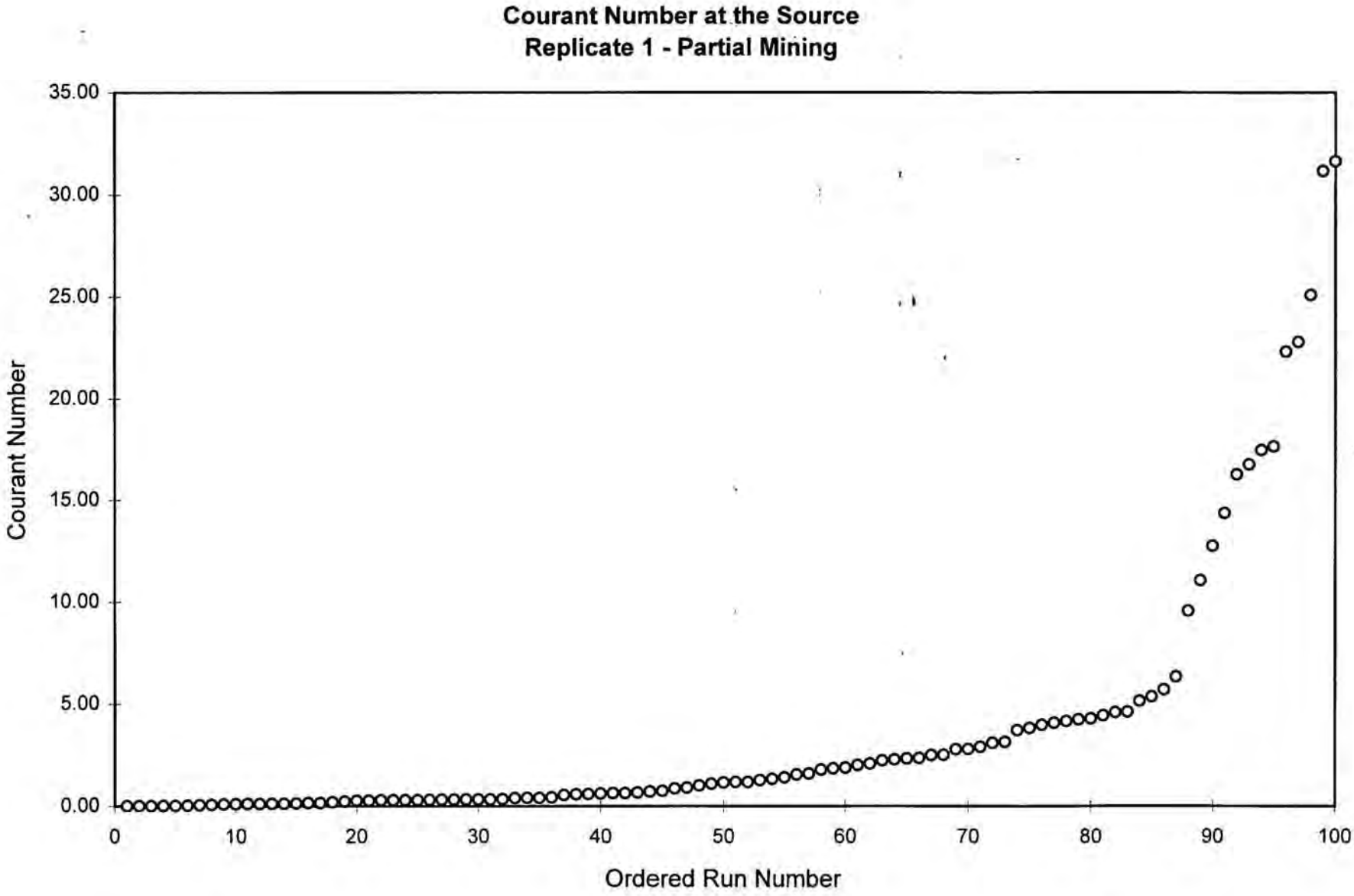

Information Only

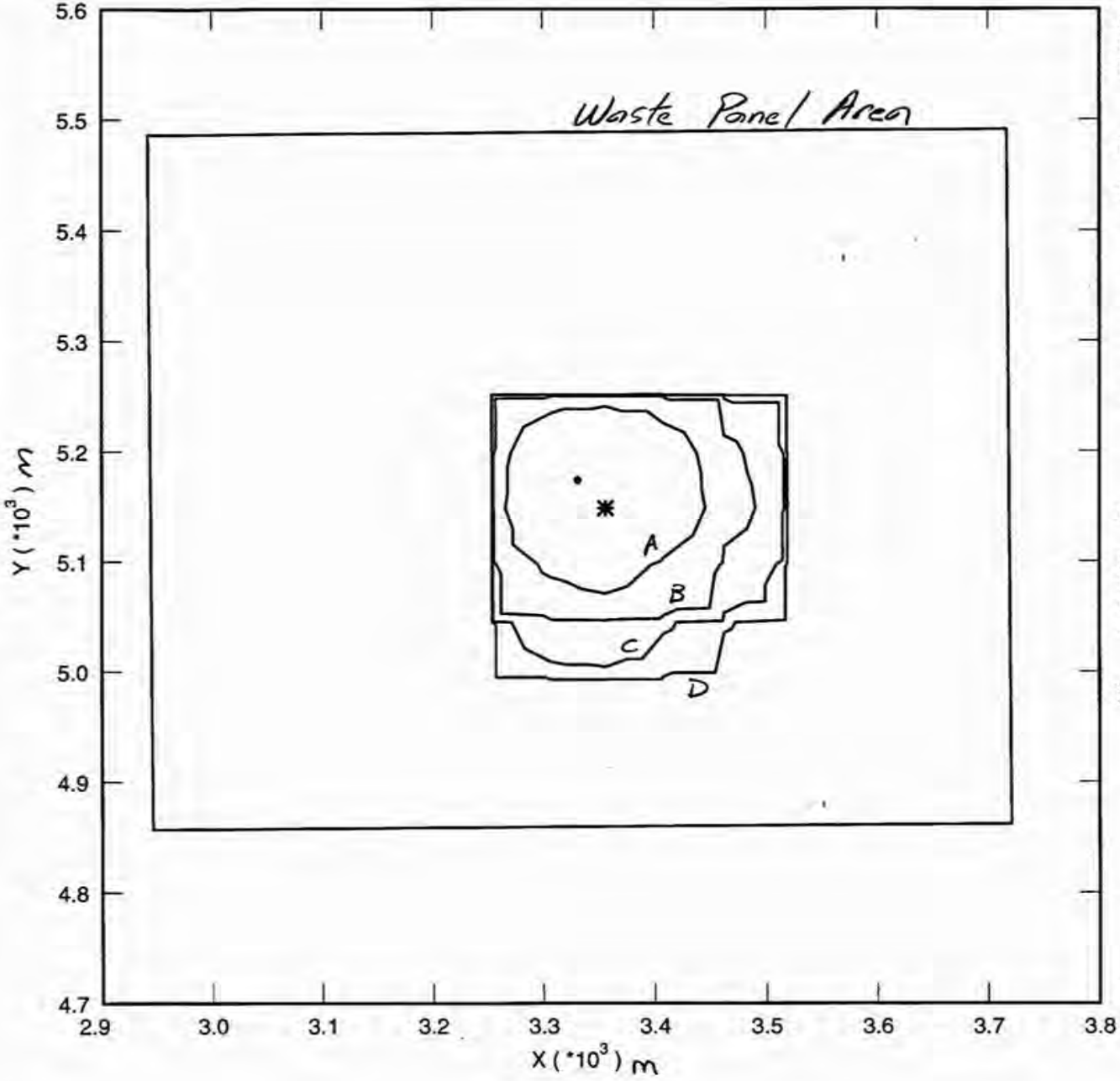

GM_PA96 6.08 06/16/96
RELATE_P 1.43 06/16/96
POSTSECO 1.02 06/18/96

NO Deformation

Element Blocks Active:
1 of 1

Figure 7.35
^{234}U concentration contour plot for Replicate 1, Run #93 with 7,500 time steps.

CONU234 (kg/m^3)

A = 0.1000E-6
B = 10.00E-9
C = 1.000E-9
D = 0.1000E-9

= 0.0000E-6
✱ = 0.6904E-6

Time = 10.00E+3 years

U1:[JLRAMSE.CCA.ST2D.R1]ST2D3_CCA_R1_V093_FM.CDB;1

BLOTCDB_PA96 1.37 06/26/96 15:42

Information Only

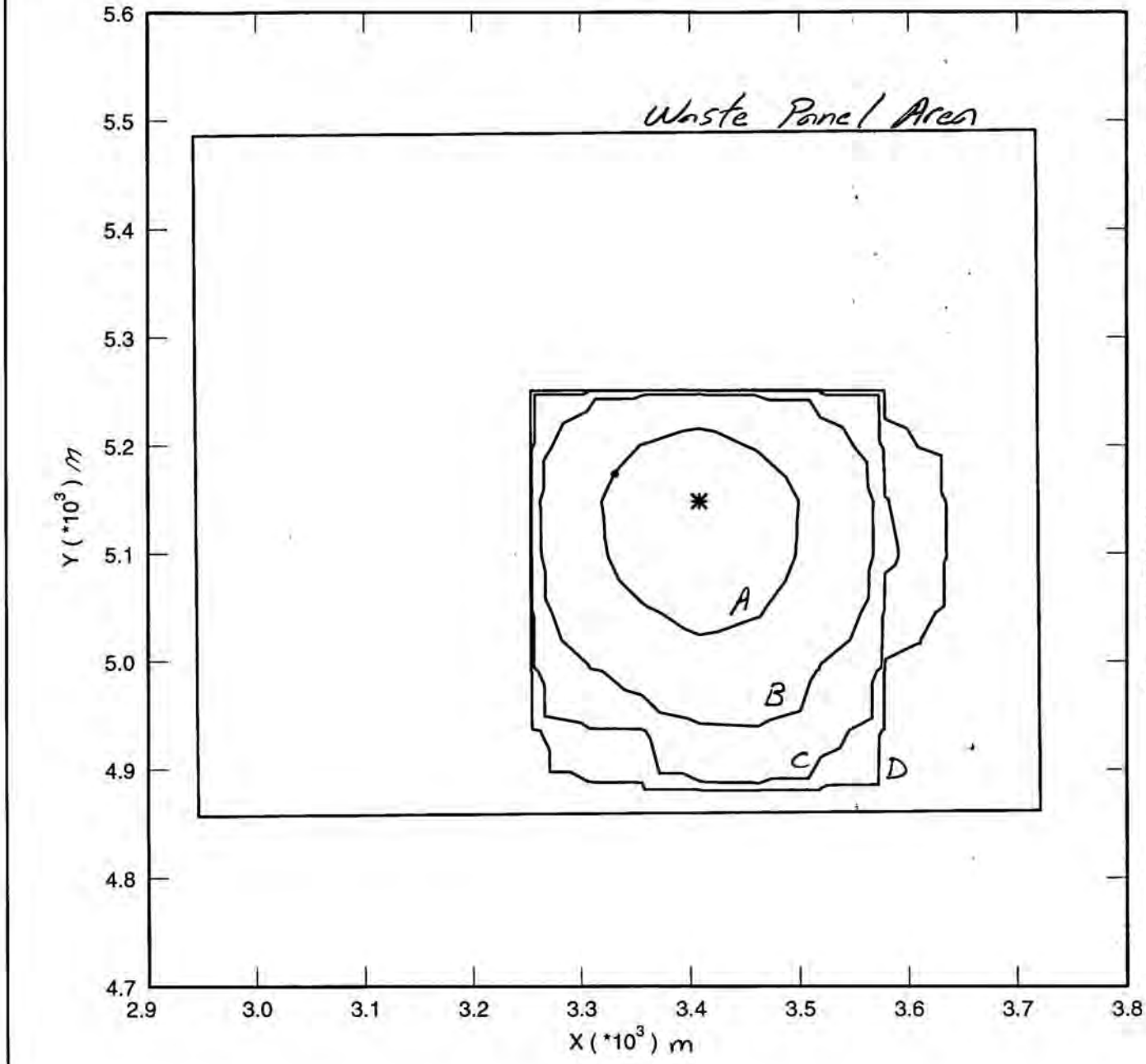

GM_PA96 6.08 06/16/96
RELATE_P 1.43 06/16/96
POSTSECO 1.02 06/26/96

NO Deformation

Element Blocks Active:
1 of 1

Figure 7.36
^{234}U concentration contour plot for Replicate 1, Run #93 with 100,000 time steps.

CONU234 (kg/m^3)

A = 0.1000E-6
B = 10.00E-9
C = 1.000E-9
D = 0.1000E-9

= 0.0000E-6
* = 0.3050E-6

Time = 10.00E+3 years

N1:[NOBACK.JLRAMSE.CCA.ST2D.R1FM]TEST_R1_V998_FM.CDB01

BLOTCDB_PA96 1.37 06/26/96 15:41

Information Only

51

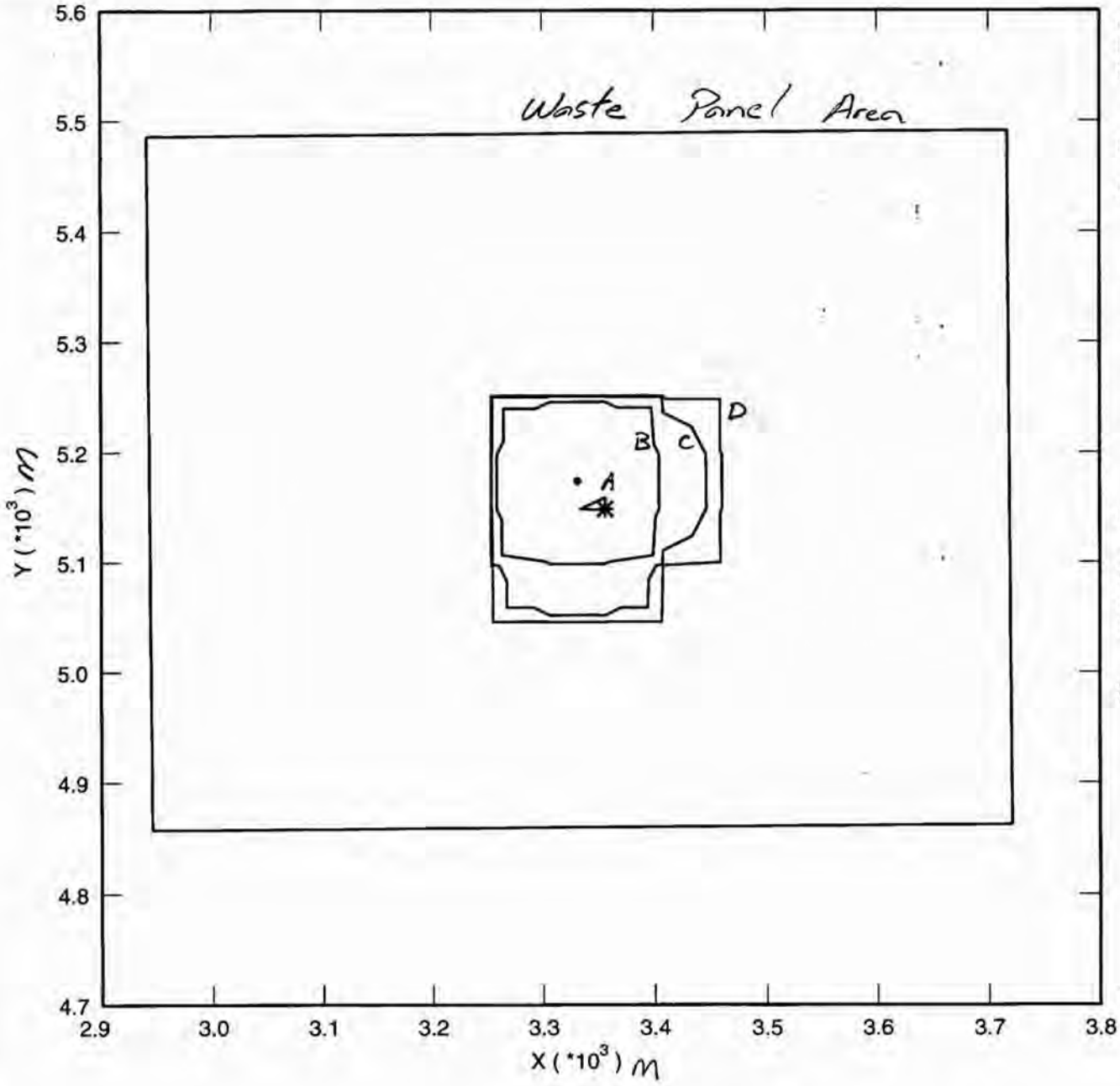

GM_PA96 6.08 06/16/96
RELATE_P 1.43 06/16/96
POSTSECO 1.02 06/16/96

NO Deformation

Element Blocks Active:
1 of 1

Figure 7.3.7
^{234}U Concentration contour plot for Replicate 1, Run 1, with 7,500 time steps

CONU234 (kg/m^3)

A = 1.000E-6
B = 0.100E-6
C = 0.010E-6
D = 0.001E-6

= 0.000E-6
✱ = 1.015E-6

Time = 315.6E+9 seconds
= 10,000 years

U1:[JLRAMSE.CCA.ST2D.R1]ST2D3_CCA_R1_V001_FM.CDB;1

BLOTCDB_PA96 1.37 06/26/96 14:07

Information Only

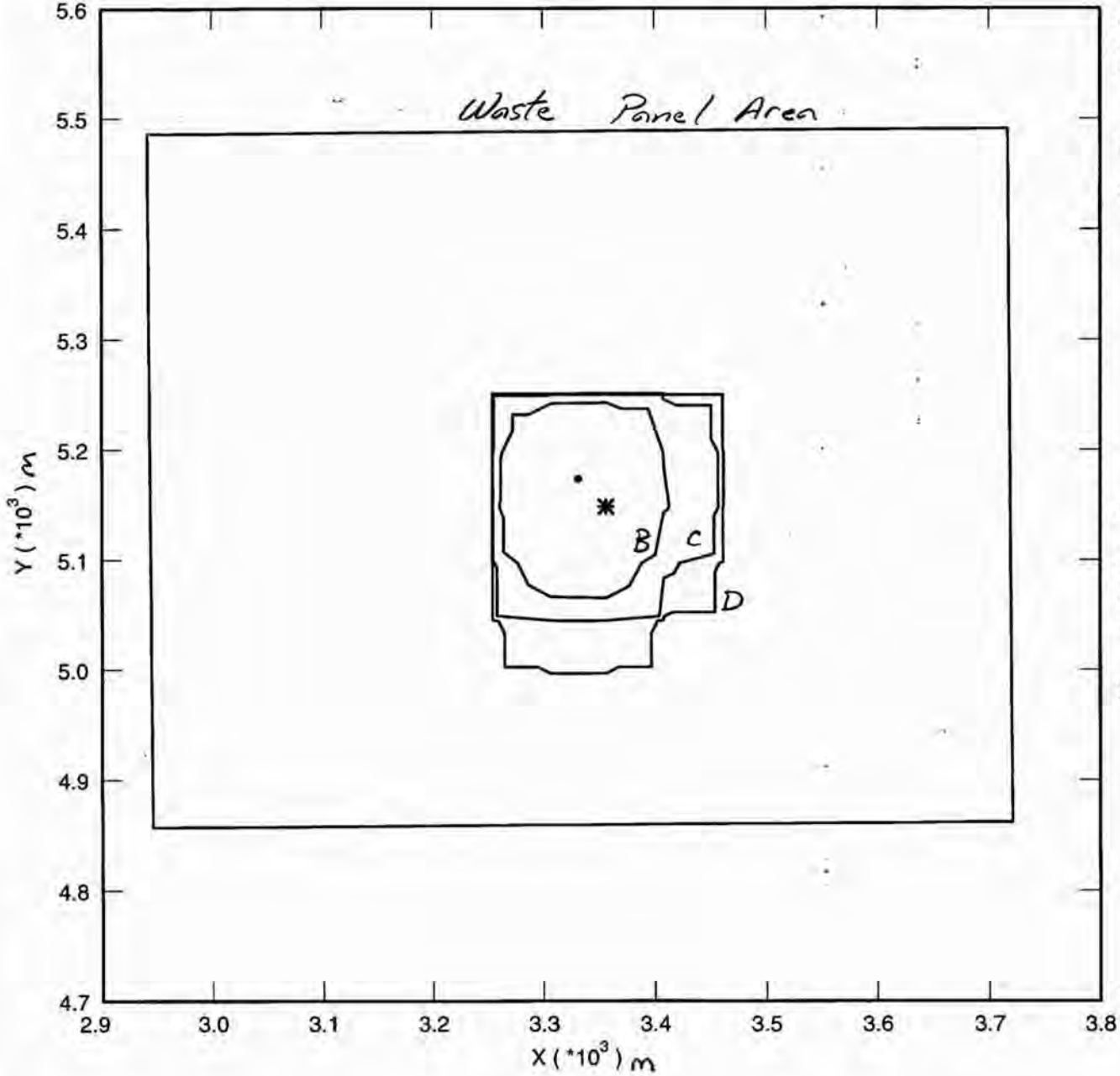

GM_PA96 6.08 06/16/96
RELATE_P 1.43 06/16/96
POSTSECO 1.02 06/23/96

NO Deformation

Element Blocks Active:
1 of 1

Figure 7.38
^{234}U Concentration Contour plot for Replicate 1, Run 1 with 1,000,000 Time Steps.

CONU234 (kg/m^3)

A = 1.000E-6
B = 0.100E-6
C = 0.010E-6
D = 0.001E-6

= 0.0000E-6
✱ = 0.8842E-6

Time = 10.00E+3 years

N1:[NOBACK.JLRAMSE.CCA.ST2D.R1FM]TEST_R1_V001_FM.CDB;1

BLOTCDB_PA96 1.37 06/26/96 14:26

Information Only

8.0 References

Bertram, S. G., 1996. Record of FEP screening work FEP ID# NS-4A, Pumping from the Culebra within the controlled area, WPO 30755, Sandia WIPP Central Files (SWCF).

Blaine, R.L., 1996. Error in PRESECOTP2D and impact on CCA calculation - Corrected, WPO WPO 42334, Sandia WIPP Central Files (SWCF).

Brush, L.H., 1996. Ranges and probability distributions of K_ds for dissolved Pu, Am, U, Th, and Np in the Culebra for the PA calculations to support the WIPP CCA, WPO 38801, Sandia WIPP Central Files (SWCF).

Brush, L.H., and L.J. Storz, 1996. Revised ranges and probability distributions of K_ds for dissolved Pu, Am, U, Th, and Np in the Culebra for the PA calculations to support the WIPP CCA, WPO 38231, Sandia WIPP Central Files (SWCF).

Corbet, T., 1996. FEP NS-9, two-dimensional assumption for Culebra calculations, WPO 30802, Sandia WIPP Central Files (SWCF).

Corbet, T., and P. Swift, 1996. Parameters required for SECOFL2D: Climate Index, WPO 36425, Sandia WIPP Central Files (SWCF).

Fewell, M.E., 1996. Analysis plan for the performance assessment analyses supporting the compliance application, AP-AAD, WPO 36335, Sandia WIPP Central Files (SWCF).

Garner, J.W., 1996. Radioisotopes to be used in the 1996 CCA calculations, WPO 35202, Sandia WIPP Central Files (SWCF).

Helton, J.C., and J.D. Johnson, 1996. Design document for CCDFGF and GRIDFLO, WPO 31235, Sandia WIPP Central Files (SWCF).

Holt, R.M., and D.W. Powers, 1988. Facies variability and post-depositional alteration within the Rustler Formation in the vicinity of the Waste Isolation Pilot Plant, Southeastern New Mexico. DOE/WIPP 88-004. U.S. Department of Energy, Carlsbad, NM.

Hunter, R.L. 1985. A regional water balance for the waste isolation pilot plant (WIPP) site and surrouding area. SAND84-2233. Sandia National Laboratories, Albuquerque, NM.

Huyakorn, P.S., and G.F. Pinder, 1983. Computation methods in subsurface flow, Academic Press Inc., New York, NY.

Lavenue, M.S., 1996. Analysis of the generation of transmissivity fields for the Culebra Dolomite, AP-018, WPO 40517, Sandia WIPP Central Files (SWCF).

Information Only

McCord, J., 1996. Longitudinal dispersivity for the Culebra dolomite, WPO 37230, Sandia WIPP Central Files (SWCF).

Meigs, L., and McCord J., 1996. Physical Transport in the Culebra Dolomite, WPO 39167, Sandia WIPP Central Files (SWCF).

Papenguth, H.W., 1996. Parameter record package for colloid actinide retardation parameters, WPO 38173, Sandia WIPP Central Files (SWCF).

Perkins, W.G., 1996. Calculation of filtration for microbial and mineral fragment colloids, WPO 38250, Sandia WIPP Central Files (SWCF).

Pinder, G.F., Gray, W.G., 1977. Finite element simulation in surface and subsurface hydrology. Academic Press, New York.

Roache, P.J., R.L. Blaine, and B.L. Baker, 1996. SECOFL2D User's Manual Version 3.03, WPO 37271, Sandia WIPP Central Files (SWCF).

Ramsey, J.L., 1996. Analysis plan for the Culebra flow and transport calculations (Task 3) of the performance assessment analyses supporting the compliance certification application, AP-019, WPO 37267, Sandia WIPP Central Files (SWCF).

Robinson, T.W., and W.B. Lang, 1938. Geology and ground-water conditions of the Pecos River Valley in the vicinity of Laguna Grande de la Sal, New Mexico, with special reference to the salt content of the river water. Twelfth and thirteenth biennial reports of the state engineer of New Mexico for the 23rd, 24th, 25th, and 26th fiscal years, July1, 1934 to July 30, 1938. State Engineer, Santa Fe, NM.

Ruskauff, G., 1996. Groundwater modeling analysis plan for the generation of transmissivity fields for the Culebra flow and transport calculations, AP-018, WPO 37256, Sandia WIPP Central Files (SWCF).

Salari, K., and R. Blaine, 1996. SECOTP2D user's manual, Version 1.30, WPO 36695, Sandia WIPP Central Files (SWCF).

Smith, L.N., J.D. Johnson, and J.C. Helton, 1996. Analysis package for the CCDF construction (Task 7) of the performance assessment analysis supporting the compliance certification application, WPO 40524, Sandia WIPP Central Files (SWCF).

Stockman, C.T., 1996. Treatment of colloids in Culebra transport. WPO 38797, Sandia WIPP Central Files (SWCF).

Information Only

Vaughn, P.V., 1996. Analysis Package for the Salado Flow Calculations (Task 1) of the Performance Assessment Analyses Supporting the Compliance Certification Application, WPO 40514, Sandia WIPP Central Files (SWCF).

Vine, J.D., 1963. Surface geology of the Nash Draw quadrangle, Eddy County, New Mexico. U.S. Geological Survey Bulletin, 1141-B.

Wallace, M.G., 1996a. Record of FEP screening work FEP ID# NS-5A, Pumping from the Culebra Outside of the Controlled AreaWPO 40831, Sandia WIPP Central Files (SWCF).

Wallace, M.G., 1996b. Record of FEP screening work FEP ID# NS-11, Subsidence Associated with Mining Inside or Outside of the Controlled Area, WPO 40816, Sandia WIPP Central Files (SWCF).

Wallace, M.G., 1996c. Grid Design Study for the 1996 CCA Culebra flow and transport calculations, WPO 41654, Sandia WIPP Central Files (SWCF), to be submitted.

Williamson M., K. Aragon, 1996. Traceability / Repodicibility of the PA96 calculation for the CCA, WPO 40313, Sandia WIPP Central Files (SWCF).

WIPP Performance Assessment Department, 1992. Preliminary performance assessment for the Waste Isolation Pilot Plant, Volume 4: Uncertainty and sensitivity analyses for 40 CFR 191, Subpart B. SAND92-0700/4, WPO 23599, Sandia WIPP Central Files (SWCF).

Information Only

Appendix A

Physical Transport in the Culebra Dolomite
Meigs and McCord (1996)

Information Only

Sandia National Laboratories

Albuquerque, New Mexico 87185-1324

date: July 11, 1996

to: file (SWCF-A Records Center, SWCF-A:WBS1.1.5.2.3:TD:QA: Non-Salado Tracer Test Interpretations, Interim Simulations, WPO#37450)

Lucy Meigs Jim McCord

from: Lucy Meigs and Jim McCord, MS - 1324

WPO # 39167

subject: Physical Transport in the Culebra Dolomite

Attached is a letter report that briefly describes the recent work that has been done to characterize the physical transport processes in the Culebra dolomite. It also describes the rationale for the physical transport parameters used for the SECOTP2D calculations in the performance assessment calculations. Additional detailed information on the interpretations of the tracer test data and additional detail on discussion in this memo will be contained (or referenced) in the record package into which this memo is being placed (WPO#37450).

Copy to:
Margaret Chu, MS 1335
Peter Davies, MS 1324
Al Lappin, MS 1324
Rick Beauheim, MS 1324
Tom Corbet, MS 1324
Hans Papenguth, MS 1341
Larry Brush, Ms1341
Jim Nowack, MS1320
George Perkins, MS1341
Bob Holt, MS1324

Information Only

Exceptional Service in the National Interest

Physical Transport in the Culebra Dolomite

by Lucy C. Meigs and James T. McCord

7/11/96

Information Only

Physical Transport in the Culebra Dolomite

The Culebra Dolomite Member of the Rustler Formation is being studied as a possible transport medium for radionuclides released from the WIPP repository by future inadvertent human intrusion. This letter report describes data collection and data analyses which led to our current conceptual model of physical transport in the Culebra. It also covers how the conceptual model is implemented in the performance assessment (PA) of the WIPP site, and parameterization of the PA numerical models of physical transport in the Culebra.

Characterization of the Culebra for Development and Testing of Conceptual Models

In order to determine the important processes (advection, dispersion and diffusion) controlling contaminant transport and to evaluate the physical transport properties of the Culebra dolomite, a series of tracer tests has been conducted. Among the most important issues is whether the Culebra should be modeled as a single-porosity medium with transport only in the fractures or whether there may be significant interaction with the "matrix" (double-porosity medium). Convergent-flow tracer tests were conducted within the Culebra at three locations (H-3, H-6, and H-11 hydropads) between 1981 and 1988. These tests showed rates and amounts of solute transport to be strongly dependent on flow direction, and suggested that a physical retardation mechanism was affecting transport. The tracer-breakthrough curves from these tests were simulated using a homogeneous double-porosity continuum model (SWIFT II). These simulations showed that the observed transport behavior could be explained by a combination of anisotropy in horizontal hydraulic conductivity and matrix diffusion. These tests ruled out conceptualizing the Culebra as a homogeneous single-porosity medium (Jones et al., 1992). However, significant questions remained as to whether other processes such as heterogeneity in hydraulic conductivity could have caused the tailing in the breakthrough curves that was attributed to matrix diffusion.

Additional tracer tests have recently been conducted at the H-11 and H-19 hydropads. These tests included single-well injection-withdrawal tests and multiwell convergent-flow tests at both locations. The results of a preliminary tracer test conducted May-July 1995 at the H-19 hydropad revealed that at this site, transport was slower than at previous sites tested. The relatively high advective porosity (greater than 0.05, larger than typical fracture porosities) that appears to be required to model these data caused us to question our previous conceptualization of the Culebra. Through careful reexamination of the geology and stratigraphy of the Culebra, we have developed a clearer picture of the important processes that control transport.

The Culebra has non-uniform properties both horizontally and vertically. This has been demonstrated with both hydraulic and tracer tests. The upper portion of the Culebra has a much lower permeability and does not appear to provide pathways for rapid transport (see effective thickness discussion below). Examination of core and shaft exposures has

Information Only

b

revealed that there are multiple scales of porosity within the Culebra including: fractures ranging from microscale to potentially large, vuggy zones, and interparticle and intercrystalline porosity (Figure 1). Flow occurs within fractures, within vugs where they are connected by fractures, and probably to some extent within interparticle porosity where the porosity is high, such as "chalky" lenses. At any given location, flow will occur in response to hydraulic gradients in all places that are permeable. The variation in peak arrival time in tracer breakthrough curves between the H-11 and the H-19 hydropads suggests that the types of porosity contributing to rapid advective transport vary spatially. In addition to advective transport of solutes, diffusive transport will occur into all connected porosity. Thus, diffusion can be an important process for effectively retarding solutes by transferring mass from the porosity where advection (flow) is the dominant process into other portions of the rock. Diffusion into stagnant portions of the rock also provides access to additional surface area for sorption. When the permeability contrast between different scales of connected porosity is large, transport can effectively be modeled by dividing the system into advective porosity (often referred to as fracture porosity) and diffusive porosity (often referred to as matrix porosity).

The interpretations of tracer test data to date have relied on both homogeneous and heterogeneous single- and double-porosity continuum models (SWIFT II and THEMM). Spatial variations in advective transport are represented in numerical simulations of the tracer tests with random fields of hydraulic conductivity. Interpretations completed thus far have shown that the single-well injection-withdrawal test data from both the H-11 and H-19 hydropads cannot be explained by heterogeneity alone. Simulations of cumulative mass recovery during the withdrawal phase of the single-well tests with both homogeneous and heterogeneous models suggest that mass recovery should be very rapid for single-porosity media. The Culebra tracer test data, however, show a much slower cumulative mass recovery, as would be anticipated if some sort of diffusional process was controlling mass recovery (i.e. if matrix diffusion is playing a significant role).

In summary, the major physical transport processes that affect actinide transport through the Culebra dolomite include advection (through fractures and other permeable porosity), dispersive spreading during advection due to heterogeneity, and matrix diffusion (between fractures and matrix or more generally, diffusion between adjacent regions with large permeability contrasts). Sorption also exerts an important control on transport, however this memorandum focuses on physical transport rather than chemical transport.

PA Modeling of Physical Transport in the Culebra

At the Performance Assessment (PA) scale, spatial variability in advective transport is represented by heterogeneous transmissivity fields that have been conditioned on available point transmissivity data and transient pressure data. In the PA calculations, the lower permeability of the upper portion of the Culebra has been approximated by eliminating this portion of the Culebra from the transport model. The possible spatial variability in transport properties (diffusion and sorption rates) has not been taken into

Information Only

7

Figure 1. Multiple scales of Culebra porosity based on examination of core, shaft mapping and RaaX logging (Holt, 1996).

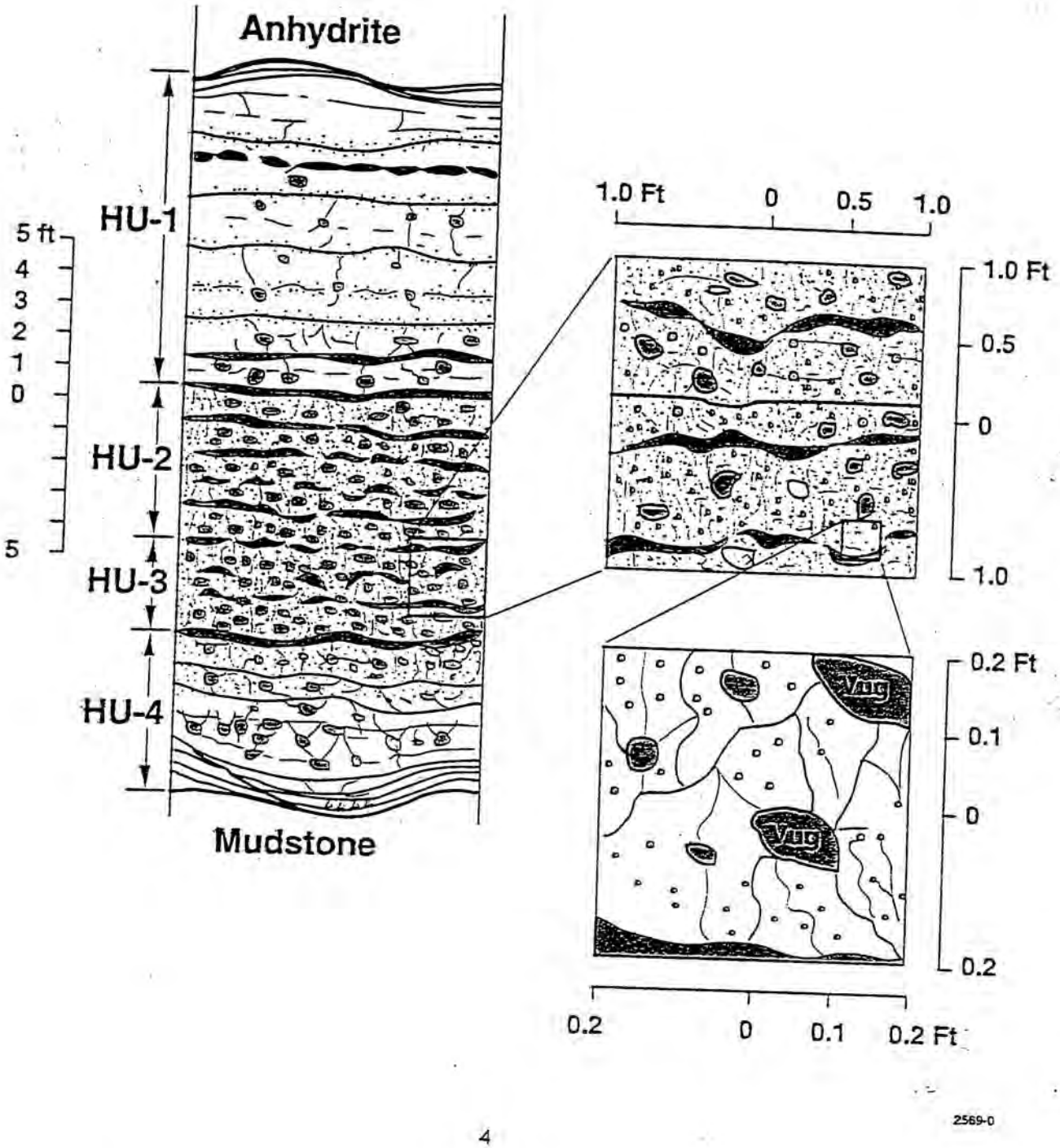

Information Only

account in the PA model. Attempts have been made to take into account the variability by limiting the parameter ranges to the expected effective spatial averages across the site and, when unquantified uncertainties exist, by providing conservative estimates of transport parameters (i.e. parameters that could lead to greater releases than expected). For instance, with respect to effective Culebra thickness (see next section), field data indicate that only the lower 4± m actively participates in flow at most locations sampled. Despite the fact that our rather sparse sampling network prevents us from ruling out the existence of regions where the entire 7 m of Culebra is active in the physical transport process, we have conservatively specified that PA calculations should consider the Culebra to be only 4 m thick everywhere.

The PA for WIPP models transport in the Culebra with SECOTP2D which is a double-porosity model. The physical transport parameters required by SECOTP2D are: (1) effective thickness (See parameter records package in the Sandia WIPP Central Files (SWCF-A), WPO#37223), (2) advective porosity (often referred to as fracture porosity) (WPO#37227), (3) diffusional porosity (often referred to as matrix porosity) (WPO#37228), (4) half matrix block length (defined as one-half the thickness of a matrix slab between two parallel plate fractures) which represents specific surface area to volume ratio for matrix diffusion (WPO#37225), (5) diffusive (or matrix) tortuosity (WPO#37226), and (6) dispersivity (WPO#s 37230 and 37231). Effective thickness, diffusive porosity, and diffusive tortuosity were all specified based on field or laboratory measurements. Half matrix block length and advective porosity were specified based on the interpretation of tracer test data from the H-3, H-11 and H-19 hydropads (Hydro Geo Chem, Inc., 1985; Stensrud et al., 1990, Beauheim et al., 1995). Dispersivity values were developed based on comparison of values inferred from tracers tests to large-scale values expected due to heterogeneity at the PA scale. A description of the rationale for the distribution of each of these parameters is provided below.

Effective Thickness

The effective thickness used for the SECOTP2D calculations is 4.0 m. This effective thickness represents the median Culebra total thickness within the land withdrawal boundary (LWB) (7 m) minus the median (and mean) thickness of Unit 1 (upper Culebra) within the LWB (3 m) as defined by Holt (1996). There is considerable information that indicates that there are significant vertical stratigraphic variations in the Culebra (Holt and Powers, 1984, 1986, 1988, 1990). Based on the descriptions of numerous cores it can be concluded that the basic stratigraphy of the Culebra dolomite is continuous across the land withdrawal boundary area (Holt, 1996; Holt and Powers 1988). Recent hydraulic tests at the H-19 hydropad (Kloska et al., 1995) have indicated that the permeability of the upper portion of the Culebra is significantly lower than the permeability of the lower Culebra at this hydropad. Hydrophysical (fluid) logging also suggest that most of the flow is coming from the lower portion of the Culebra at H-19 (Results of COLOG work, WPO# 38402). Tracer tests have confirmed that at the H-19 hydropad the upper portion of the Culebra does not play a significant role in solute transport. Tracers injected into

Information Only

the upper Culebra at H-19b3, H-19b5, H-19b7 only showed up at the pumping well (H-19b0) at barely detectable levels, whereas tracers injected into the lower Culebra or the full Culebra at these wells showed up at the pumping well in significant concentrations (Beauheim et al., 1995; and H-19 tracer test data (WPO# 37452)). In descriptions of the Culebra dolomite in the Air Intake Shaft, Holt and Powers (1990) noted that most of the fluid observed to come out of the Culebra came from the lower portion of the Culebra. Mercer and Orr (1979) report the results of a tracer (^{131}I) and temperature survey run at the H-3 hydropad which indicated that, within the resolution of the test, 100 percent of the flow out was in the lower approximately 10 ft of the Culebra. This test thus suggests that at H-3 the upper 14 ft of Culebra has a very low permeability. Hydraulic testing at well H-14 found that at this location the permeability of both the upper and the lower Culebra was quite low. At H-14 the permeability of the upper Culebra is slightly higher than the permeability of the lower Culebra (Beauheim, 1987). In summary, the bulk of the data points to the fact that in many locations the majority of the flow and transport appears to be taking place in the lower portion of the Culebra, i.e. excluding hydrostratigraphic unit 1. There may be locations where the entire Culebra participates in transport, but for lack of evidence along the off-site pathway, a thinner thickness has been selected. If additional evidence were to be collected that indicated that the entire Culebra thickness should be used in the PA model, the use of this larger thickness would result in slower transport and a decrease in releases.

Diffusive Porosity

The diffusive porosity distribution used for the SECOTP2D calculations is:

Minimum	0.10
10th Percentile	0.11
25th percentile	0.12
50th percentile	0.16
75th percentile	0.18
90th percentile	0.19
Maximum	0.25

This porosity distribution is derived from laboratory measurements. Boyle's Law helium porosity measurements have been made on 103 Culebra core plugs from 17 locations as reported in Kelley and Saulnier (1990), as well as additional porosity measurements recently completed by Terra Tek (WP0#38234). Water resaturation porosity measurements were also made for a subset of the cores. All measurements were very similar; the average difference between the water resaturation porosity and the Boyle's Law helium porosity was less than 0.005. The methodology used for these porosity measurements and the comparisons made are described in Kelley and Saulnier (1990). A spreadsheet in the diffusive porosity parameter records package (WPO#37228) summarizes all the Boyle's Law helium porosity data that have been collected. This spreadsheet summarizes the maximum, minimum, median and average for all data, data-averaged by well, and well averages averaged by hydropad, and all data averaged by

Information Only

hydropad. The hydropad averages of the data were used to develop the distribution presented above since the wells at an individual hydropad are very close together as compared to the spacing of all wells. As expected, averages from the hydropads give a narrower distribution than the distribution of all data. In the PA simulations (SECOTP2D), a single value of diffusive porosity is used across the entire model domain for a given realization. The value used for diffusive porosity clearly should be the effective average diffusive porosity encountered along the expected off-site pathway. Thus it does not make sense to include the extreme individual data values in the distribution for use by PA.

Diffusive Tortuosity

The diffusive tortuosity used for the SECOTP2D calculations is 0.11. This tortuosity value is the median tortuosity calculated from 36 core measurements at 13 locations as reported in Kelley and Saulnier (1990) together with additional measurements recently completed by Terra Tek (WP0#38234). (The measurements reported by Kelley and Saulnier (1990) were also made by Terra Tek.) Terra Tek first determined the formation factor based on electrical-resistivity measurements of core plugs. The formation factor results subsequently were used to calculate tortuosity. Tortuosity is a measurement of the tortuous nature of the pore structure within the rock. The smaller the value, the more tortuous the pathway and the slower the diffusion rate. The methodology used for the determination of formation factor and the calculation of tortuosities is described in Kelley and Saulnier (1990). A spreadsheet in the diffusive tortuosity parameter records package (WPO#37226) summarizes all the tortuosity data. Diffusive tortuosity is fixed parameter in PA calculations because there is a relatively small range to the data with few outliers.

Half Matrix Block Length

The matrix half-block length distribution used for the SECOTP2D calculation is a uniform distribution ranging from 0.05 to 0.5 m (i.e., full matrix block length values from 0.1 to 1.0 m), with a single value drawn from this distribution for each realization (implying that a single sampled value should represent an average of spatially variable block lengths along the expected "off-site pathway"). This distribution is derived from results of simulating the tracer tests conducted at the H-3, H-11, and H-19 hydropads. Numerical simulations were performed with double-porosity continuum models with both homogeneous and heterogeneous hydraulic conductivity fields. The homogeneous approach utilized the SWIFT-II transport code, and the heterogeneous approach used the THEMM code; both are being qualified per WIPP QAP 19-1. (See WPO#37450 for additional information on simulations.)

Both modeling approaches yielded consistent results for each well-to-well path with regard to matrix block length. It should be pointed out that for some paths the best fit block length is somewhat smaller than the minimum value of the range (e.g., H-11b2), and for some paths the best fit is larger than the recommended range (e.g., H-3b1) for the PA distribution. However, as mentioned above, the PA distribution is really a

Information Only

11

distribution of expected spatial averages, since each realization utilizes a single value for block length for the entire simulation domain. It is also important to remember that the tracer test results reflect transport behavior over paths of lengths represented by the well spacing, or lengths ranging from 10 to 30 meters. Considering these two facts, the entire range of matrix block length values inferred from the tracer tests has been truncated to yield the PA distribution which ranges uniformly from 0.1 to 1.0 m. Any single value drawn from the distribution should represent an aerial average for the exit pathway of 2.5 km length, roughly the distance from the center of the waste panels to the land withdrawal boundary. We strongly feel that the extreme value of matrix block greater than 1.0 m will not occur over regions as large as the exit pathway. It should be noted that simulations with a large matrix block length (small surface area for diffusion) will lead to more releases (compared to simulations with small matrix block lengths) because there will be less diffusion and in turn less accessible surface area for sorption.

In general, the matrix block length and advective porosity were the two primary fitting parameters inferred from comparing simulation results to field data. This is because essentially all of the other physical transport parameters could be measured independently with semi-quantifiable and rather small uncertainties; these other parameters were thus considered "fixed values" in the simulations (See WPO#37439). In an effort to obtain extreme values for matrix block length (as well as advective porosity), some of the interpretive simulations stressed the fixed parameters towards the endpoints of their uncertainty range. The "stressing" of fixed parameters was performed in a deliberate fashion such that all changes to the fixed values would "push" the fitted parameter value in the same direction. For instance, to obtain the minimum matrix block length one would decrease the well spacing, the free-water diffusion coefficient and the diffusive porosity, and increase the pumping rate. Simulations with stressed parameters were only conducted for those pathways that had either very large or very small block lengths for the best fit simulations with the fixed parameters at our best estimate. The best-fit matrix block lengths for the stressed simulations lie at or beyond the endpoints of the best-fit distribution (and well beyond the endpoints of the recommended PA distribution). Again, as alluded to in the preceding paragraph, while such extreme values of matrix block length may be valid for simulating transport in the Culebra at some locations within the WIPP simulation domain, it is considered highly unlikely that they occur over regions approaching the length scale of the entire exit pathway. Thus the recommended PA distribution for aerially-averaged matrix block length has endpoints less extreme than the hydropad-scale fitted values. A uniform distribution is recommended because it gives equal probability to all values within the distribution. Even though tracer test interpretations to date suggest that there may be a somewhat higher probability that the block length should be at the lower end of the distribution, given the facts that we have only a limited number of tests sites and that smaller block lengths will yield slower travel paths to the PA compliance boundary (e.g., more physical retardation), we have chosen to recommend a uniform distribution.

Information Only

One final note which must be addressed relates to the fact that the PA model (SECOTP2D) utilizes a parallel plate model for simulating double-porosity (fracture and matrix) transport, whereas our tracer test interpretive tools (SWIFT II and THEMM) utilize spherical models for simulating the matrix block geometry. (The matrix block length is conceptualized as the thickness of a matrix block between two fractures and represents the surface area to volume ratio for diffusion between the advective porosity and the diffusive porosity.) One important consideration results from this difference in conceptualization of physical retardation via matrix diffusion. This consideration is important with respect to matrix diffusion parameters, particularly when the time scale of a solute pulse duration is small with respect to the diffusion time scale for solute to move from the fracture-block interface to the center of the block. When the pulse duration time scale is small compared to the diffusion-to-block-centroid time scale (e.g., relatively large blocks), the diffusing solute never "feels" solute diffusing in from the other side of the block and it behaves as if it is diffusing into an infinite length block. In these cases, the surface area for diffusion determines the diffusion rate and one can directly convert from the spherical model to the parallel plate model by dividing the block length determined using the spherical blocks by three. On the other hand, when the diffusion-to-block-centroid time scale is equal to or less than the pulse duration time scale (e.g., for relatively small blocks, or long solute pulse durations), solutes invading matrix blocks from opposite sides "meet" at the centroid, resulting in decreased concentration gradients and concurrent decreases in physical retardation due to decreased matrix diffusion. When the blocks become saturated, the spherical and parallel plate block model block lengths can be considered equivalent. At this limit, the double-porosity transport model converges on a single porosity model with all of the pore space (advective + diffusive porosity) immediately accessible by solutes (thus no fast fracture flow paths with rapid transport to the compliance boundary). Between the extremes of large blocks with essentially infinite diffusion and small blocks which allow immediate complete solute saturation of all porosity (equivalent to single-porosity with high porosity), the block length obtained by a spherical model would be between 1-3 times larger than that that would be obtained with a parallel plate model. Given that the conversion between spherical and parallel plate models depends on the parameters of the simulation, that we expect the smaller block sizes in the distribution given to PA to have small diffusion time scales compared to expected pulse duration's time scales, and that the larger blocks will yield faster travel paths to the PA compliance boundary with less physical retardation, we have chosen not to divide our block lengths by three for the recommended PA distribution.

Advective Porosity

The advective porosity distribution used for the SECOTP2D calculation is log-uniform over a range from $1x10^{-4}$ to $1x10^{-2}$. This distribution was derived from numerical simulation of the tracer tests conducted at the H-3, H-11, and H-19 hydropads, and comparing simulated to observed tracer breakthrough data at the pumping well. As mentioned above for matrix block length, two different double-porosity conceptual

Information Only

models were applied, a homogeneous media approach and a heterogeneous media approach. The homogeneous approach utilized the SWIFT-II transport code, and the heterogeneous approach used the THEMM code. (See WPO#37450 for additional information on simulations.)

Both modeling approaches yielded consistent results for each well-to-well path with regard to advective porosity. As was the case for matrix block length, for some paths the best-fit advective porosity is somewhat smaller than the minimum value of the range (e.g., H-11b3) and for some paths the best fit is larger than the recommended range (e.g., H-19b2, b3, b4, b5, b6, b7). It is important to remember that the tracer test results reflect transport behavior over paths of lengths represented by the well spacing, or lengths ranging from 10 to 30 meter. The entire range of best fit values from the tracer tests has been truncated for the PA distribution based on the fact that the PA transport model utilizes a single value for advective porosity for the entire simulation domain. Recall that single value should represent an aerial average for the exit pathway. We strongly feel that the extreme values of advective porosity less than $1x10^{-4}$ will not occur over regions as large as the exit pathway, and thus aerial averages lie between these two endpoints. It should be noted that simulations with a small advective porosity will lead to more releases (compared to simulations with large advective porosity) because there will be faster transport resulting in less time for diffusion and in turn less accessible surface area for sorption.

As mentioned above, the advective porosity and matrix block length were the two primary fitting parameters inferred from comparing simulation results to field data. Again, in an effort to obtain extreme values for matrix block length and advective porosity, some of the interpretive simulations stressed the fixed parameters towards the endpoints of their uncertainty range. The "stressing" of fixed parameters was performed in a deliberate fashion such that all changes to the fixed values would "push" the fitted parameter value in the same direction. Simulations with stressed parameters were only conducted for those pathways that had either very large or very small block lengths for the best fit simulations with the fixed parameters at our best estimate. The best-fit advective porosity for the stressed simulations lie at or beyond the endpoints of the best-fit distribution (and well beyond the endpoints of the recommended PA distribution). Again, as alluded to previously, while such extreme values of advective porosity may be valid for simulating transport in the Culebra at some locations within the WIPP simulation domain, it is considered highly unlikely that they occur over regions approaching the length scale of the entire exit pathway. Thus the recommended PA distribution for aerially-averaged advective porosity has endpoints less extreme than the hydropad-scale fitted values. A log uniform distribution is recommended because it gives equal probability to all values in log space. There is not sufficient data from the three hydropad test sites to create a meaningful probability distribution other than log uniform. Two of the tracer test sites have a relatively low advective porosity and one site has a high advective porosity.

Information Only

Dispersivity

For the PA transport simulations using SECOTP2D, we recommend using a longitudinal and transverse dispersivity equal to zero. If, for numerical stability and/or convergence reasons, a non-zero value is desired, we recommend a constant value of 2 m or smaller. For simulations using a non-zero longitudinal dispersivity, we recommend a longitudinal to transverse dispersivity ratio of 10:1. The rationale for this recommendation lies in the fact that dispersive spreading due to permeability heterogeneity at the PA scale appears to overwhelm dispersive mixing observed at smaller (e.g., hydropad) scales (see detailed discussion below). Given that PA models for flow and transport in the Culebra explicitly account for heterogeneity in the permeability fields, there is no need to specify a discrete dispersivity value to account for mixing at the PA and smaller scales.

Research into solute dispersion in groundwater over the past couple of decades has identified a characteristic trend in dispersivities over a wide range of length scales of interest. The trend clearly shows that dispersivity tends to increase as one moves from a labortory column scale (cm) to the field scale (m), with larger field problems exhibiting generally higher dispersivity than smaller field problems. This trend perhaps is best summarized by the well-known Gelhar figure (e.g., Gelhar, 1986; Gelhar et al., 1992) in which lab and field data from a large number of experiments are presented on a single plot; this plot is reproduced here as Figure 2. This figure clearly shows the longitudinal dispersivity, α_l, increasing with the scale of the problem. Also shown in the plot are dashed curves which approximate the min-max envelope of the data and the straight line $\alpha_l=0.1L$ where L is the length scale of the experiment domain. The $\alpha_l=0.1L$ line represents the "rule of thumb" often employed when one simulates field-scale problems without the luxury of having site-specific field-scale dispersivities. Notable for the purpose of the WIPP PA simulations is the fact that at scales greater than 1 km, all data values fall below the *0.1L* line (most of them substantially below the line with values ranging from *0.01L* to *0.001L).*

For the WIPP PA, we are interested in transport from the waste panel area to the land withdrawal boundary (LWB). For the most likely curvilinear exit trajectories, this distance is on the order of 2.5 to 3 km. Unfortunately, our largest scale site-specific data for the dispersivity of the Culebra is from the hydropad tracer tests, with well spacings ranging between 10 and 43 m. When intepreting the results of hydropad tracer tests conducted in the Culebra, best fits with homogeneous media models generally used dispersivities less than or equal to *0.1L*. Furthermore, hydraulic testing at the hydropad sites yielded estimates of the lnK variance (σ_{lnK}^2) and lnK correlation scale (λ) product of less than 1.5 m. Stochastic analyses of flow and transport in heterogeneous aquifers (e.g., Gelhar, 1986) derive this product as an estimator of asymptotic macrodispersivity, $\sigma_{lnK}^2 \cdot \lambda = \alpha_l$. In summary, hydraulic and tracer testing of the Culebra dolomite at the WIPP site indicate that at the hydropad scale the dispersivity is generally less than 2 m. Based on Figure 2, at a length scale of an exit trajectory from the waste panels to the LWB (~3

Information Only

Figure 2. Laboratory and field measured values of longitudinal dispersivity as a function of scale of measurement. The largest circles represent the most reliable data (Adapted by Fetter, 1993, from Gelhar, 1986).

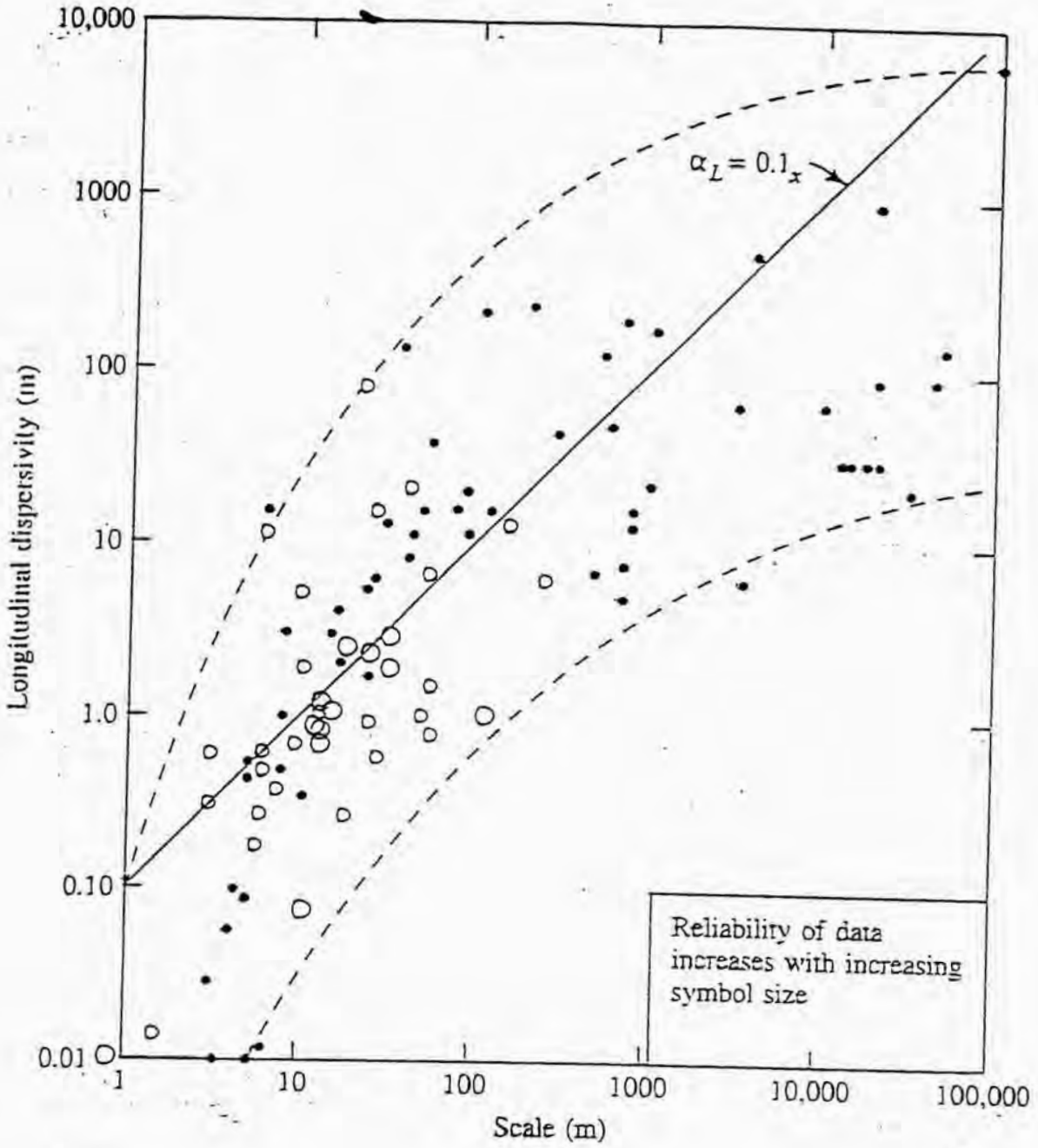

Information Only

km) we would expect dispersivities to range somewhere between 10 and 1000 m (or a normalized dispersivity $A=\alpha/L$ to vary between .0033 and 0.33).

This gross estimate of large scale dispersivity derived from Figure 2 can be compared to site-specific spreading estimates using the PA flow model. The PA groundwater flow and transport simulations explicitly acknowledge heterogeneity in the Culebra permeability fields by providing a gridblock by gridblock variation in permeability , with that variation conditioned on permeability measurements/observations from hydropad scale hydraulic testing (i.e., T-fields generated by GRASP-INV, see Appendix TFIELD). One can estimate the effective dispersivity associated with the heterogeneous permeability fields by tracking particles from the source (waste panel) area to the exit (LWB) location, and computing the temporal statistics of the particle travel time from source to exit. Equation 10.7 in Domenico and Schwartz (1990) show that one can use the temporal statistics to compute the dispersivity from such a particle tracking exercise:

$$\alpha_l = \frac{v\sigma_t^2}{2t} \qquad (1)$$

where v is the average pore water velocity (computed as the distance divided by the mean travel time), σ_t^2 is the variance of particle travel time, and t is the mean travel time. We implemented this approach by tracking particles released along a line in the middle of the waste panel area (with the line parallel to the LWB) to the Land Withdrawal Boundary, and the particle tracking results yielded the input parameters required for equation 1 (σ_t^2 and t). This particle tracking was performed on all 100 heterogeneous permeability field realizations generated by GRASP-INV for the 1996 PA (undisturbed by mining). Results of this particle tracking approach show heterogeneity-induced spreading to yield PA-scale dispersivities ranging from approximately 10 m to approximately 1000 m (normalized values between .003 and 0.3). This result is entirely consistent with published results from other experiments conducted around the world published before 1992 (e.g., Figure 2), and these dispersivities are significantly larger than those inferred from the hydropad tracer test results. We therefore feel that, given no site-specific large-scale data on dispersivities, we can trust that the transmissivity heterogeneity explicitly accounted for in the Culebra flow (SECOFL2D) simulations will impart a reasonable amount of dispersive solute spreading on simulated actinide releases with no need to specify additional spreading through the dispersivity parameter in SECOTP2D.

Gelhar et al. (1992) also summarize experimental results related to transverse dispersivity, and they show that the ratio of longitudinal to (horizontal) transverse dispersivity generally ranges between 2:1 and 50:1 and exhibits no clear trend with problem scale. For the WIPP site, no definitive / highly reliable data set exists to provide an estimate of transverse dispersivity. Again, we feel that the heterogeneity in the flow simulations will cause a reasonable amount of spreading, and we should not take credit

Information Only

17

for additional spreading by specifying a dispersivity for SECOTP2D which exceeds that caused by the transmissivity heterogeneity.

Based on the above data, analysis, and discussion, any specified value of longitudinal dispersivity less than roughly 2 m will yield similar results for solute transport in the Culebra dolomite from the WIPP waste panel area to the LWB. Assuming that the numerical codes used correctly solve the governing partial differential equations, simulations using local dispersivities less than or equal to 2 m will yield results consistent with field-scale dispersive spreading observations as reported by Gelhar et al. (1992). Given the lack of WIPP site-specific information related to transverse dispersivity, we rely entirely on previous studies (e.g., see Gelhar et al., 1992) to recommend a ratio of longitudinal to transverse dispersivity equal to 10:1.

Parameter Cross Correlations

One might suspect the possibility of some cross correlation between sampled parameters. To test this suspicion, we have prepared scatter plots of interpreted results from the hydropad test sites which yielded the physical transport parameters used to develop the PA parameter distributions (H-3, H-11, and H-19). Scatter plots of well-to-well transmissivity versus well-to-well advective porosity and matrix block length showed no observable trends, nor did a scatter plot of advective porosity versus matrix block length. These results strongly suggest a lack of correlation between these parameters, and therefore the recommended PA distributions include no cross correlations.

References

Beauheim, R. L. 1987. *Interpretations of Single-Well Hydraulic Tests Conducted at and Near the Waste Isolation Pilot Plant (WIPP) Site, 1983-1987.* SAND87-0039.

Beauheim, R. L., L.C. Meigs, G.J.Saulnier, and W.A. Stensrud, 1995. Culebra Transport Program Test Plan: Tracer Testing of the Culebra Dolomite Member of the Rustler Formation at the H-19 and H-11 Hydropads on the WIPP Site.(Tracer test data will be in WPO#s 37452, 37467, and 37468.)

Cauffman, T.L., A.M. and J.P. McCord. 1990, *Ground-Water Flow Modeling of the Culebra Dolomite*, Volume II: Data Base. SAND89-7068/2

Domenico, P., and F.W. Schwartz, 1990. *Physical and Chemical Hydrogeology*, John Wiley Publishing.

Fetter, C.W., 1993. *Contaminant Hydrogeology*, Macmillan Publishing Co., 458 pp.

Gelhar, L.W., 1986. Stochastic subsurface hydrology from theory to applications, *Water Resources Research* , v.22(9): 135s-145s.

Gelhar, L.W., C. Welty, and K. Rehfeldt, 1992. A critical review of data on field-scale dispersion in aquifers, *Water Resources Research*, v.28(7): 1955-1974.

Hydro Geo Chem, 1985. *WIPP Hydrology Program, Waste Isolation Pilot Plant, SENM, Hydrologic Data Report #1*, SAND85-7206, 710pp.

Information Only

Holt, R.M. 1996. unpublished letter report entitled *Hydrostratigraphy of the Culebra Dolomite Member of the Rustler Formation in the WIPP Region* (WPO#38225).

Holt, R. M. and D.W. Powers, 1984, *Geotechnical Activities in the Waste Handling Shaft.* WTSD-TME-038, U.S. Department of Energy by TSC and International Technology Corporation

Holt, R. M. and D.W. Powers, 1986, *Geotechnical activities in the Exhaust Shaft,* DOE-WIPP 86-008, U.S. Department of Energy, WIPP Project Office, Carlsbad, NM

Holt, R. M. and D.W. Powers. 1988. *Facies Variability and Post-Depositionsl Alteration Within the Rustler Formation in the Vicinity of the Waste Isolation Pilot Plant, Southeastern, New Mexico.* DOE-WIPP 88-004, U.S. DOE, WIPP Project Office, Carlsbad, NM.

Holt, R. M. and D.W. Powers. 1990. *Geologic mapping of the Air Intake Shaft at the Waste Isolation Pilot Plant, Southeastern New Mexico.* DOE-WIPP 90-051, US.S. Department of Energy, WIPP Project Office, Carlsbad, NM

Jones, T.L., V.A. Kelley, J.F. Pickens, D.T. Upton, R.L. Beauheim, and P.B. Davies. 1992. Integration of Interpretation Results of Tracer Tests Performed in the Culebra Dolomite at the Waste Isolation Pilot Plant Site, SAND92-1579.

Kelley, V.A. and G.J. Saulnier. 1990. *Core Analyses for Selected Samples from the Culebra Dolomite at the Waste Isolation Pilot Plant Site.* SAND90-7011.

Kloska, M.B., G.J. Saulnier, Jr., and R.L. Beauheim. 1995. *Culebra Transport Program Test Plan: Hydraulic Characterization of the Culebra Dolomite Member of the Rustler Formation at the H-19 Hydropad on the WIPP site.* (Results to be contained in WPO#s 38400 and 38401.)

Mercer, J.W. and B.R. Orr. 1979. *Interim data report on the geohydrology of the proposed Waste Isolation Pilot Plant Site in southeastern New Mexico,* U.S. Geological Survey Water Resources Investigations Report 79-89.

Stensrud, W.A., M.A. Bame, K.D. Lantz, J.B. Palmer, and G.J. Saulnier, 1990. *WIPP Hydrology Program, Waste Isolation Pilot Plant, Southeastern New Mexico, Hydrologic Data Report #8,* SAND89-7056.

Information Only